Faculty of Physics and Astronomy

University of Heidelberg

Diploma thesis

in Physics

submitted by

Simon Altevogt

born in Göttingen

2003

Production of rotationally cold H_3^+ ions with a hollow cathode ion source

This diploma thesis has been carried out by *Simon Altevogt* **at the**
Max-Planck-Institut für Kernphysik
under the supervision of
Prof. Dr. Andreas Wolf

Kurzfassung

Produktion von rotationskalten H_3^+ Ionen in einer Hohlkathodenquelle

Eine Hohlkathodenquelle wurde nach Vorlage einer Quelle konstruiert, die in der Gruppe von Prof. H. Helm an der Universität Freiburg in Gebrauch ist. Die Quelle wurde gebaut und getestet am Max-Planck-Institut für Kernphysik in Heidelberg. Die Quelle ist einfach aufgebaut und enthält drei Elektroden: eine Anode, eine Kathode und eine Bias-Elektrode, die direkt hinter der Kathode angebracht ist. Anode und Kathode werden mit flüssigem Stickstoff gekühlt. Zwei unterschiedliche elektrische Schaltungen wurden untersucht. Die erste Schaltung sieht ein Anodennetzteil und ein Biasnetzteil vor, während die zweite eine zusätzliche Hochspannungsplatform aufweist, auf der das Anodennetzteil untergebracht ist. Die Ionenausbeute zeigt eine starke Abhängigkeit vom Quelleninnendruck und der Entladungsintensität. Ein maximaler, stabiler H_3^+ Strom von bis zu einigen μA konnte erzielt werden. Die dissoziative Rekombinationsreaktion von H_3^+ mit Elektronen bei null Relativenergie, wurde benutzt, um die Rotationsanregung der Ionen zu bestimmen. Die Experimente wurde in einem 'merged-beam' Aufbau am Schwerionenspeicherring TSR ausgeführt. Durch den Vergleich mit Monte-Carlo-Simulationen konnte eine minimale Rotationsenergie der Ionen von $k\mathrm{T}_{rot} \ll 100\mathrm{meV}$ für die zweite Beschaltungsart abgeleitet werden.

Abstract

Production of rotationally cold H_3^+ ions with a hollow cathode ion source

A hollow cathode ion source has been build following a design in use in the group of Prof. H. Helm at the Universität Freiburg. The source was manufactured and its properties have been studied in detail at the Max-Planck-Institut für Kernphysik in Heidelberg. The source features a simple layout consisting of three electrodes: an anode, a cathode and a bias electrode situated directly after the cathode. Both anode and cathode are cooled by liquid nitrogen. Two different types of electrical wiring have been tested. The first type featured a straightforward wiring, while in the second type anode and cathode were mounted on a separate platform. The ion yields were found to be strongly dependent on the inside H_2-gas pressure and discharge intensity. A stable maximum current of up to several μA of H_3^+ could be produced. To determine the rotational temperature of the ions, the dissociative recombination of the H_3^+ ions from the source with electrons at zero relative energy was studied in a merged beam setup at the heavy ion storage ring TSR. By comparing the results to Monte-Carlo simulations, the minimum rotational temperature of the ions was found to be $k\mathrm{T}_{rot} \ll 100\mathrm{meV}$ for the second wiring type.

Meinen Eltern

Contents

1. Motivation and goals

The molecular ion H_3^+ is the simplest stable polyatomic molecular system. It consists of two electrons and three protons. In the ground state, the protons occupy the vertices of an equilateral triangle. Since its discovery by J. J. Thomson in 1912, it has been a testing ground for theoretical methods of calculating, for example calculations of rovibrational energy levels of polyatomic systems done by Carney in 1976 [1]. H_3^+ is formed through the reaction $H_2 + H_2^+ \longrightarrow H_3^+ + H$ [2]. This ion-neutral reaction is highly efficient owing to its high exothermicity of 1.7eV and it has a large cross section $\approx 100\text{Å}^2$ and no activation barrier [3]. Hence, H_3^+ is found wherever molecular hydrogen is present and partly ionized. As hydrogen is by far the most abundant element in the universe, H_3^+ was long expected to be an astrophysical important species [4]. But it wasn't until the late 1990s that the presence of H_3^+ could be proven in interstellar clouds [5, 6], which contain about 100 particles per cm^3 at a temperature of 100K compared to a total density of 10^3 particles per cm^3. Furthermore, H_3^+ is an efficient proton donor to neutral molecules via the so called proton hop reactions $H_3^+ + X \longrightarrow XH^+ + H_2$ [7]. In interstellar space this reaction is believed to initiate chains of ion-molecule reactions, leading for instance to the formation of large organic molecules. Indeed, H_3^+ is a key component of models describing interstellar chemistry and its abundance in the interstellar medium is a benchmark for such models. The main process leading to the destruction of H_3^+ , beside the above mentioned proton hop reactions, is the dissociative recombination (DR) with low energy electrons: $H_3^+ + e^- \longrightarrow H_2 + H$ or $H + H + H$. Thus, the rate of destruction of H_3^+ via DR is a crucial aspect for the understanding of the chemistry in the interstellar medium.
Experimental studies of H_3^+ have given values for the rate of dissociative recombination with low energy electrons ranging over several orders of magnitude, varying according to the experimental methods applied for the measurement (see for example [8, 9]). More recent measurements are seen to converge towards one another. But still the value obtained from ion-storage ring measurements of about $1.15 \cdot 10^{-7}\ \frac{\text{cm}^3}{\text{s}}$ [10] differs by one order of magnitude from the result acquired in flowing-afterglow Langmuir probe (FALP) measurements of $< 1.3 \cdot 10^{-8}\ \frac{\text{cm}^3}{\text{s}}$ published by Glosík in 2000 [11]. Furthermore, with

the higher DR rate as measured with the storage ring technique, the astrophysical models cannot explain the large quantities of H_3^+ found in interstellar clouds.

Theoretically the DR reaction with cold electrons was considered impossible for a long time [12]. But the gap between theory and experiment began to narrow when a two-dimensional calculation was published by Schneider in 2000 [13], which, including the DR reaction at zero electron energy, led to an H_3^+ destruction rate close to $10^{-9}\ \frac{\mathrm{cm}^3}{\mathrm{s}}$. However, this value is still far below the rates observed experimentally. An attempt to resolve this puzzle was made by Kokoouline and coworkers in 2001 [14]. The autors were able to show that the Jahn-Teller symmetry-distortion effect [15] generates recombination at a much faster rate than any other mechanism, raising the value of the theoretically predicted rate to $10^{-8}\ \frac{\mathrm{cm}^3}{\mathrm{s}}$.

In addition, the novel calculations suggested that the rotational excitation of H_3^+ can have a significant influence on the rate of the dissociative recombination of H_3^+ with low energy electrons. This could very well explain the difference between rates measured in storage ring experiments, FALP measurements and theoretical calculations. However, detailed measurements with molecular ions of controlled rotational excitation are necessary to test these ideas.

The storage ring technique offers the advantage of very long storage times of the observed molecular species. This allows rovibrational excitations of the molecules to be removed by emission of radiation. However, this can not be applied in the case of H_3^+, since the rotational relaxation of the H_3^+ ion can be said to be very slow due to its vanishing dipole moment in the vibrational ground state. Indeed, while the vibrational excitation was found to relax to the ground state after $\approx$ 2s of storage [16], a sizable amount of rotational molecular excitation was still found to be present even after 40s of storage time [17]. Hence, to be able to perform measurements on rotationally cold H_3^+ ions in a storage ring, one needs to reduce the initial rotational excitation that the ions posess when leaving the ion source.

In order to control the initial excitation of the H_3^+ ions, we sought a way of production in a cold environment. Therefore a simple ion source design with the possibility of liquid nitrogen cooling was aspired. The source layout was adapted from a present design of an ion source in use by the group of Prof. H. Helm at the Unversität Freiburg. The ion source was built and assembled at the Max-Planck-Institut für Kernphysik in Heidelberg prior to this work.

The aim of this diploma thesis was to examine the properties of the constructed ion source and therefore will focus on the following aspects:

- Characterization of the ion source. That includes:
  - a simulation of the field distribution inside the ion source,
  - a determination of the discharge characteristics,
  - an examination of the different ion species produced in the source, with special attention paid to the production of H_3^+ .
- Measurement of the rotational excitation of the H_3^+ ions produced in the ion source.

2. Hollow cathode discharges

2.1 Gas discharge physics

2.1.1 Gas breakdown and the self sustained discharge

The breakdown can be defined as the transformation of a non-conductive medium into a conductive one when a sufficiently strong electric field is applied.
According to the Townsend theory of breakdown charge carriers are produced by volume processes and by surface processes. The volume processes are described by the *ionization coefficient* α (first Townsend coefficient). The α coefficient gives the electron multiplication in the gas, i.e. the average number of ionization induced by an electron per unit length of the electron travel path in the direction of the electric field E. It is a function of the reduced electric field $\frac{E}{p}$, where p is the gas pressure, and is dependent on the type of gas.
The *secondary emission coefficient* γ (second Townsend coefficient) describes the processes that take place at the interface gas-cathode and represents the ratio of number of electrons emitted from the cathode per incident particle on the cathode surface. The secondary emission coefficient depends on the cathode material, the type of gas and the reduced electric field $\frac{E}{p}$. The γ coefficient includes the effect of several different particles impinging the cathode surface, namely: ions (γ_i), excited atoms (γ_m), electrons (γ_e) and photons (γ_p). A detailed description of the processes involved in the formation of secondary and primary electrons can be found in [18, 19, 20].
For initiating a self sustained discharge, one primary electron lost at the anode has to be replaced by at least one secondary electron created in the gas or at the cathode. For a homogeneous electric field the condition for self-sustenance can be given by

$$\gamma(e^{\alpha d} - 1) = 1 \quad \text{or} \quad \alpha d = ln(\frac{1}{\gamma} + 1) \ , \tag{2.1}$$

where d is the distance between the electrodes. This condition defines the *breakdown* of

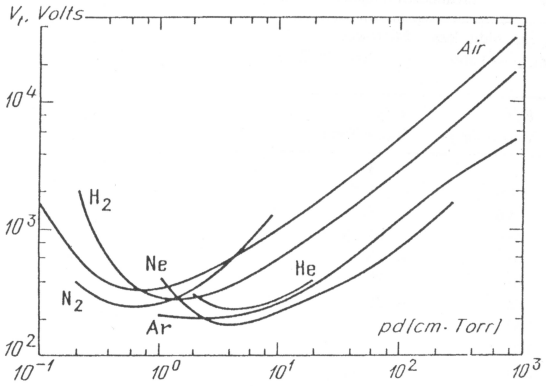

Figure 2.1: *Breakdown potentials over a wide range of pd values for different gases [19].*

the gas into a conductor. Taking into account that α and γ depend on the reduced electric field, the *breakdown voltage* V_t can be analytically derived [19]

$$\mathrm{V}_t = \frac{\mathrm{B}pd}{\ln(pd) + \ln(\frac{\mathrm{A}}{\ln(1+\gamma^{-1})})} \ , \tag{2.2}$$

where A and B are experimentally determined constants for a given gas. The dependence of the breakdown voltage on the product of electrode distance and gas pressure (pd) and the gas type is depicted by the so called *Paschen curves* shown in Fig. 2.1. A numerical approach to the Townsend theory of breakdown can be found in [21].

2.1.2 The glow discharge

In a discharge a large number of phenomena may occur. One way to classify these phenomena is by observing the changes in the current-voltage characteristic of the discharge. A characteristical current-voltage dependence is displayed in Fig. 2.2.
At low voltages (**A**–**B**) one observes the flow of a small discharge current caused by the charge carriers present in the gas due to background radiation. It saturates when all charge carriers are swept away (**B**–**C**). Once the voltage passes a value where the initially present electrons can acquire enough kinetic energy to ionize neutral gas particle, the current will rise exponentially (**C**–**D**). This region is called the *Townsend regime* or *Townsend discharge*. In the region of high electric field prior to electrical breakdown (**D**–**E**), one can observe corona discharges, especially on sharp points and edges of the electrodes. Electrical breakdown occurs when the necessary amplification due to secondary processes is reached (**E**); the discharge is now self-sustained.
In the *glow discharge regime* the discharge emits light because the electron energy and

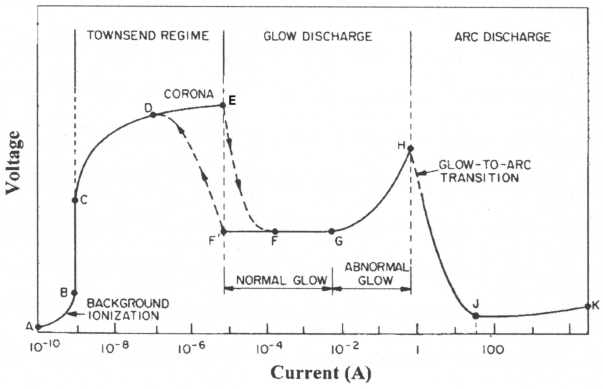

Figure 2.2: *Typical current-voltage characteristic of a low pressure discharge [22].*

number density are high enough to generate visible light by excitation collisions. After breakdown **E**–**F**, the gas enters the *normal glow region* in which the voltage is almost independent of the current over several orders of magnitude. As current increases, the discharge expands until it covers the complete cathode surface and then enters the *abnormal glow regime* (**G**–**H**) in which the voltage is no longer constant.
At point **H** the electrodes become sufficiently heated by the presence of the discharge. The cathode now emits electrons thermionically and the discharges undergoes the *glow-to-arc transition* (**H**–**I**). The following region of high current operation is called the *arc regime* (**I**–**K**).

2.1.3 Structure of the glow discharge

The structures of a glow discharge were first observed and described by Michael Faraday in 1830. They appear over a wide range of operating conditions. At low pressures, the glow discharge normally manifests a stratification into dark and bright luminous layers as illustrated in Fig. 2.3 b for a discharge in H_2 .
The main distinction of the glow discharge from the Townsend discharge lies in a sharply non-uniform distribution of the potential difference applied across the electrode gap as can be seen in Fig. 2.3 a. This results from the accumulation of space charge in front of the electrodes [19, 22, 20]. The ion mobility is much lower than that of the electrons. This leads to the accumulation of ions close to the cathode. Therefore most of the applied potential drops over a small distance ($d_{Cath.\ fall}$) close to the cathode, called the *cathode fall* $U_{Cath.\ fall}$.
Close to the cathode a thin dark space (*Aston dark space*) is situated followed by the *cathode glow*. The cathode glow is followed by the *cathode dark space*, the *negative glow*

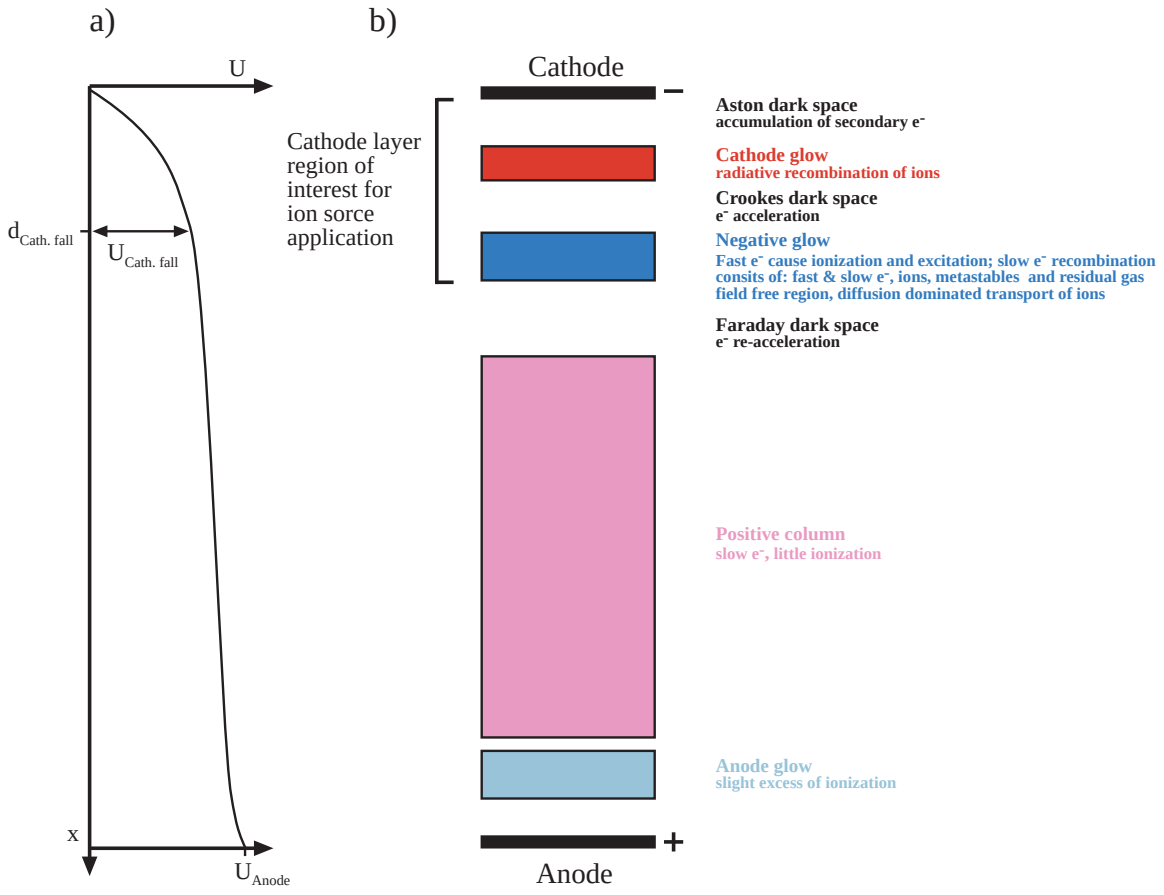

Figure 2.3: *Typical example of a plate-to-plate glow discharge and the distribution of (***a***) potential and(***b***) different structures. The colors correspond to the appearance of a discharge in* H_2 *taken from [18].*

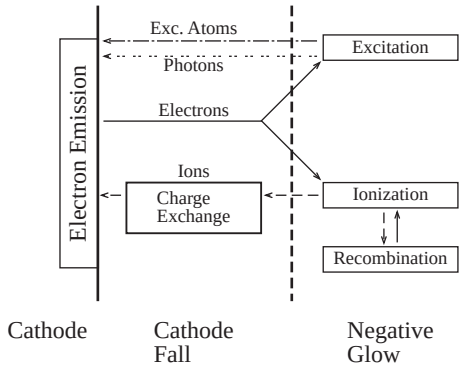

Figure 2.4: *Simplified carrier balance at the cathode after [23].*

and the *Faraday dark space*. This concludes the *cathode layer* region of the discharge. If the electrode separation gap is high enough, the positive column is present, followed by the *anode glow*. A description of the different processes connected to the various zones present in the glow discharge can be found in Fig. 2.3 b and in more detail in [19, 20, 18]. The cathode layer is determinant for sustaining the discharge. Electrons that have been accelerated in the cathode fall region result in a powerful ionization source creating ions in the negative glow. This is the reason why the negative glow is the brightest structure of the discharge. The negative glow can be considered to be almost field free because the high space charge potential of the ions shields of any external field. This means that the transport of ions in the negative glow is dominated by diffusion [23, 24, 19, 25].
A schematic drawing that summarizes the basic processes involved in the formation of a glow discharge can be found in Fig. 2.4.

2.1.4 The hollow cathode effect

The hollow cathode discharge is a special form of glow discharge operated in a cylindrical hollow cathode. In a specific range of operation the cathode layer is found to be inside the hollow structure of the cathode as illustrated in Fig. 2.5. Under such conditions the discharge current is found to be orders of magnitude higher for the same sustaining voltage than for a plane cathode. The effect was first observed by Paschen in 1916 and by Güntherschulze [26] in 1924 (see also [27]).
A brief overview of these different processes involved in the hollow cathode effect shall be given in this section. A more detailed description of the hollow cathode effect and its applications can be found in [23, 25, 28].
There are several mechanisms contributing to the hollow cathode effect:

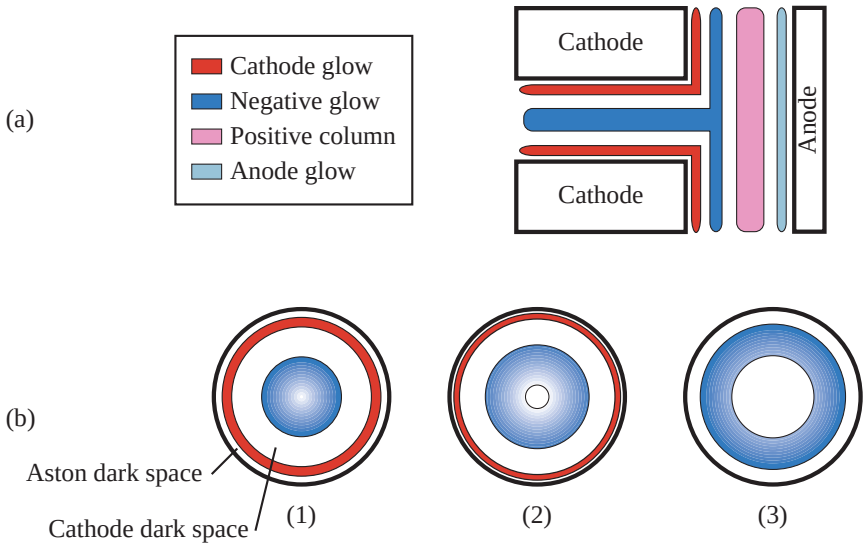

Figure 2.5: (**a**) *Schematic view of the arrangement of the structures in a hollow cathode discharge, compare to Fig. 2.3.* (**b**) *Evolution of the cathode layer for a cylindrical hollow cathode when the pressure increases, for* $p_1 < p_2 < p_3$.

- the *pendel effect*; electrons emitted from the cathode will be accelerated in the cathode fall and produce ionization in the negative glow. They will pass the negative glow and are repelled at the opposite cathode surface (pendular electrons). Due to their pendulum motions, the electrons are kept inside the cathode for a longer time and therefore contribute to a further enhanced ionization rate [29, 30].

- the production of secondary electrons is enhanced. Due to the hollow geometry particles (metastables, photons, ions) have a higher chance of hitting the cathode effectively increasing the electron emission rate of the cathode.

- the confined structure leads to a higher density of sputtered atoms of the cathode material. This causes an increase in secondary emission since these metal atoms have a much lower ionization potential [31].

- the higher plasma densities inside the hollow cathode makes multistep processes more likely [32].

- the cathode fall in a hollow cathode can be significantly thinner, reducing the probability of charge transfer collisions. Therefore the average ion velocity at the cathode is increased, causing an increased secondary electron emission rate [33].

All these mechanisms strongly depend on the operation conditions, such as the hollow cathode geometry, the inside pressure p, the fill gas, and the cathode material. The most

important process is the pendel effect. It is only present if the electron mean free path is of the same order as the cathode inner diameter D. Therefore the optimal pD value should be in the range of 0.1–10 $\frac{\text{torr}}{\text{cm}}$ [23, 34].

2.2 Discharges in H_2

When comparing hollow cathode discharges driven in rare gases, such as helium or neon, to discharges in molecular ions, such as H_2 , one should expect to see a change in discharge behavior because of the absence of metastable energy levels in molecular gases. However, research has been done on low pressure hollow cathode discharges (here 2 torr) by Sturges and Oskam in 1966 [35], showing no fundamental difference in the discharge characteristic. Indeed, it was found that the behavior of H_2 discharges and the enhancement of the discharge efficiency, due to the hollow cathode effect, was very similar to that experienced in helium discharges under same the conditions. This indicates that under low pressure conditions the influence of metastables on the hollow cathode effect can be neglected.
In the case of ion production in the plasma one has to distinguish between primary ions formed by collisions with energetic electrons (*electron impact ionization*) and ions formed due to secondary processes. In a H_2 discharge primary ions are merely H_2^+ . This could be illustrated by Smyth in 1925 [36] by looking at the pressure dependence of ion production. It was shown that at low pressures H_2^+ dominated, while at higher pressures it almost vanished because of the production of secondary ions, namely H^+ and H_3^+ . For the production of H_3^+ , Hogness and Lunn [2] suggested the reaction

$$H_2^+ + H_2 \longrightarrow H_3^+ + H \ , \tag{2.3}$$

having a very high cross section, which was later confirmed to be of the order of $\approx 100\text{Å}^2$ [37] at 300K. The production of H^+ , then resulting from breakup reactions of the primary ion, is much less likely than the H_3^+ formation [2]. Later, the formation of heavier particles in hydrogen plasmas were reported, which could be identified as H_5^+ [38, 39] being formed in 3-body collisions $H_3^+ + 2H_2 \longrightarrow H_5^+ + H_2$. Also the production of even higher H_2 cluster ions is possible. Reported up to the current date are H_{23}^+ ion clusters [40] that only form at low temperatures, making them very unlikely candidates for formation in discharges.
Furthermore, there are also reactions leading to the destruction of H_3^+ in the discharge, i.e. collision induced dissociation (CID), dissociative recombination (DR) and the asymmetric charge transfer (ACT). These reactions will become important at a later stage (see

Sec. 3.2) and should thus be mentioned here.

$$CID: \quad H_2 + H_3^+ \longrightarrow \begin{cases} H_2^+ + H + H \\ H^+ + H_2 + H_2 \end{cases} \tag{2.4}$$

$$DR: \quad H_3^+ + e^- \longrightarrow \begin{cases} H + H + H \\ H + H_2 \end{cases} \tag{2.5}$$

$$ACT: \quad H_2 + H_3^+ \longrightarrow (H_2^+)^{**} + (H_3^0)^{**} \tag{2.6}$$

Studies on the ion energy distribution in a glow discharge conducted by Davis and Vanderslice in 1963 [41] could give answers to the regions of production in the discharge. Looking at the ion energies of particles extracted directly at the cathode, it could be shown that the H_3^+ ions have a quite sharp energy distribution, with a large number of them having an energy corresponding to the cathode fall potential. This suggests that most of the H_3^+ ions are formed by collisions in the negative glow and not in the cathode fall region. A similar energy distribution was found for H_2^+ and only the distribution of H^+ is significantly broader, giving rise to the assumption that H^+ is also produced in other regions of the plasma.

3. Construction and characterization of the ion source

The ion source used in this case is a hollow-cathode and hollow-anode type ion source. The main body of the ion source is an exact copy of a source in use at the Universität Freiburg in the group of Prof. H. Helm. There it has been used to produce H_3^+ ions and their isotopomers required to be rotationally and vibrationally as cold as possible [42, 43]. No thorough examination of the rovibrational distribution of the ions from the source has been done although influences of the ion source conditions on the rotational distribution were found in measurements on dissociative charge transfer [44].
This chapter will cover the construction and characterization of the ion source, starting with the description of the design in Sec. 3.1. Then two different electrical wirings with field simulations will be presented (see Sec. 3.2). The plasma characteristic as measured for a H_2 discharge is described in Sec. 3.3 and in Sec. 3.4 the ion production capabilities of the source will discussed.

3.1 Design

A technical drawing of the various source parts is shown in Fig. 3.1 and Fig. 3.2 displays a picture of the assembled source.
The complete ion source is mounted on a DN160CF flange. The flange includes six SHV feedthroughs, for electrical connections, and three DN16CF feedthroughs, as illustrated in Fig. 3.1 and 3.2. The DN16CF feedthroughs are equipped with $^1/_4''$ VCR couplings. Two of them are used as liquid nitrogen inlet and outlet, while the remaining one is used for H_2 gas inlet to the source. A DN40CF hole has been introduced into the flange that is sealed with an appropriate viewport, which allows monitoring of the burning discharge through another viewport in the rear end of the source volume. The source body is hold in place by three M4 steel rods protruding from the flange through the viewport, anode

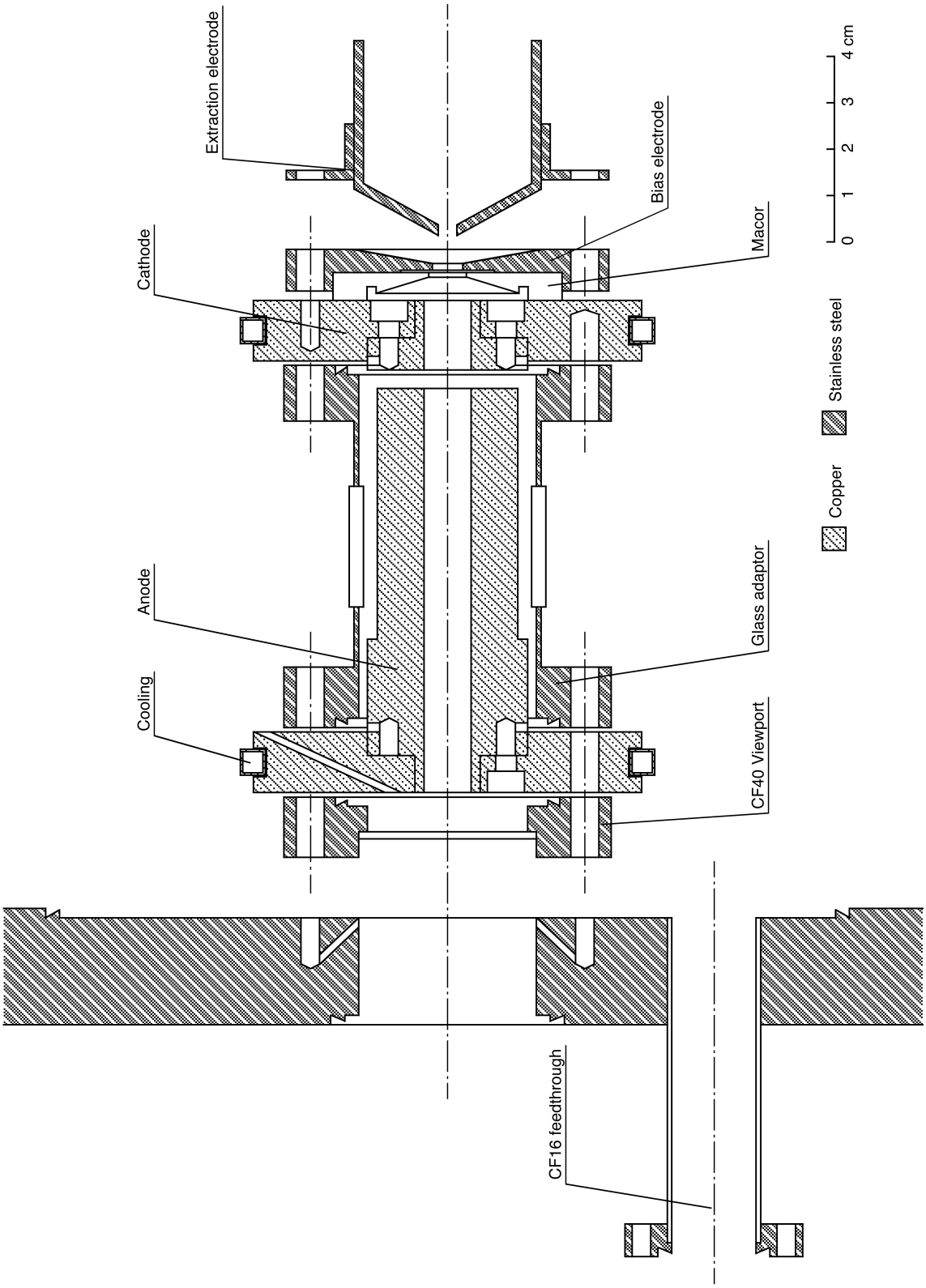

Figure 3.1: *The layout of the hollow cathode ion source.*

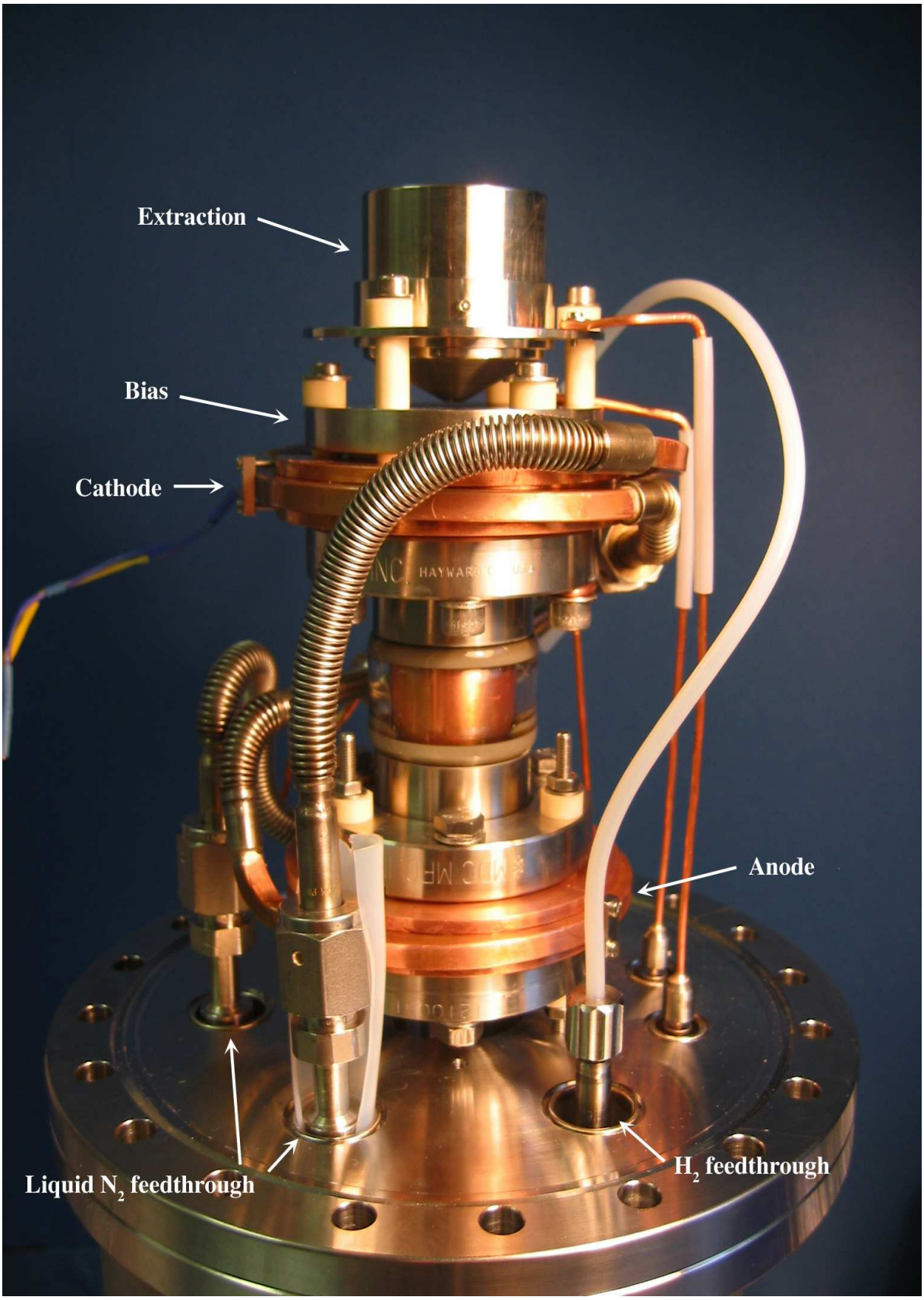

Figure 3.2: *The hollow cathode ion source assembled.*

and the lower part of a glass adaptor. The source body is electrically insulated from the flange by Degussit tubes (outer diameter 7mm), which enclose the rods, and by Degussit endcaps.

To allow the operation of high pressure discharges while keeping the source in a high vacuum environment, the discharge is maintained in a separate volume with only a small opening ($\approx$ 0.4mm) to the high vacuum. All connections are sealed with Teflon DN40CF gaskets which are softer than copper caskets. Therefore, copper can be used as electrode material for the anode and the cathode, which features a superior heat conductance of $\approx 700\frac{\mathrm{W}}{\mathrm{mK}}$ at 100K [45]. The source volume is closed in the back by another DN40CF viewport which is screwed directly onto the anode electrode. The discharge is maintained between an anode and a cathode structure. These two structures are separated by a glass adaptor (standard piece from MDC Caburn part no. 462002) with a length of about 80mm. The anode structure consists of two parts. A copper disc of 13mm thickness and 83mm in diameter, with a small dent on the outer rim where the cooling tubes are attached and a hollow copper cylinder, with an overall length of 8.8cm and an inner diameter of 1cm. The copper cylinder is inserted into the anode and hold in place by four M4 screws. The dimensions and design of the cathode structure are similar to the anode. It is made up of two parts, namely a copper disc (13mm thickness and 83mm diameter) and a small copper inlay (length 1.5cm and an inner diameter of 1cm). In view of the rough treatment imposed by the burning discharge on the cathode surface, this construction makes maintenance of the cathode much easier, since the inlay is replaceable. To prevent the discharge from burning to the inside of the glass adaptor, its upper part is insulated from the anode by a layer of Teflon foil. Following the cathode structure is a ring made of Macor material. It is pressed onto the cathode by the bias electrode. A small Molybdenum disc is situated between the macor and the bias electrode. It is kept in position by a dent on the bottom side of the bias electrode. The disc has a diameter of 2cm and includes a hole in the center. This hole defines the opening to the high vacuum environment. The disc can be exchanged by removing the bias electrode, making replacement for maintenance purposes easy, but also offers the possibility to introduce other exit hole diameters, ranging from 0.2–1mm. The design of the extraction electrode was modeled with SIMION 3D [46] to ensure best ion extraction at low voltages and a focusing effect on the ion beam. Again degussit tubes and endcaps are used to insulate the mounting screws from the electrodes and positioning, for both the bias and extraction electrode.

As can be seen in the picture (Fig. 3.2), the implementation of the cooling is done with copper tubings and stainless steel bellows for the flexible parts. The cooling circuit con-

nects cathode and anode in series. Insulating ceramic parts were introduced on both feedthroughs and in the segment bridging the two electrodes.
For monitoring of the cathode temperature we use a platinum electrode with known temperature resistance dependency (PT100). The PT100 is glued onto the cathode from the outside. The resistance of the PT100 is determined by measuring the voltage drop over the PT100. Therefore, the PT100 signal is fed via Kapton insulated cables to a RS232 connector feedthrough in a DN40CF flange introduced in the enclosure of the source. Due to a change in the wiring (see also Sec. 3.2), it was later required to guarantee an electrical insulation of the PT100 electrode by surrounding it with thin Kapton foil, which impaired the heat conductance and lead to higher temperature readings than the actual electrode temperature. However, temperature measurement was mainly used to verify the status of the liquid N_2 flow. Liquid N_2 was supplied by a 50l dewar. With typical nitrogen pressures of 1.5 to 2bar measured above the liquid in the dewar, adequate cooling was achieved for 3–4 operating hours, with discharges dissipating a typical power of $\approx 30W$.
The discharge gas, in our case pure H_2 , is brought in through one of the three DN16CF feedthroughs. Electrical insulation of the feedthrough from anode potential was done with a Teflon hose of about 30cm length. The Teflon hose is coupled to a 3mm copper tubing which is fed into the opening in the anode electrode. The outside H_2 pressure p was measured by a Pirani gauge, about a meter away from the feedthrough, and regulated by a voltage controlled valve (Pfeiffer EVR 116). Pressure readings inside the beam pipe p_{IS} were obtained from the Penning gauge IS (see Fig. 3.13), situated in the high current injector (HSI) (see Sec. 3.4 and 4.1.1) beam line, about 50cm downstream from the source. Outside H_2 pressures were typically in the range of p = 2–25mbar, with p_{IS} ranging from 10^{-5}–10^{-4}mbar. Via calculations of the flow resistance [47], one can estimate the pressure inside the source volume p_{Source}, being approximately a factor of 10 less than the pressure outside. Using this estimation, the obtained breakdown potentials for H_2 and He gases were found to be in good agreement with the known Paschen curves (Fig. 2.1). Unless otherwise specified all given pressure values refer to the outside H_2 pressure p.
The construction of the ion source as described above meets three essential conditions. First, with the vacuum shielding of the volume where the discharge takes place, the source can be introduced directly into high vacuum ($\approx 10^{-5}$–10^{-7}mbar). Second, the geometrical arrangement of the anode and cathode makes operation in the hollow cathode regime possible with voltages of 1–2kV for the transition between glow discharge and hollow cathode discharge at pressures of p_{Source} = 0.2–2.5mbar inside the source. Third, the arrangement of anode and cathode electrodes is done so that the cathode is closer to the exit hole. This makes it possible to extract the ions directly from the negative glow region

(see Fig. 2.5).
The source design also reflects the goal of obtaining rotationally cold ions. The incoming H_2 gas flows through the channel in the anode disc (inner diameter 0.3cm, length 3cm) and through the anode cylinder (inner diameter 1cm, length 8.8cm). Both anode parts are cooled down close to liquid nitrogen temperature ($\approx$ 100K). The inner diameter of the H_2 path is always a factor of 9–10 smaller than the overall travel length of the gas molecules, thus they undergo collisions with the walls. At the same time, they undergo collisions with other H_2 molecules, since with a surrounding pressure of $\approx$ 1mbar, the mean free path of a molecule is about 7mm [48] and is smaller than the overall travel length of more than 12.8cm. Hence, the H_2 molecules equilibrate with the temperature of the walls. With a thermal distribution of rotational states that is given by

$$\mathrm{P(J)} = \frac{1}{N}(2\mathrm{J}+1)e^{-\frac{\mathrm{J(J+1)B}_{rot}}{k\mathrm{T}}} \ , \tag{3.1}$$

where B_{rot} = 14meV is the rotational constant of H_2 , J the rotational level and N reflects the total amount of rotational states. For T = 100K we obtain for the first three rotational states P(1) = 89.56%, P(2) = 10.41% and P(3) = 0.026%. Thus, almost all the H_2 molecules will be in their rotational ground state.
Additionally, the ions produced in the negative glow region situated inside the cathode travel 7–10mm in the high pressure environment, inside the source, before they are extracted from the ion source.

3.2 Wiring and field modeling

The rotational temperature of the H_3^+ ions produced in the ion source was studied with two different electrical wiring layouts displayed in Fig 3.3 and Fig. 3.5, respectively. The source characteristics was mainly studied with the type A wiring, but the characterization largely involves pure plasma parameters that do not depend on the wiring. This section will give an explanation of the different wirings and how they are realized.
The layout used initially for source tests and also for the first beamtime in January 2003, with small alterations, is the one shown in Fig. 3.3 and 3.4. The whole assembly is mounted on a high voltage platform with the potential given by $U_{Platform}$. For source testing we used a potential of 5kV, while during the TSR beamtime (see Sec. 4.3) 12kV had to be used, since the RFQ accelerator (see Sec. 4.1.1) needs an initial energy of $4\frac{\mathrm{kV}}{\mathrm{nucleon}}$. The cathode is kept on platform potential. The discharge is driven by the power supply U_{APS}, that delivers a maximum output of positive 3kV in voltage and 67mA in

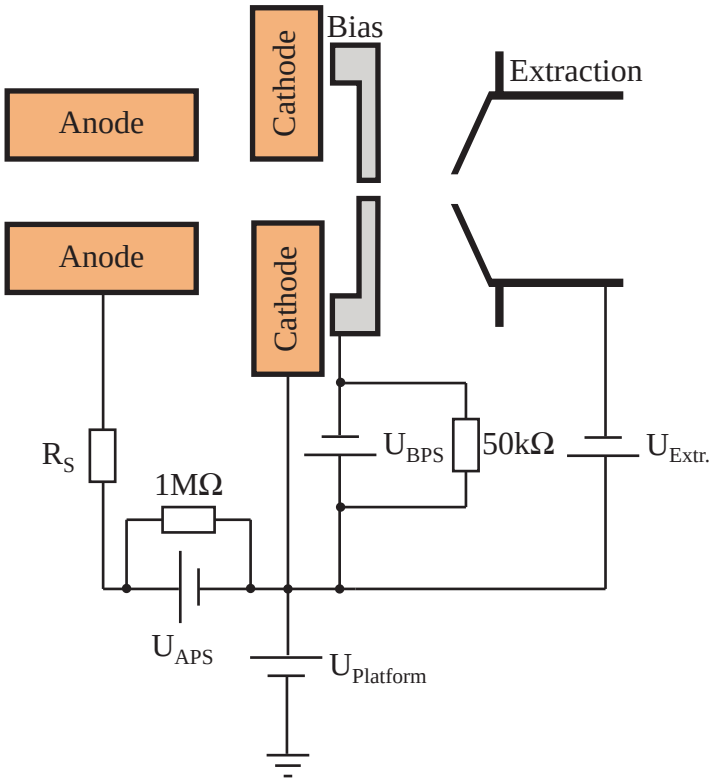

Figure 3.3: *Schematic drawing of wiring type A.*

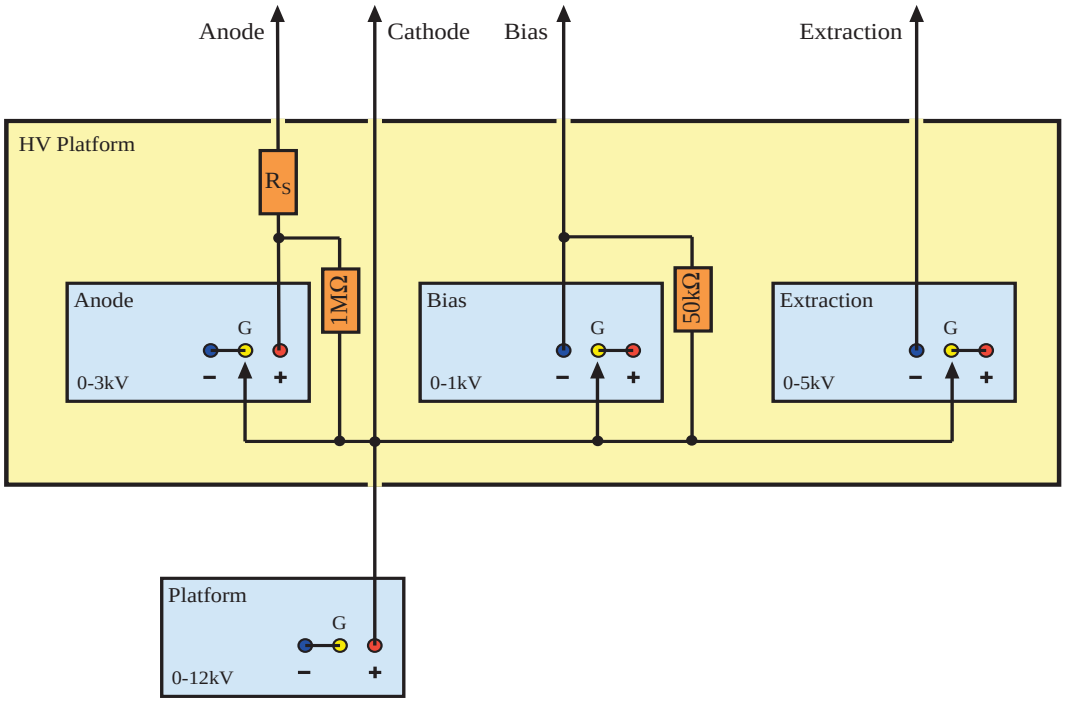

Figure 3.4: *Schematic drawing of the placement and connections of the different power supplies for wiring type A.*

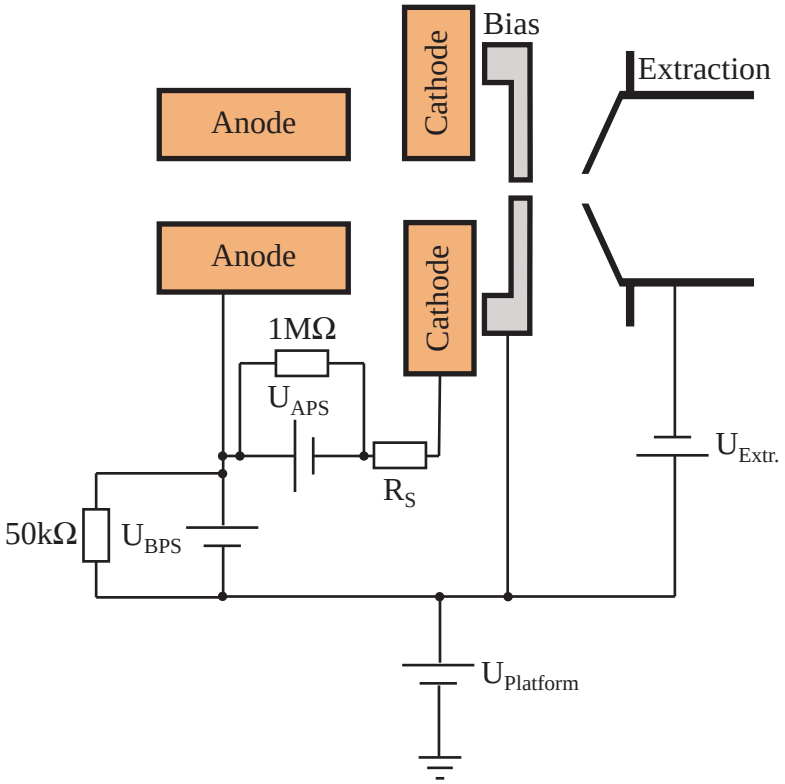

Figure 3.5: *Schematic drawing of wiring type B.*

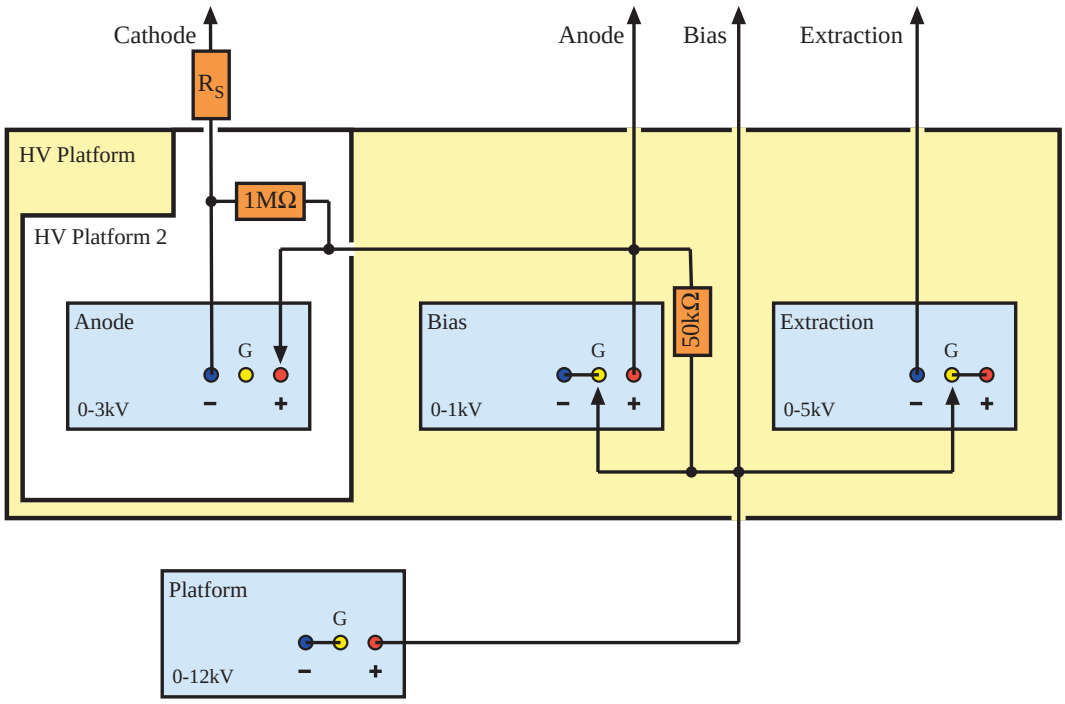

Figure 3.6: *Schematic drawing of the placement and connections of the different power supplies for wiring type B.*

current. The extraction potential and the bias electrode are lowered from the platform. $U_{Extraction}$ is supplied by a negative 5kV supply and the bias power supply U_{BPS} delivers a negative 1kV maximum voltage.

In the second beamtime in April 2003 we used another type of wiring scheme. A schematic drawing of the type B wiring is displayed in Fig. 3.5 and a figure of the placement and connections between the different power supplies can be seen in Fig. 3.6. Two distinct changes have been made. First, the bias electrode is now directly connected to the platform. Additionally, a second high voltage platform on the existing platform is created. Residing on this platform is the discharge driving power supply U_{APS}, which was reversed in polarity but still remains of the same dimension and extends downwards from the second platform defining the cathode potential. The potential of the second platform is given by the power supply U_{BPS}, a positive source with a maximum voltage of 1kV. The arrangement of the power supply delivering the extraction potential $U_{Extraction}$ remains unaltered.

Most power supplies are coupled with a parallel resistor. The resistors are indicated in the Fig. 3.3, 3.4, 3.5 and 3.6. The resistors serve as a spark protection, but also put a defined load on the supply, which improves their stability. An additional protection of the discharge driving power supply U_{APS} is accomplished by the resistor in series R_S. Typical values for the resistance of R_S ranged from 10–40kΩ. The circuit containing the resistor also includes the anode power supply U_{APS}. The anode power supply applies a potential drop over the gap between anode and cathode (discharge gap), that is filled with gas, in our case H_2 . Before the discharge is ingnited, the resistance of the gas filled discharge gap is much higher than R_S, so that the largest potential drop, in the circuit, occurs between anode and cathode. When breakdown occurs and the discharge ignites, the plamsa filling the gap becomes conducting and the resistance drops rapidly. The value of the series resistor is now larger than the resistance presented by the gas filled discharge gap and most of the voltage drop occurs at R_S. Thus, the resistor R_S serves as an additional load on the power supply, effectively limiting the current flowing through the circuit.

In order to better understand the electric field distribution inside the source we conducted a numerical modeling. In this case MAFIA [49] had to be used, since SIMION 3D cannot cope with dielectric materials and therefore was not able to take the presence of the Macor piece and the Teflon foil into account, which influence the field to a large extent. The results are displayed in Fig. 3.7 and Fig. 3.9 together with a potential distribution (Fig. 3.8 and Fig. 3.10) along the line of symmety, given by the line titled y-plane. Additionally, the influence of each electrode on the overall potential distribution is denoted by the colored curves in Fig. 3.8 and Fig. 3.10. Shown are two different settings for the bias

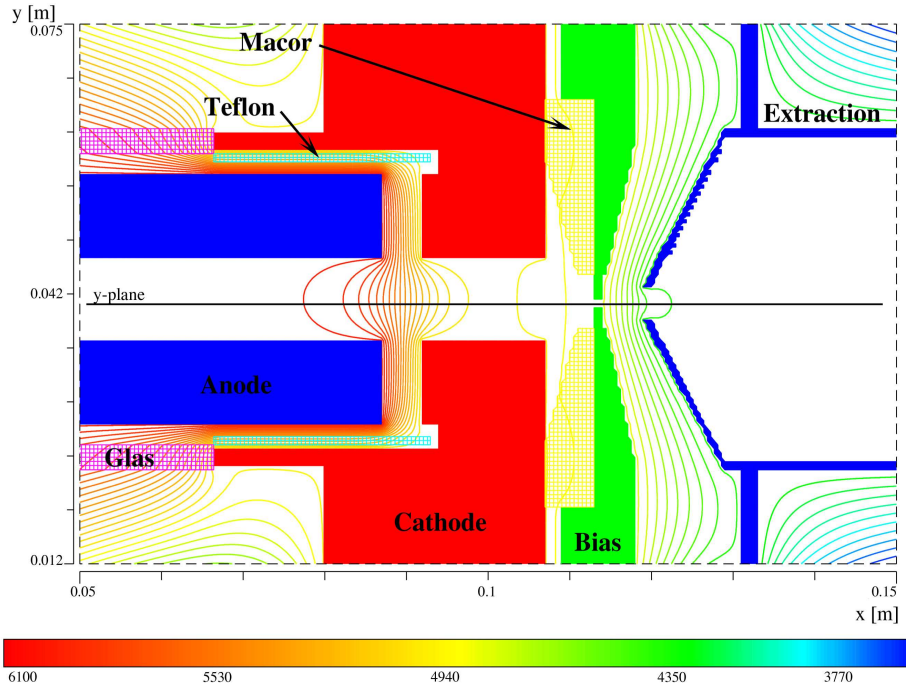

Figure 3.7: *Field modeled with MAFIA for* $U_{Bias} < U_{Cathode}$. *The settings are* $U_{Anode} = 6kV$, $U_{Cathode} = 5kV$, $U_{Bias} = 4.9kV$ *and* $U_{Extraction} = 4.4kV$. *Note the color coding of the electrode materials does not correspond to the color scaling of the potential lines, shown in the lower part of the picture.*

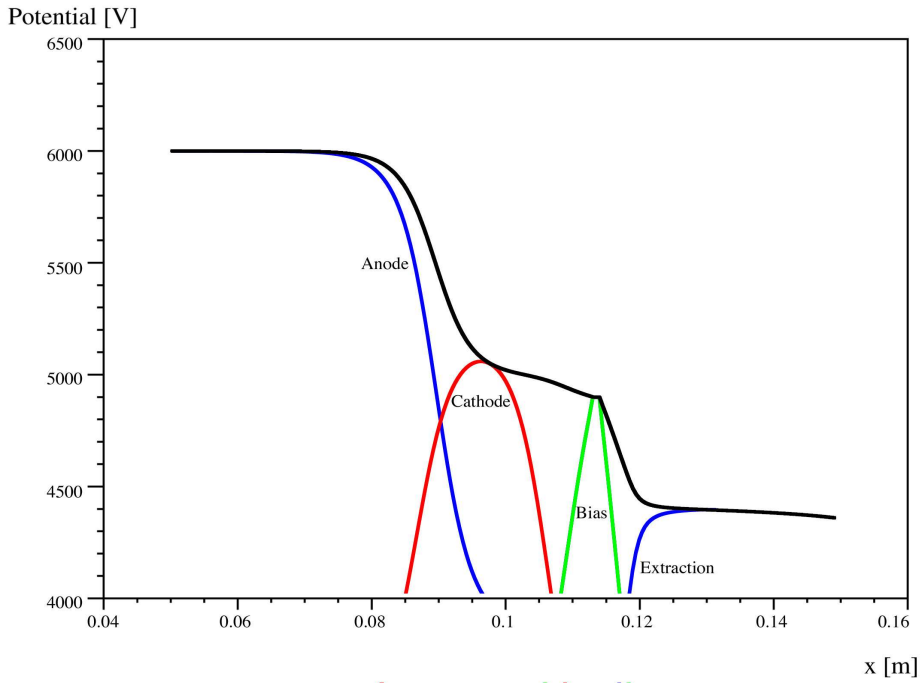

Figure 3.8: *Potential distribution of the field modeled in Fig. 3.7 along the y-plane titled line. The contribution for each electrode is denoted by the colored lines.*

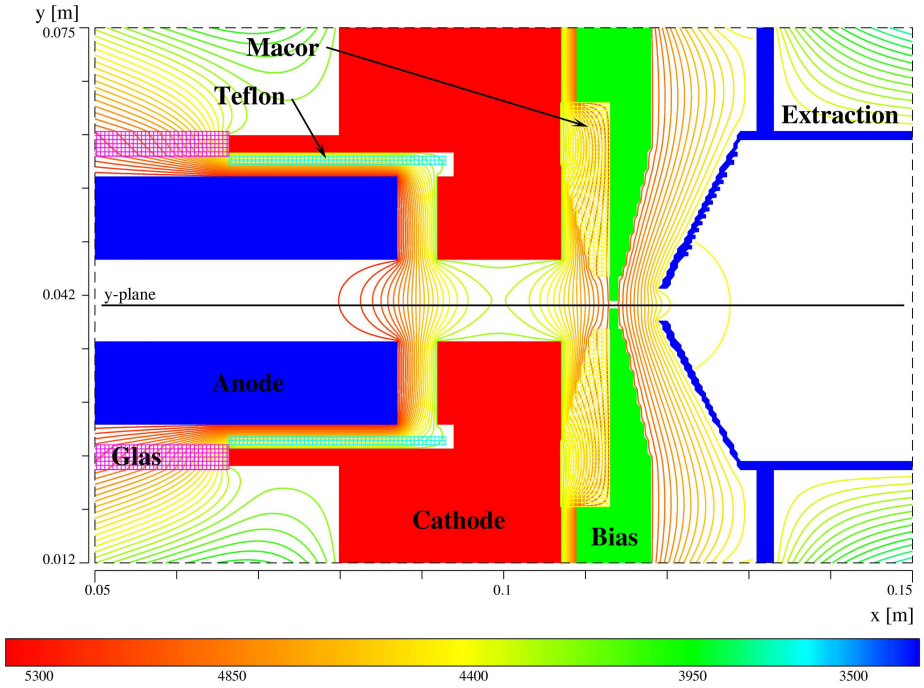

Figure 3.9: *Field modeled with MAFIA for* $U_{Bias} > U_{Cathode}$. *The settings are* $U_{Anode} = 5.2kV$, $U_{Cathode} = 4.2kV$, $U_{Bias} = 5kV$ *and* $U_{Extraction} = 4.4kV$. *Note the color coding of the electrode materials does not correspond to the color scaling of the potential lines, shown in the lower part of the picture.*

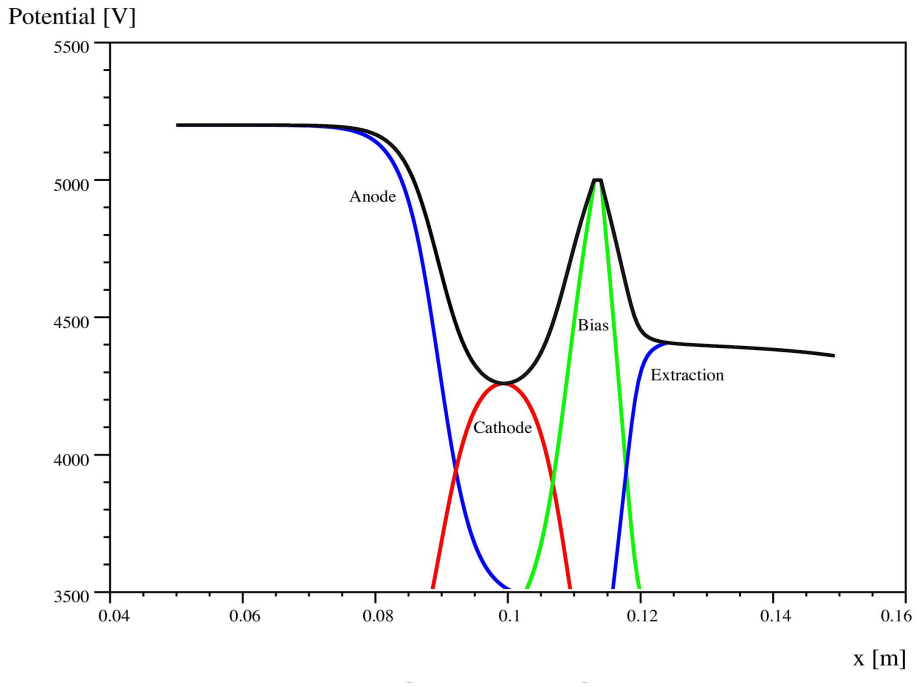

Figure 3.10: *Potential distribution of the field modeled in Fig. 3.9 along the y-plane titled line. The contribution for each electrode is denoted by the colored lines.*

electrode. Fig. 3.8 and Fig. 3.7 show a situation where the potential of the bias electrode U_{Bias} is lower than the cathode $U_{Cathode}$. The settings are $U_{Anode} = 6kV$, $U_{Cathode} = 5kV$, $U_{Bias} = 4.9kV$ and $U_{Extraction} = 4.4kV$. In Fig. 3.10 and Fig. 3.9 a situation where the potential of the bias electrode U_{Bias} is higher than the cathode $U_{Cathode}$ is displayed. The settings are $U_{Anode} = 5.2kV$, $U_{Cathode} = 4.2kV$, $U_{Bias} = 5kV$ and $U_{Extraction} = 4.4kV$.
The initial wiring type A was supposed to provide a simple wiring layout with a good transmission of the ion beam and a high ion current extracted from the source. Therefore, all power supplies were mounted on one HV platform. Additionally, the bias electrode was equipped with a negative power supply U_{BPS}, to be able to reach into the negative glow of the plasma, where most of the ions will be formed. This way of wiring corresponds to the field modeled in Fig. 3.7. In the potential distribution along the line of symmetry Fig. 3.8 one can observe a small additional potential, imposed by the bias electrode, reaching into the cathode where the burning discharge would be situated. It turned out that by using -1000V on the bias power supply U_{BPS} a stable current of up to 600nA of H_3^+ could be produced (see Fig. 3.20).
On transport through the ion source and the plasma H_3^+ undergoes collisions [50]. We consider three different types of collisions, mainly with internally cold H_2 that H_3^+ can take part in. First, H_3^+ can perform an elastic collision where momentum and angular momentum is exchanged with the collision partner

$$H_3^+ + H_2 \longrightarrow H_3^+ + H_2 \ . \tag{3.2}$$

Further, there are several reactive collisions where H_3^+ is destroyed, i.e. collision induced dissocitaion (CID), dissociative recombination (DR) and the asymmetric charge transfer (ACT) (see Sec. 2.2). The cross sections for these reactions are strong functions of the collision energy. At collision energies between 0–5eV the elastic collisions will dominate having a cross section $\sigma \approx 200 Å^2$. At higher energies (E > 5eV) the cross section for momentum transfer collisions becomes less and the reactive collisions start to play the major role. The cross section of these reaction ranges between 1–2$Å^2$.
For the production of rotationally cold H_3^+ , the H_3^+ ions need to be cooled by de-exciting collisions inside the source. While the production and destruction in a H_2 plasma is well understood, what constitutes the internal cooling of H_3^+ after production is unclear [51]. Assuming, that the cooling happens through collisions at low collision energies, i.e. through the reaction $H_3^+ + H_2 \longrightarrow H_3^+ + H_2$. One needs to introduce a way to emphasize this reaction in the plasma. In their paper published in 1997, Šimko *et al.* [50] conducted numerical simulations of the transport of H^+ and H_3^+ ions in H_2 driftubes. The

authors were able to show that the important parameter to probe different parts of the collision cross section is $^{E}/_{n}$, where E is the electric field strength and n the gas density. Therefore, we sought a way to create a potential well in which the plasma will be situated. Under these conditions the ions will perform a diffusive motion (small $^{E}/_{n}$) inside the source and by adjusting one side of the potential well, one can introduce different electric fields to probe different parts of the collision cross section.
Thus, U_{BPS} was exchanged with a positive power supply of the same dimension. This corresponds to a field modeled in Fig. 3.7, where the potential of the bias electrode U_{Bias} is higher than the cathode potential $U_{Cathode}$. Looking at the field modeled by MAFIA, accompanied again by a graph of the potential distribution along the line titled y-plane (Fig. 3.8), it becomes clear, that the bias electrode and the anode electrode form a potential well. To further improve the situation, a new type of wiring illustrated in Fig. 3.5 and 3.6 was introduced. The advantage of using this kind of wiring will be discussed in the next section.

3.3 Plasma characteristics

The ions are mostly formed in the negative glow of the discharge. That means, that the potential on which they are formed is given by the negative glow potential $U_{Neg.\ glow}$. Thus, when they are extracted from the source and accelerated to ground potential $U_{Neg.\ glow}$ will define the energy of the ions. The electrons undergo acceleration in the cathode fall region before they actually produce ions, which then form the negative glow. Therefore, the potential of the negative glow $U_{Neg.\ glow}$ is defined by the cathode potential $U_{Cathode}$ plus the potential drop over the cathode fall region $U_{Cath.\ fall}$, as described in Eq. 3.3.

$$U_{Neg.\ glow} = U_{Cathode} + U_{Cath.\ fall} \tag{3.3}$$

Due to the fact that the cathode fall constitutes the most significant voltage drop in the discharge (see Sec. 2.1.3) one can state that $U_{Cathode} + U_{Cath.\ fall} \lesssim U_{Anode}$. Therefore one obtains for the potential of the ions U_{Ion}

$$U_{Ion} \approx U_{Anode}\ . \tag{3.4}$$

Thus, for the wiring type A one obtains the following situation. The potential of the anode electrode U_{Anode} is defined by the platform plus the anode power supply U_{APS}. In addition one needs to take into account the voltage drop over the series resistor R_S given

by $U_S = I_P R_S$, where I_P denotes the current flowing through the discharge provided by the anode power supply.

$$U_{Anode} = U_{Platform} + U_{APS} - I_P R_S \tag{3.5}$$

The potential of the bias electrode is given by

$$U_{Bias} = U_{Platform} + U_{BPS} \ , \tag{3.6}$$

where the bias power supply U_{BPS} can deliver either a negative or positive output voltage. To compare the anode electrode to the bias electrode we subtract the two potentials and arrive at

$$U_{Anode} - U_{Bias} = U_{APS} - I_P R_S - U_{BPS} \ . \tag{3.7}$$

For the wiring type B the relation changes and one arrives at the following situation. The potential of the anode electrode U_{Anode} is defined by the platform plus the bias power supply U_{BPS}.

$$U_{Anode} = U_{Platform} + U_{BPS} \tag{3.8}$$

The potential of the bias electrode is given by

$$U_{Bias} = U_{Platform} \ . \tag{3.9}$$

Subtracting the anode electrode potential from the bias electrode potential we obtain

$$U_{Anode} - U_{Bias} = U_{BPS} \ . \tag{3.10}$$

In order to construct a potential well enabling a diffusive motion of the ions inside the source (see Sec. 3.2) the potential on which the ions are created U_{Ion} has to match the potential of the bias electrode U_{Bias}. Thus, with Eq. 3.4 one arrives at $U_{Anode} \approx U_{Bias}$. For the wiring type A the difference between U_{Anode} and U_{Bias} is given by Eq. 3.7. In case of a positive power supply U_{BPS} the anode potential and the bias potential can be matched for a given discharge condition $U_{APS} - I_P R_S$. If the discharge conditions changes U_{BPS} has to be adjusted according to that. Therefore, the situation where the ions undergo diffusive motion inside the source is not independent of the discharge conditions.
The difference between anode potential and bias potential in the case of the wiring scheme B is given in Eq. 3.10. Here the bias potential can be matched to the anode potential by

varying U_{BPS} and is independent of the discharge conditions. Thus, the U_{BPS} and the discharge conditions are decoupled and U_{BPS} remains constant for all discharge conditions. The current-voltage characteristic describes the actual behavior of the discharge at different operating conditions. Typically one records the current I_P flowing through the discharge against the potential drop ΔU_{Plasma} over the actual discharge. Due to the presence of the series resistor R_S, ΔU_{Plasma} can be related to the voltage of the anode power supply U_{APS} via

$$\Delta U_{Plasma} = U_{APS} - I_P R_S \ . \tag{3.11}$$

Current-voltage characteristics for wiring type A were taken for three representative pressures and are displayed in Fig. 3.12. Since the current-voltage characteristic only reflects the properties of the plasma, the Fig. 3.12 holds true for both types of wiring. We observed two modes of operation that can be very well distinguished, either by the plasma characteristics or by the optical appearance of the discharge shown in Fig. 3.11. Visible in Fig. 3.11 is the discharge when observed from the rear end of the source. Hence, the discharge is dominated by the pink color of the positive column (see Sec. 2.1.3). The bright spot in the center of the discharge is the negative glow. The original color is pale-blue, but since a hollow cathode discharge is much more intense, the light emitted from the negative glow appears white. The positive column covers all the other structures of the discharge, because they don't emit enough light intensity to be still visible through the positive column.

Looking at the the green curve ($p = 2.8\text{torr} \approx 4\text{mbar}$) in Fig. 3.12, we find the discharge to be in the abnormal glow discharge mode for anode currents lower than 12mA. To sustain a higher current flowing through the discharge a higher voltage is needed. This means (in terms of the discussion of Fig. 2.2) that the discharge already covers the complete cathode surface and can not expand anymore. In order to obtain a higher current more electrons have to be emitted from the cathode and therefore a higher voltage is needed (see Sec. 2.1.2). As can be seen in the left picture in Fig 3.11, the negative glow only consists of a small spot in the center of the discharge. If ΔU_{Plasma} approaches about 1.8kV, the discharge performs a transition to the hollow cathode regime. This is reflected in a sudden expansion of the negative glow region as illustrated in the right picture of Fig. 3.11. The negative glow is now much more intense and covers the opening on the cathode almost completely. Over the observed region of $I_P > 12\text{mA}$ the voltage remains almost constant. The slight rise in plasma voltage can be explained by the presence of a gas flow that constantly removes a fraction of the charge carriers in the discharge. Therefore, a higher

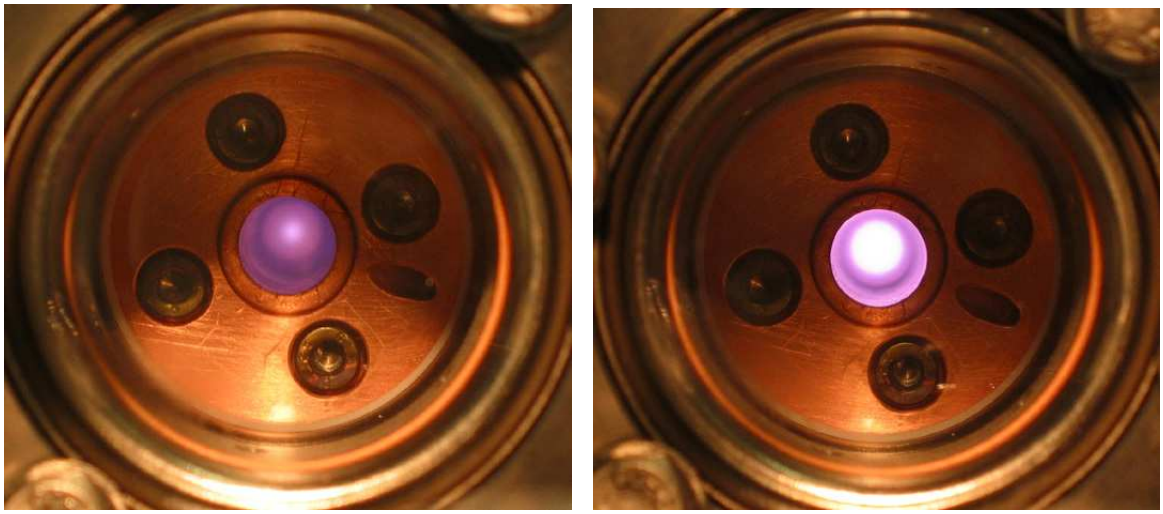

Figure 3.11: *Appearance of the discharge as seen from the outside of the source. The* **left** *picture shows the discharge regime before the transition to the hollow cathode regime has occurred. The* **right** *side illustrates the appearance after the transition.*

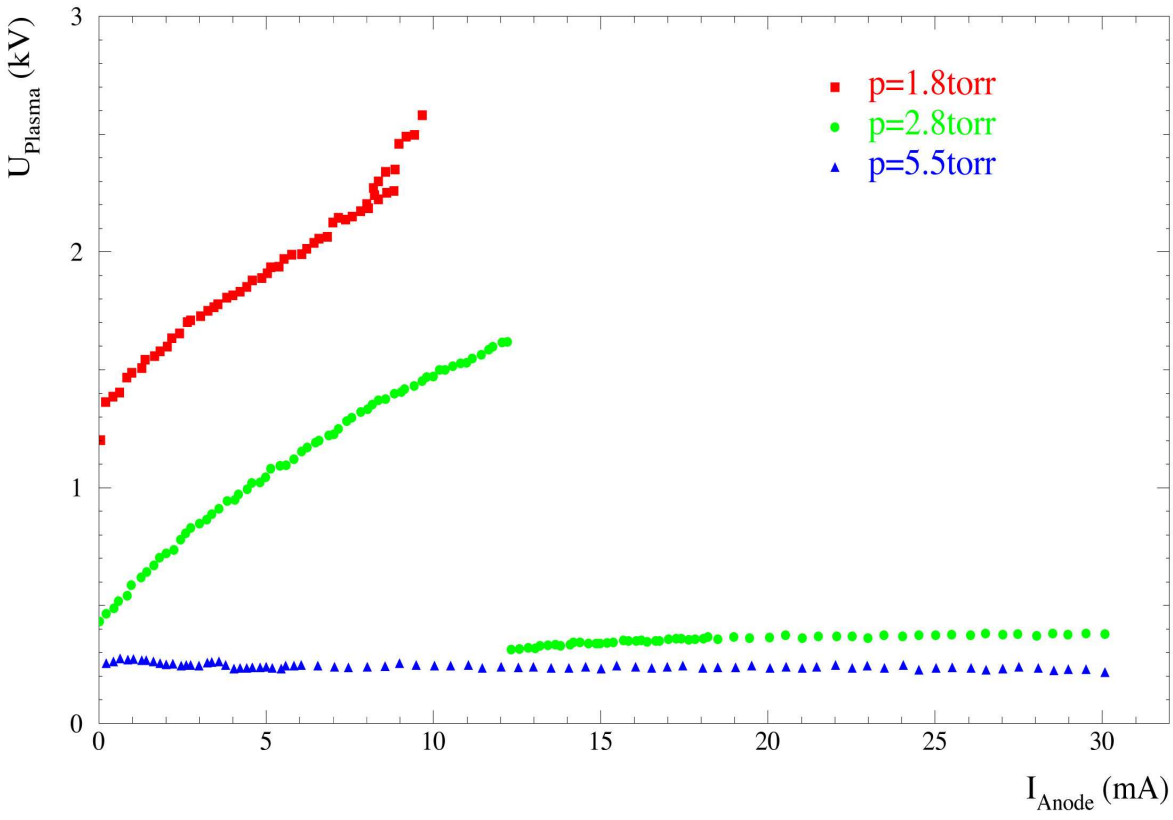

Figure 3.12: *Current voltage characteristic of a discharge in H_2 at different outside pressures p. Plotted is the anode current I_P against the voltage drop over the plasma ΔU_{Plasma}, that is given by Eq. 3.11.*

sustaining voltage is needed for compensation at higher discharge currents.
The two remaining curves show the discharge at higher pressure p = 5.5torr ≈ 7mbar and at lower pressure p = 1.8torr ≈ 2mbar. The red curve symbolizes a situation, where the potential necessary for transition to the hollow cathode mode is so high, that it cannot be reached with our means. While for the blue curve the pressure is so high, that a transition to the hollow cathode regime could only be distinguished by the optical appearance of the discharge and was found to take place at $I_P \approx 4$mA. Surprisingly, the blue curve doesn't show the same rise as the one for p = 2.8torr. This can probably be explained by the higher production of metal atoms due to sputtering from the cathode surface at higher inside pressures. Because the metal atoms have a lower ionization potential, the production of secondary electrons becomes more efficient. This results in a negative slope, which compensates the effect of the flowing gas [52].
For normal operation of the source, the outside pressure typically ranged between 3–10mbar. The discharge was usually run with a voltage setting on the anode power supply ranging from 800–1300V, while the discharge current usually was of the order of 30–55mA.

3.4 Ion yields

The final step in source characterization was to determine the different ions and their amounts produced in the source under various discharge conditions. Therefore the ion yields were examined using different setups. At first, on a test setup which was primarily used for source characterization. The test setup is a beam line with a length of about one meter mounted on a movable table. This setup is in regular use at the Max-Planck-Institut for testing of ion sources and contains a small high voltage platform to mount the source on, focusing and steering elements, a Wien filter for mass analysis and a Faraday cup for current measurements. This setup was sufficient for initial studies. However, the mass resolution of the Wien filter did not allow to distinguish ions of masses higher than ≈ 12amu. Reliable mass spectra could only be obtained with the source installed at the high current injector (HSI) (see Sec. 4.1.1).

3.4.1 Mass spectra

Fig. 3.13 shows a schematic drawing and Fig. 3.14 a picture taken of the source installed at the HSI. All source relevant installations were done inside the so called high voltage cage, enclosing all parts on high potential. All electrical connections and the gas supply were brought in through the mounting flange. The liquid nitrogen supply was implemented

with the above mentioned dewar standing on a separate insulated platform not visible on the picture, that was later moved to the outside of the cage to make dewar replacement at regular time intervals easier. The dewar was connected to the source with long Teflon wires insulated with two layers of thermal foam. This was necessary to minimize the formation of ice on the outside of the liquid nitrogen tubing. The H_2 gas is also supplied by Teflon wires, the pressure regulated by a voltage controlled valve and measured about a meter upstream from the source. The source itself was assembled as described in Sec. 3.1. It is mounted on the HV platform and put to a potential of $U_{Platform} = 12kV$, which delivers an initial kinetic energy of $4\frac{kV}{nucleon}$ in the case of H_3^+ , needed for later acceleration. The ions are extracted by the extraction electrode and then accelerated when they pass on to the first electrode of the Einzel lens (see Fig. 3.13 and Fig. 3.14), that is situated on ground potential about 2cm away from the end of the extraction electrode. Via the lens the beam can be focused into the magnet, where it will be separated according to the ions' mass to charge ratio. The beam then passes a magnetic x-y steerer and a magnetic lens triplet before it is injected into the RFQ accelerator. A more detailed description of the high voltage cage used for source installations and the facilities utilized for beam diagnostics can be taken form Fig. 3.14 and can be found in the publications by von Hahn and Grieser [53, 54].

A mass spectra is obtained by slowly sweeping the magnetic field strength while recording the ion current on the Faraday cup FC0. The mass charge ratio can then be determined with the help of the formula

$$\frac{m}{q} = \frac{r^2B^2}{2U_{Platform}} , \tag{3.12}$$

where B is the magnetic field strength (ranging from 0–4.5kG), the nominal radius of curvature r=29cm and the acceleration voltage $U_{Platform} = 12kV$. To compensate for inhomogeneities in the magnetic field and small errors in field measurement due to misplacement of the Hall probe the magnetic field B was replaced with an effective field $B_{eff} = B(1 + g)$ which incorporates a correction g that was fitted to the data.

With this in mind, the interpretation of the spectra shown in Fig. 3.15, Fig. 3.16 and Fig. 3.17 can be addressed. All spectra were taken with the type B wiring (Fig 3.5 and Fig. 3.6), the first two with a very high setting on the bias power supply, namely $U_{BPS} = 0.6kV$ and the last one with a lower setting of 0.24kV. Important to note is the fact that these spectra were taken with a software that was still in a beta state. The software simply reads out magnetic field and cup current values from the data acquisition (DAQ). Due to transmission problems it can occur that the data acquisition does not

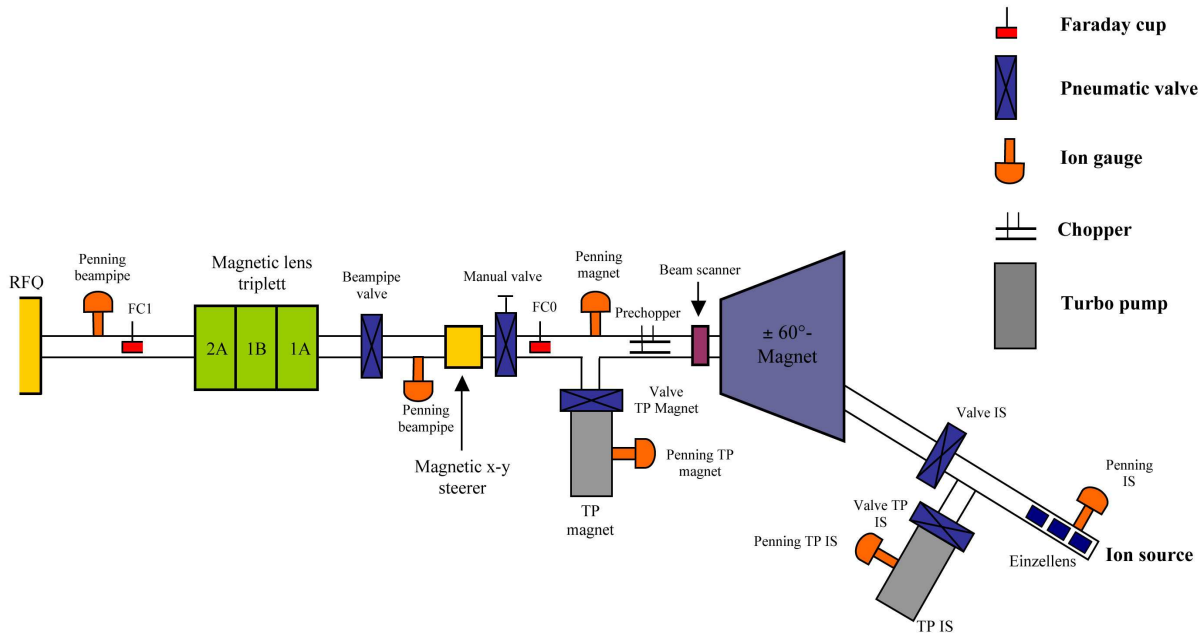

Figure 3.13: *Schematic overview of the high voltage cage installation in use for ion production for the high current injector at the Max-Planck-Institut für Kernphysik in Heidelberg, including vacuum system and beam diagnostics.*

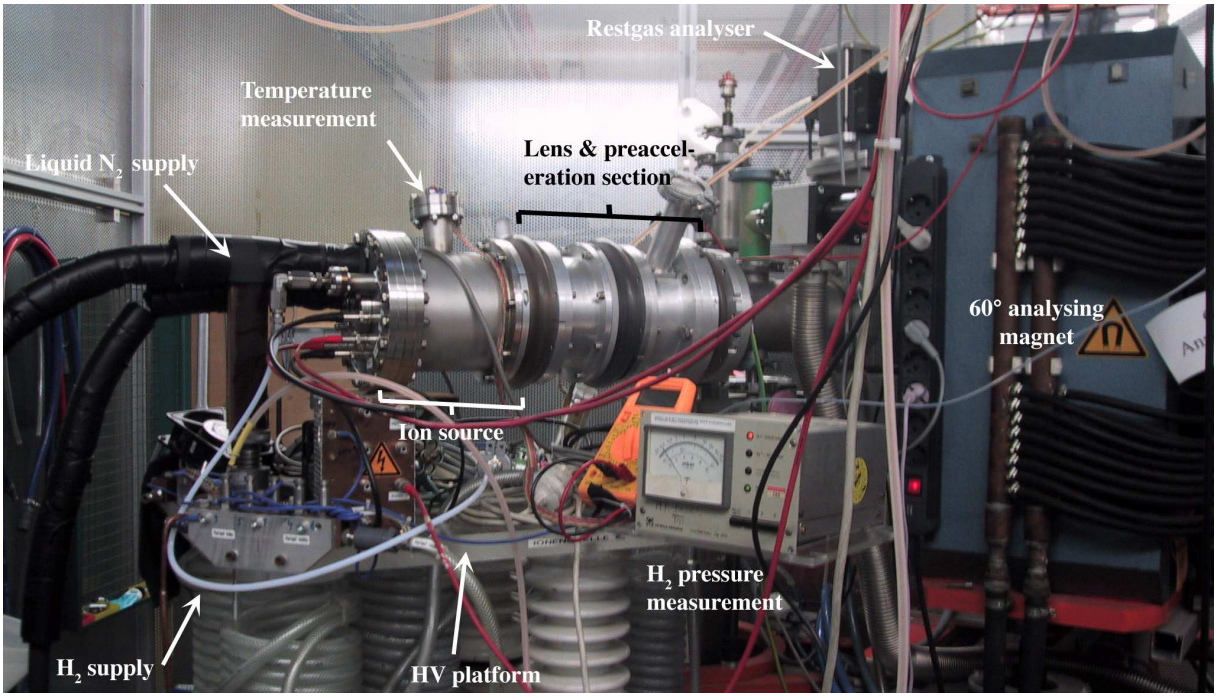

Figure 3.14: *Photo taken of the hollow cathode ion source installed at the high current injector in January 2003.*

return a value and then the software writes down a zero in the data file. This is a well understood problem that occurs in the interplay between software an DAQ and will be taken care of in a later version of the software. However, in our case this can sometimes lead to zero current values even within the peaks.

The high setting describes a situation where the motion of the ions inside the source is not diffusive (see Sec. 3.2), since the cathode potential was clearly higher than the platform. Looking at the spectra taken over almost the complete magnet range, one can assign the two high mass peaks at around 65amu to the two copper isotopes ^{63}Cu and ^{65}Cu. The natural ratio of these two isotopes is 69.17% for the ^{63}Cu and 30.83% for the ^{65}Cu which supports the interpretation, since the intensities agree quite well with the experimental measurements. The intensity of the ^{63}Cu peak was found to be 26.7nA and that of the ^{65}Cu peak was 13.4nA, which gives a ratio of 66.6 to 33.4. The origin of these ions is caused by sputtering of cathode material that was already predicted from the results of the current voltage characteristics, although these were taken at a much lower discharge current (see Sec. 3.3). At lower masses another prominent peak at around 28amu is observed, that can be assigned to singly ionized nitrogen molecules resulting from restgas still present in the source or small leakages in the cooling lines. Turning to the lower masses which were taken at better resolution on Fig. 3.16, we observe a 5-peak structure ranging from mass 14 to 18. There are several ions that can be related to these peaks. The mass 18 is very likely to result from water, which should still be present inside the source to a large extent since it naturally is not baked. Additionally, fragments of H_2O^+ namely HO^+ and O^+ should be taken into account, creating the peaks at mass 17 and 16. The very small peak at 14 can be attached to the singly charged nitrogen ion, the amount of which being surprising at first, when at the same time the molecular ion is so likely to find, one would expect a higher intensity. However, due to the strongly nucleophile character of the N^+ ion and at the same time the presence of the strongly protonating agent H_3^+ , it will be transformed to NH^+ and even further to NH_2^+, NH_3^+ and NH_4^+ since they are still strongly nucleophile agents, resulting in the peaks 15, 16 and furthermore contributing to the ones at 17 and 18. The most prominent peaks in the spectrum result from the hydrogen ions formed in the discharge. A stable current of H_3^+ totaling to about 640nA could be extracted from the source under these circumstances but also a quite strong current of H^+ was found and H_2^+ being the least favored ion. This is due to the fact that the conditions applied here boost the formation of the secondary ions H_3^+ and H^+ according to the Eq. 2.3 and the breakup reaction of H_2^+ . Both processes lead to the disappearance of H_2^+ ions from the discharge (see also Sec 2.2).

The spectra of the lower bias setting is displayed in Fig. 3.17. The most striking difference

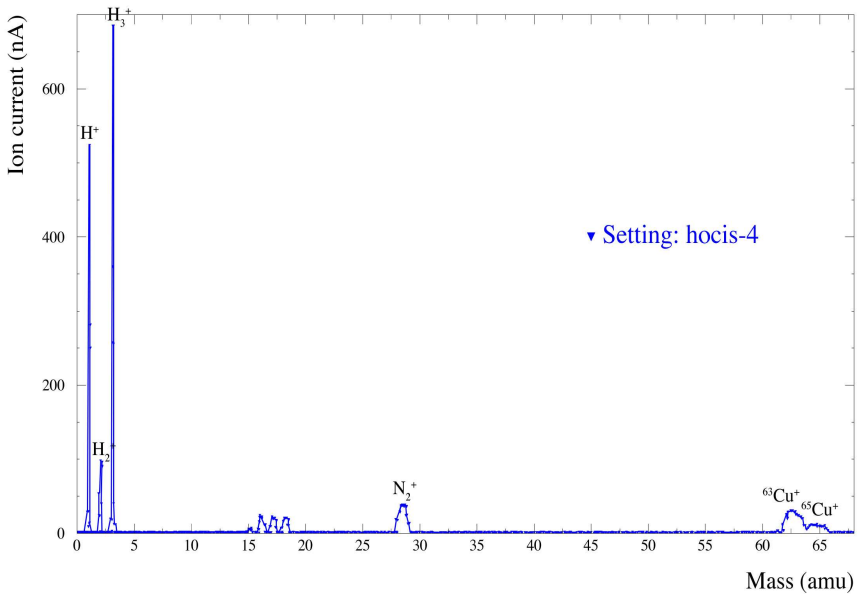

Figure 3.15: *A mass scan over the whole magnet range. The source was wired according to type B(see Fig 3.5). Settings: HOCIS-4;* $p = 5torr$, $U_{BPS} = 0.6\text{kV}$, $U_{APS} = 0.9\text{kV}$, $I_P = 55\text{mA}$.

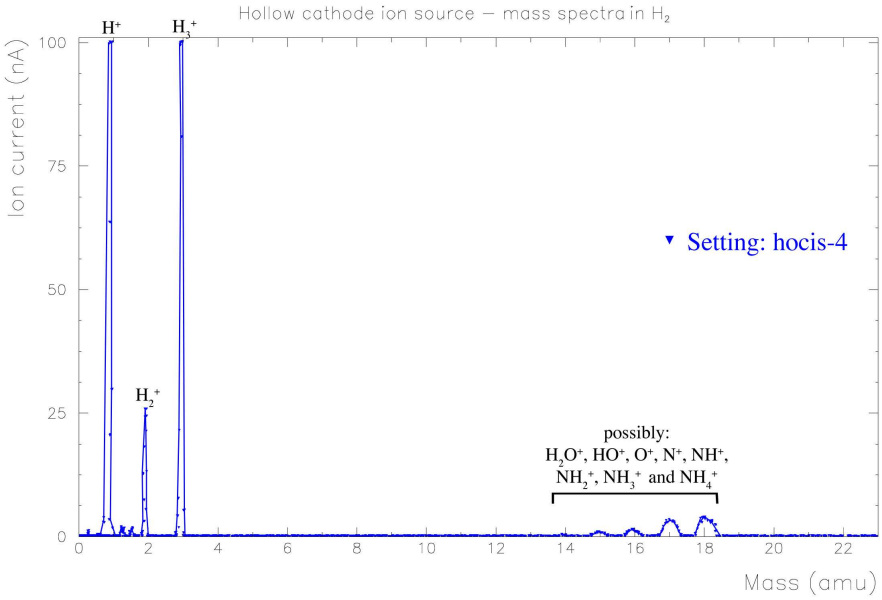

Figure 3.16: *Scan under similar conditions as Fig. 3.15, except with higher resolution and only masses up to 22amu are covered. Note that both peaks* H^+ *and* H_3^+ *saturate, due to different scaling on the y-axis.*

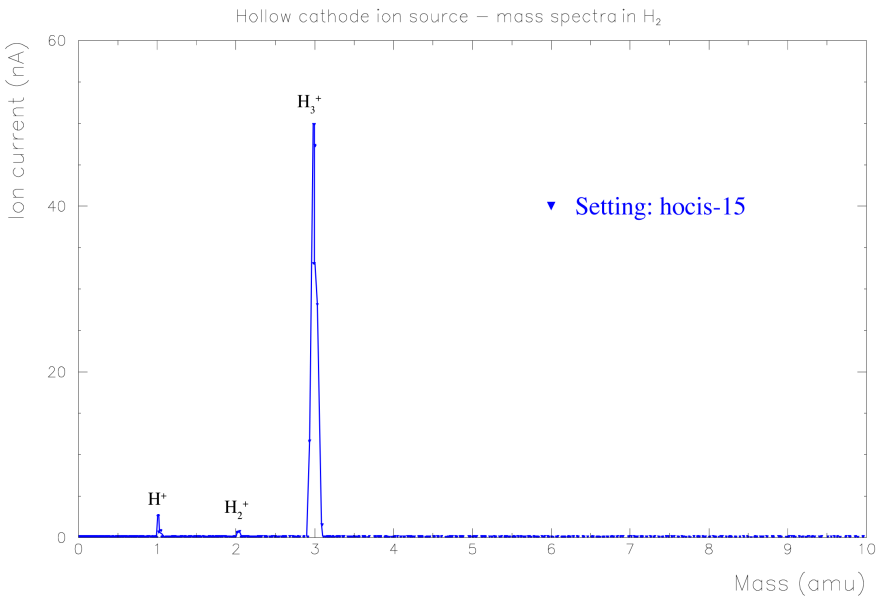

Figure 3.17: *The source was wired according to type B. The mass scan was only done over the low mass range, since no other peaks were found at higher masses. Settings: hocis-15;* p ≈ *5torr,* $U_{BPS} = 0.24\text{kV}$, $U_{APS} = 1.24\text{kV}$, $I_P = 55\text{mA}$.

between the two settings found in the mass spectra is first the significant reduction of current and also the complete absence of any other particles except for H^+ , H_2^+ and H_3^+ . Which can be explained simply by the fact that no extracting field is imposed by the bias electrode. Thus, only a small portion of the produced ions is actually extracted from the source. Thus, the non-existence of particles in the spectra simply results from the reduction to amounts that are not detectable with our means anymore. More interesting is the change of the production ratios of the three hydrogen ions. H_3^+ now clearly dominates the spectrum while H^+ and H_2^+ are hardly recognizable. This reflects the different mobility of the ions in H_2 [50] and will be addressed in the next section.

3.4.2 H^+ , H_2^+ and H_3^+ ion yields

Fig. 3.18 shows the yields of H^+ , H_2^+ and H_3^+ ions extracted from the source at different anode currents. This figure was taken on the test setup with the wiring type A but the same dependency should hold true for type B. All ions benefit from higher anode currents, i.e. higher plasma intensities. H_3^+ (red curve) profits the most with the associated ion current always being clearly higher than any other ion. H^+ is also produced in large quantities but doesn't benefit from higher plasma intensities as much as H_3^+ does. Compared to H^+ and H_3^+ , the H_2^+ ion is only produced in small amounts.

In Fig. 3.19 the pressure dependency of the ion currents has been studied and was found to be similar for both types of wiring. As expected, the pressure dependency shows that under these discharge conditions the production of secondary ions is the dominating process. At low pressures, H_3^+ is the dominating ion. In addition, a strong current of H^+ is delivered from the source. The current of H_2^+ is about one order of magnitude lower than that of H_3^+ . With increased pressure the prevailance of secondary processes increases, making H_2^+ almost disappear from the discharge. Similarily, the yield of H_3^+ current also decreases although not as significant as for H_2^+ . Over the observed pressure regime, the H^+ current remains almost static and shows only a small decrease at pressures higher than 5.5torr.

For the wiring type A, the influence of the bias electrode on the ion yields was monitored and is displayed in Fig. 3.20. With increased potential applied to the bias electrode, the H_3^+ current increases by more than 30% and arrives at a maximum of 600nA at a bias voltage of $U_{BPS} = -1\text{kV}$. In contrast, with increased bias potential the H_2^+ current remains more or less constant, while the H^+ ion current shows a small decrease.

The bias dependence was also taken for the second type of wiring B and is shown in Fig. 3.21. The results differ to a large extent when compared to Fig. 3.20. For bias

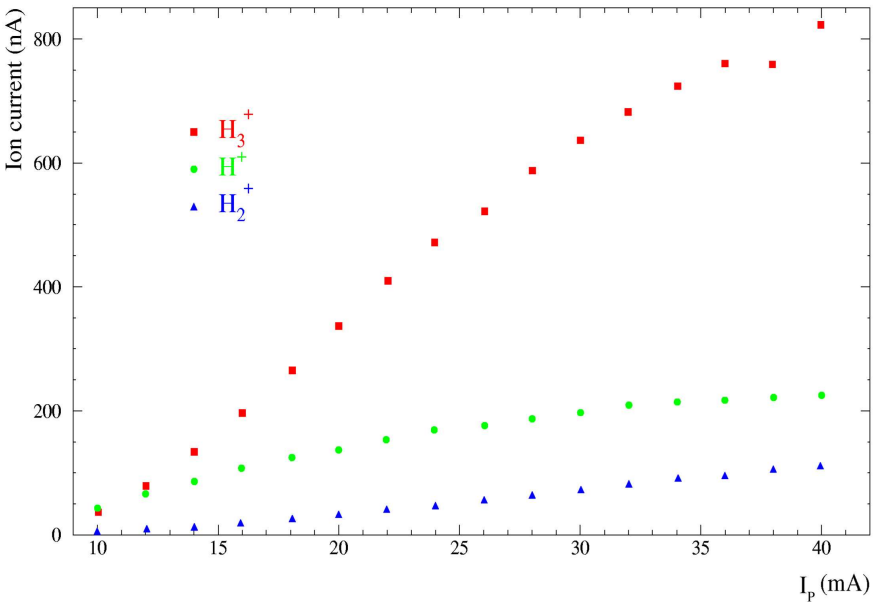

Figure 3.18: *The behavior of the obtained ion current for different discharge currents and at a constant pressure of $p = 4$torr for H^+ , H_2^+ and H_3^+ is shown. It is clearly visible that at all discharge intensities H_3^+ is the dominating ion, while H_2^+ is the least favored one as stated in Sec. 2.2. The spectrum was taken for wiring A but was similar for wiring B.*

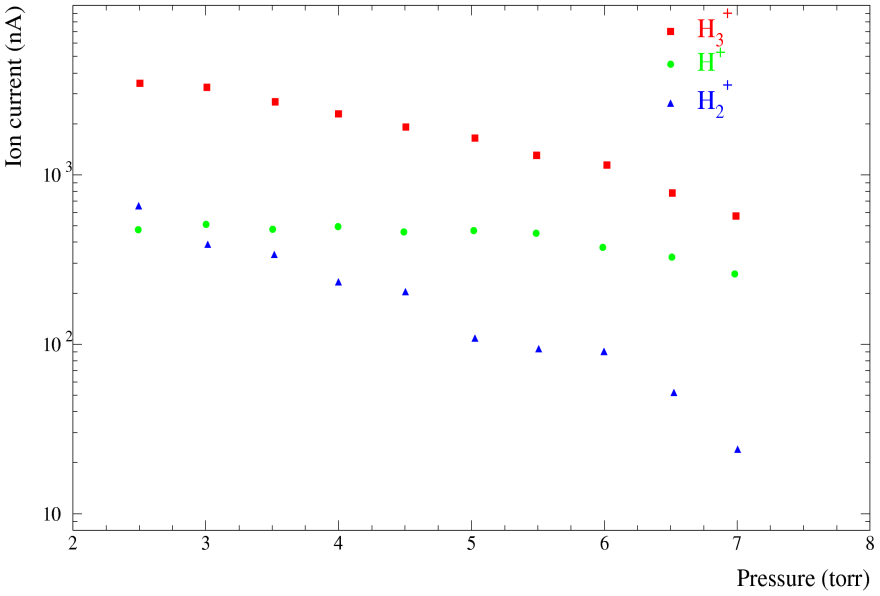

Figure 3.19: *Pressure dependence of the ion currents of H^+ , H_2^+ and H_3^+ . The spectrum was taken for wiring A but was found to be similar for wiring B.*

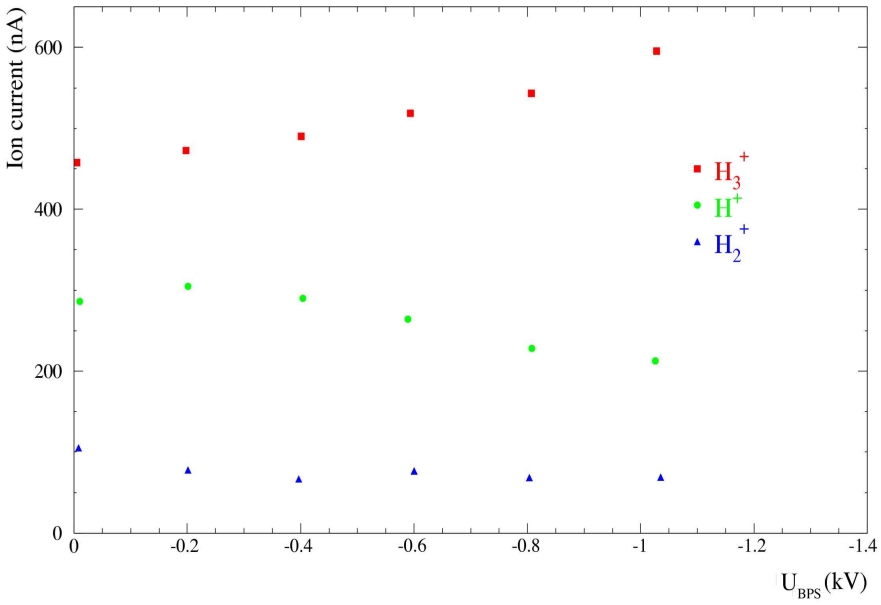

Figure 3.20: *Ion current versus different settings on the bias electrode taken at a constant outside pressure of $p = 4.5$torr for wiring type A.*

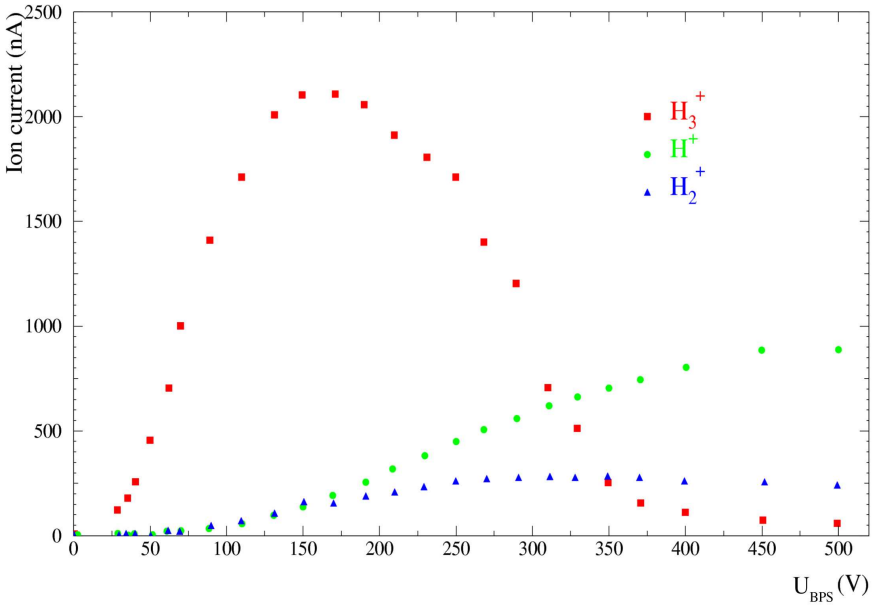

Figure 3.21: *Ion current versus different settings on the bias electrode taken at a constant outside pressure of p = 4torr for wiring type B. The spectra was taken for a freshly clean source, see Text for further details.*

voltages lower than ≈ 300V H_3^+ remains the dominating ion in the discharge undergoing a maximum at around 170V. At higher bias voltages, the extracted H_3^+ current drops turning H_3^+ in the least favored ion to be extracted, for high bias settings of 350V and higher. For low bias settings, H^+ and H_2^+ are strongly suppressed and only a few nA could be extracted from the source. At around 80V the obtained current of both ions rises. While H_2^+ undergoes a maximum at around U_{BPS} = 300V and remains constant, the H^+ current rises continuously over the whole observed bias voltage range and becomes the dominating ion, at bias voltages higher than 320V.

In Fig. 3.22 the bias current versus the bias voltage is plotted. During operation of the source in the April 2003 beam time it became apparent, that the bias electrode can also interact with the discharge. This conclusion could be derived from the observed amount of current delivered by the bias power supply. In Fig. 3.5 and Fig. 3.4 a schematic drawing of the type B wiring including all resistors was presented. As seen from the wiring diagrams, the current delivered by the power supply should only be given by the parallel resistor (R_{Bias} = 50kΩ), because the remaining circuit only imposes a capacitive resistance. The current voltage-characteristic of the bias power supply without a burning discharge (green curve) was measured and is displayed in Fig. 3.22. From the slope of the green curve a resistance of 49.3kΩ can be derived. Taking into account an inaccuracy of 2% in the indicated resistance of 50kΩ, the calculated value is in good agreement with the obtained

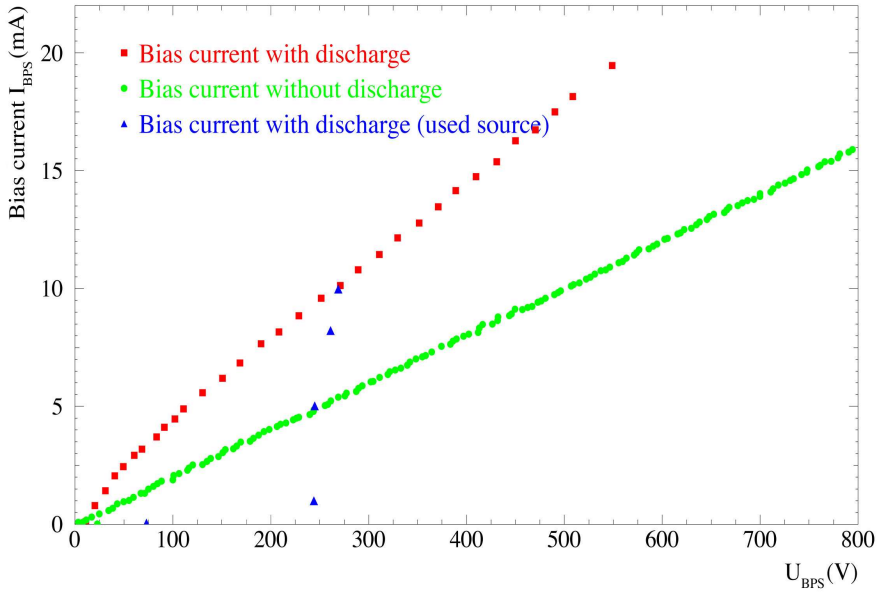

Figure 3.22: *Bias current I_{BPS} versus bias voltage U_{BPS} taken at a constant outside pressure for wiring type B, once without a running discharge (green curve), with running discharge for a freshly cleaned source (red curve) and for a source that has been running for several days (blue curve).*

value. The behavior changes if a burning discharge is present as indicated by the red curve in Fig. 3.22. For a low bias voltage the current is now almost zero. It then rises suddenly above the nominal value given by the green curve. For higher bias voltage settings a linear dependence is detected but the slope is different from the green curve. From the slope of the red curve at voltage settings higher than 150V, one can deduce a new resistance of 27.5kΩ. Another current voltage characteristic of the bias taken after the source had been in use for a couple of days (blue curve) showed that this dependency changes significantly over time. While the general behavior of showing no current at low voltage settings and then undergoing a sudden increase above the nominal value, can be said to be the same, the voltage value where the green curve and the blue curve cross is now shifted to higher values.

Summarizing the above given dependencies one can conclude the following. The pressure dependence behaves as expected (see Sec. 2.2). At low pressures, H_3^+ was the dominating ion making the neutral-ion collision process given in Eq 2.3 the most favored reaction process. With an increase in pressure the amount of H^+ ions produced in the breakup of H_2^+ by collisions remains almost constant while the amount of H_3^+ is diminished. H_2^+ showed an overall decrease over the whole observed pressure regime owing to the fact that at high pressure more and more H_2^+ ions react forming secondary ions, namely H_3^+ or H^+ . Looking

at the dependence of the ion currents on the discharge intensities, an overall increase of ion currents at higher discharge currents can be observed. At higher discharge currents more electrons are emitted from the cathode surface, resulting in the production of more ions. Since, at the applied pressure of p = 4torr, H_3^+ is the dominating ion (see Fig. 3.19) it becomes clear that H_3^+ will profit most from an increased electron density in the discharge, while H_2^+ and H^+ don't benefit as much.

Comparing the different dependencies on the bias potential for the two types of wiring schemes (Fig. 3.20 and Fig. 3.21) one can see that for wiring type A the bias electrode forms an extraction potential reaching into the discharge and yields higher currents of H_3^+ . The fact that one only observes an increase in H_3^+ current further supports the theory that we are in fact probing into the negative glow region, since the largest quantity of H_3^+ ions should be located in this discharge region (see Sec. 2.2).

Looking at Fig 3.21, one can see that H_3^+ undergoes a maximum, while H^+ rises steadily. The peak structure of H_3^+ essentially reflects the H_3^+ mobility in H_2 [50] which is a function of $^{E}/_{n}$, with E the electric field and n the gas density (see also Sec. 3.2). Thus, one can, in principle, calibrate U_{BPS} for a given pressure to the value of $^{E}/_{n}$. In this way one can control the dominating reactions in the plasma [50]. This is reflected in the peak structure of the H_3^+ curve. At low bias settings ($U_{BPS} < 170V$), i.e. low $^{E}/_{n}$, elastic collisions (see Sec 3.2) dominate, while at high bias settings ($U_{BPS} > 170V$) destructive collisions (see Sec. 2.2) play a major role, leading to a decrease in H_3^+ current. The basic idea is now to measure the rotational excitation of the ions for different bias voltages. However, the picture in Fig. 3.21 was obtained for a freshly cleaned source and a different Macor piece (see Fig. 3.1). Due to excessive coating inside the source, that developed during the April 2003 beamtime, the Macor piece had to be replaced by a spare part that differed from the original one. Because of these problems with the ion source the H_3^+ versus bias voltage spectrum was shifted to higher U_{BPS} values. Therefore, the results for the rotational excitation cannot be directly related to Fig. 3.21.

From the Fig. 3.22 we can derive that the bias electrode can also influence the burning discharge. This assumption can be derived from the changed slope observed in the red curve. The obtained resistance of 27.5kΩ is less than the original value of about 50kΩ. This suggests that a second parallel resistor is present in the circuit with a value of $\approx$ 61kΩ. This second parallel resistor can only result from the gaseous medium in the source, which becomes conductive. It is conceivable, that at high bias voltage settings a second discharge is ignited close to the bias electrode. The observation that the current voltage characteristic is dependent on usage time might be due to the fact that the plasma conditions cannot be guaranteed to be the same. For instance, the inside pressure could

be different. But also the above mentioned source problems could play a role.

4. Rotational temperature measurements of the H_3^+ ions

To investigate the rotational temperature of the ions produced in the hollow cathode ion source, the dissociative recombination of the produced H_3^+ ions with electrons at zero relative energy was studied. As experimental technique heavy ion storage ring particle imaging was utilized.
The dissociative recombination of H_3^+ (ν,J) in rotational (J) and vibrational (ν) levels can be formally expressed:

$$H_3^+(\nu, J) + e^- \longrightarrow \begin{cases} H(1s) + H(1s) + H(1s) & +4.76eV + E(\nu, J) \quad (a) \\ H_2(\nu', J') + H(1s) & +9.23eV + E(\nu'', J'') \quad (b) \end{cases} \tag{4.1}$$

with a probability of 75% for channel **a** and 25% for **b**, respectively [55]. In the two-body channel (Eq. 4.1b) the energy release is shared between the internal excitation of the molecular fragment and the relative kinetic energy of the two fragments. In the three-body channel (Eq. 4.1a), the total kinetic energy release (KER) should amount to 4.76eV plus E(ν,J) , as no internal excitations of the fragments are possible. The energy E(ν,J) comprises the vibrational and rotational excitation energy of the H_3^+ ions. Thus, a measurement of the kinetic energy release of the three body channel yields information on the initial energy, i.e. rovibrational excitation of the H_3^+ ions.
In the experiment the H_3^+ ions are produced in the hollow cathode source. They are accelerated and injected into the heavy ion storage ring. The ions circulate in the storage ring and are overlapped by an intense electron beam. The relative electron energy is only $\approx$ 10meV. The H_3^+ ions combine with the electrons and dissociate. The neutral fragments leave the storage ring and are recorded on an MCP detector. The sum of the squared distances of the recorded neutral particles is proportional to the total kinetic energy release. Earlier experiments [16] using the Coulomb explosion imaging technique (CEI) [56] have shown that the H_3^+ ions are vibrationally cold after 2s of storage in the

storage ring. On the other hand, rotational excitations have to be expected to be still present in the beam, since the rotational relaxation of H_3^+ in the vibrational ground state by radiative transitions is expected to be slow, due to the vanishing dipole moment. Thus, the measurement of the KER of the H_3^+ ions in the three body channel after storage times of 2s and higher yields information on the rotational excitation of the ions.
In Sec. 4.1 the ion beam acceleration system will be described. The Heidelberg heavy ion storage ring TSR together with the electron cooler will be covered in Sec. 4.1.2 and Sec. 4.1.3. In Sec. 4.2 the setup of the imaging detector will be illustrated and in Sec. 4.3 the results of both beam times in January and April 2003 will be covered.

4.1 Beam acceleration and the test storage ring TSR

4.1.1 The high current injector HSI

The ion production facilities for the HSI where already discussed in Sec. 3.4. In addition to the hollow cathode ion source a CHORDIS (**C**old **HO**t **R**eflex **D**ischarge **I**on **S**ource) [57] was simultaneously installed. The CHORDIS was installed for two purposes. First, it can produce several micro ampere of H_3^+ and was used to have sufficiently high beam intensity for ring and cooler preparation. Second, the rotational excitation of the H_3^+ ions produced in the CHORDIS were used as a direct comparison to the H_3^+ ions produced in the hollow cathode source. Both sources are completely different in design. The CHORDIS is a filament source, where the filament will be heated to $\approx$ 1500K. The hollow cathode ion source features a self-sustained discharge, where the H_3^+ is produced in a cold environment, because the supplied H_2 gas is rotationally cold. So we can expect the ions from the CHORDIS to show a higher rotational temperature.
The accelerator section of the Heidelberg HSI [54] includes two radio frequency quadrupole (RFQ) resonators [58] and eight seven-gap resonators [53] a schematic drawing of this system is displayed in Fig. 4.1 and a picture along the beam line is shown in Fig. 4.2. A RFQ resonator is an efficient device for acceleration of slow ion beams and both RFQs are designed to accelerate a minimum charge to mass ratio of 1:9, yielding a total energy of up to $0.5\frac{\text{MeV}}{\text{nucleon}}$ for both resonators. The beam is then transfered to the eight 7-gap resonators via a matching section. The 7-gaps additionally provide an energy of $1.2\frac{\text{MeV}}{\text{nucleon}}$. Thus, a total energy of about $1.7\frac{\text{MeV}}{\text{nucleon}}$ can be obtained for the complete HSI.
The high current injector is connected via a transfer beam line to the storage ring. The transfer beam line includes several dipole magnets for mass separation, focusing units and a post accelerator, which is made up of several RF resonator structures, similar in design

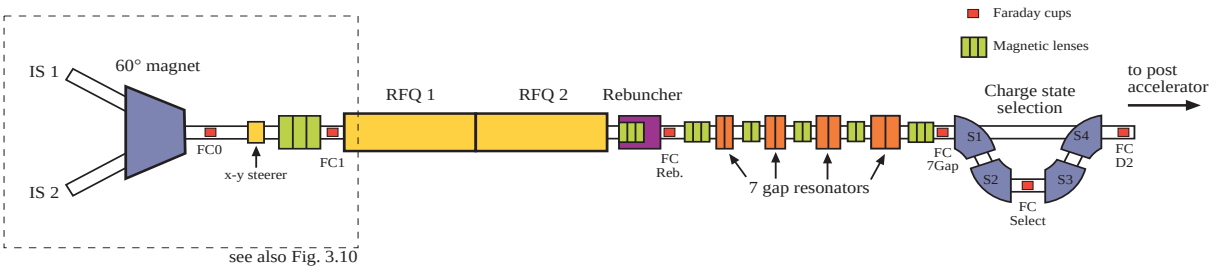

Figure 4.1: *Schematic drawing of the Heidelberg high current injector. Shown is the present status with two RFQ's, the eight 7-gap resonators, the four charge state selecting magnets together with the main focusing and diagnostic parts.*

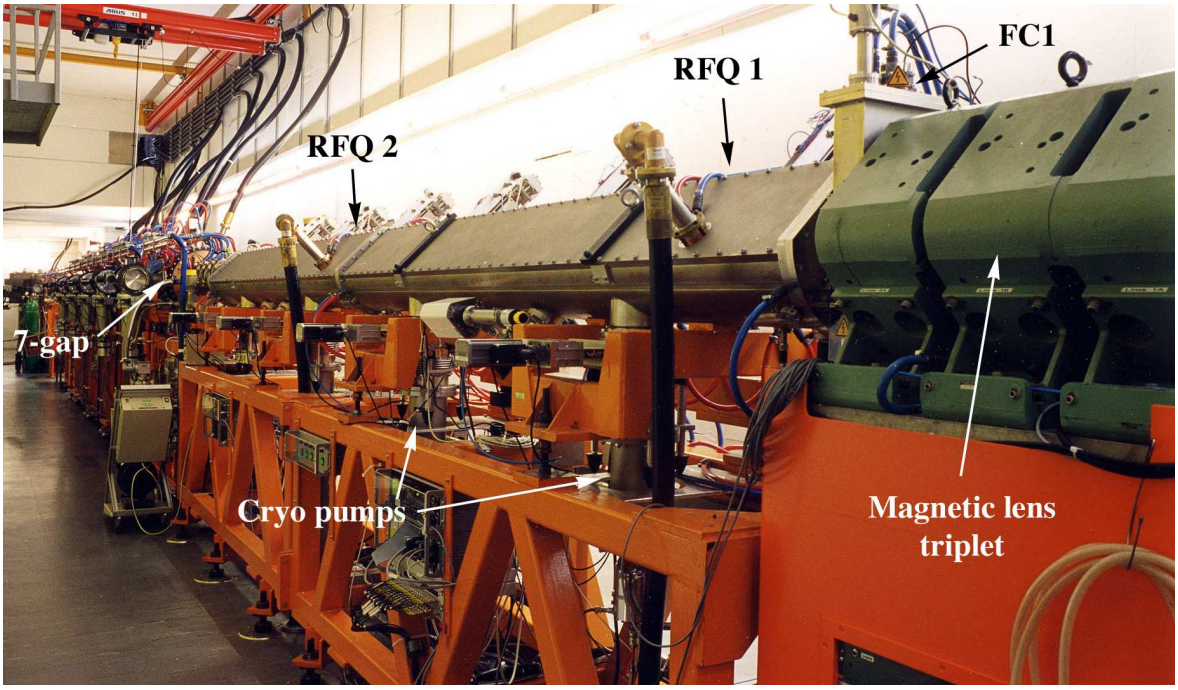

Figure 4.2: *The Heidelberg high current injector. The picture was taken from the beginning of the acceleration section along the beam line. Both the RFQ's and the resonators can be nicely seen.*

than the 7-gaps used in the HSI, that can be used for further acceleration, but was not utilized in out experiments.

4.1.2 The Heidelberg test storage ring TSR

A schematic drawing of the test storage ring (TSR) situated at the Max-Planck-Institut für Kernphysik in Heidelberg is shown in Fig. 4.3. The TSR started operation in May 1988 [59] and was in the beginning mainly used for experiments with atomic ions. In the recent years it has been taken advantage of the capability to store molecular ions for up to a couple of minutes. For molecular ions, the storage time is mainly limited by destructive collisions with residual gas molecules. The residual gas in the TSR consists mostly of H_2 and constitutes a background pressure of $5 \cdot 10^{-11}$mbar.
A detailed description of the TSR was given by Baumann *et al.* in 1988 [60]. The test storage ring is equipped with eight dipole magnets, twenty quadrupole magnets and twelve sextupole magnets for keeping the ion beam on a closed orbit of 55.4m circumference. Four magnetic septa and an electrostatic septum are used for injection and extraction of the ion beam from the ring. With the application of the multi-turn injection technique [61] the number of stored ions N_{ion} ranges from $\approx 10^5 - 10^8$ per multi-turn injection corresponding to an ion current $I_{ion} \approx 0.01 - 10\mu$A [62] for a typical ion velocity $v_{ion} \approx 3\%$ of the speed of light, according to the relation

$$I_{ion} = \frac{N_{ion} q_{ion} v_{ion}}{L} , \tag{4.2}$$

where L is the ring circumference and q_{ion} is the ion charge. The maximum magnetic field of the dipole magnets restricts the beam energy. An ion with mass m_{ion} moves in the magnetic field B of the dipole on a circular orbit with a radius ρ due to the Lorentz force. The so called rigidity $B\rho$ of the TSR is therefore defined as

$$B\rho = \frac{m_{ion} v_{ion}}{q_{ion}} . \tag{4.3}$$

The radius of curvature in the dipole magnet is $\rho = 1.15$m and the maximum rigidity of the TSR totals to $(B\rho)_{max} = 1.4$Tm. This allows the storage of ions with an energy of $30\frac{\text{MeV}}{\text{nucleon}}$ assuming a typical mass to charge ratio of 1:2.

4.1.3 The electron cooler

To provide a cooling device for the stored ion beam the TSR features an electron cooler, as can be seen in the enlarged part in Fig. 4.3. A detailed description of the electron

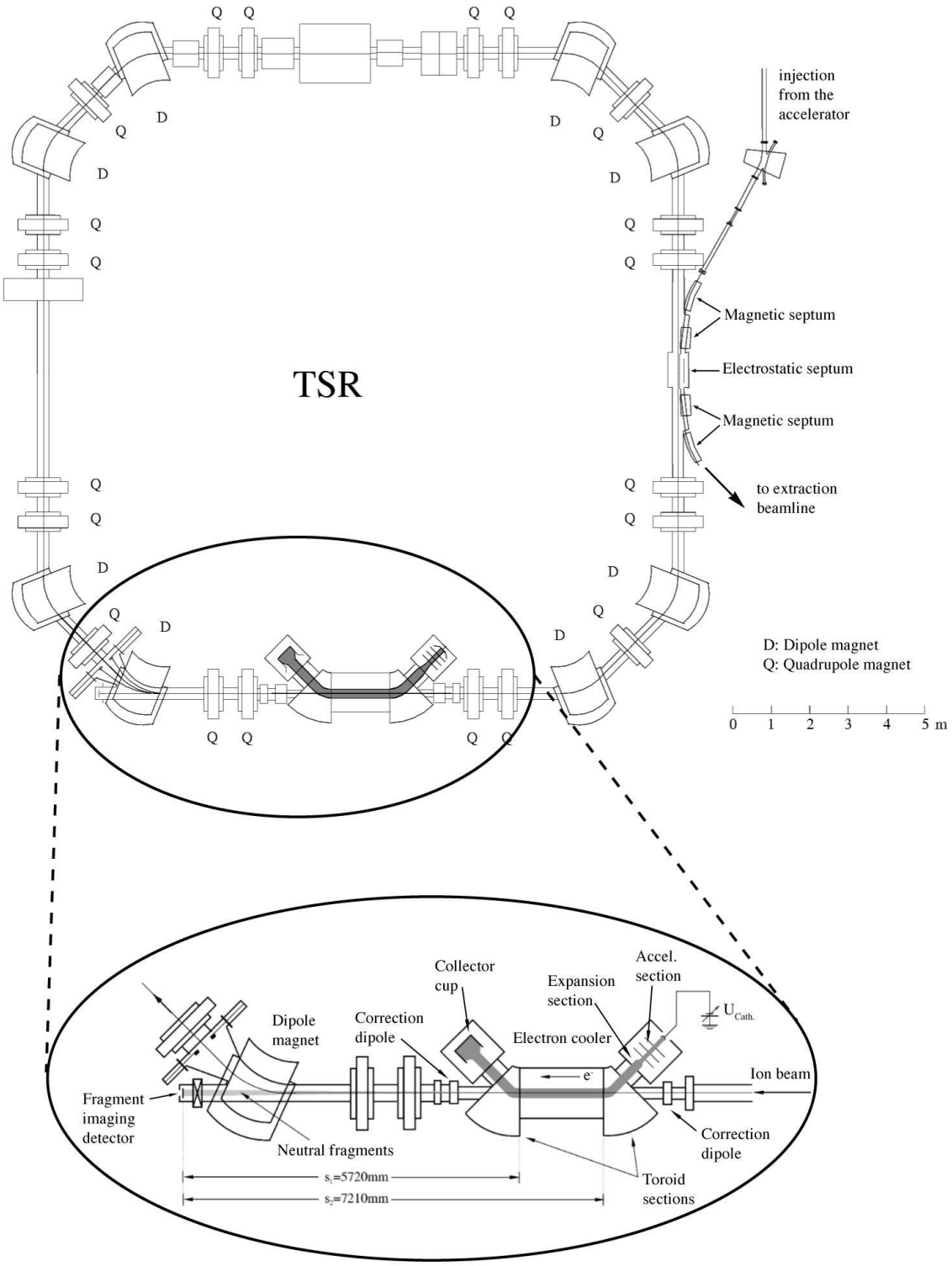

Figure 4.3: *The heavy ion storage ring TSR together with the injection beam line, the electron cooler and the dipole chamber with installed fragment imaging detector is shown.*

cooler was given by Steck *et al.* in 1990 [63]. The electron cooler provides a cold electron beam that is overlapped with the circulating ion beam. After modifications of the electron gun [64] the electron beam is produced by a thermocathode with a diameter of $^3/_8''$. The emission of electrons from the cathode is space-charge limited and the electron current I_e is given by Langmuir's law

$$I_e = PU_{Cath.}^{3/2} , \tag{4.4}$$

where $U_{Cath.}$ is the cathode voltage and P the preveance, which is defined by the geometry of the cathode. Typically, electron currents of 10–30mA are delivered by the thermocathode. The electrons are accelerated in the acceleration section to match the velocities of the ions in the ring. The electron beam is then merged with the circulating ion beam in the toroid section. The interaction section, where electron beam and ion beam overlap, has a length of about 1.5m. In the overlap section the electron beam is guided by a solenoidal field which usually amounts to ≈ 2–4mT. In the second toroid section the electron beam is withdrawn from the overlap section and afterwards collected in a collector cup. To compensate for the distraction of the circulating ion beam imposed by the toroid magnets, correction dipoles are installed just before and after the overlap section ensuring further storage of the ions inside the TSR.

The electron cooler serves two purposes. First, it provides cooling of the stored ion beam. Due to the electron-ion interaction the electron beam provides a 'cold bath' for the ions in the overlap region. This leads to a phase-space cooling, i.e. a reduction of the transverse and longitudinal momentum spread, of the stored ions. The phase-space cooling reduces the width of the horizontal and vertical beam profile, producing a cooled ion beam with a diameter of about 1mm (FWHM) on a timescale of a few seconds (see also [65, 59]). Besides the phase space cooling of the ion beam, the overlapping electron beam also gives rise to dissociative recombination reactions (DR) of the stored ions with the electrons. Thus, the electron beam can also be used as a target with well known collision energy of the fragments, since one has good control of the electron energy, leading to a center of mass (c.m.) energy of electrons and ions of ≈ 10meV.

For both efficient cooling and low-resolution recombination experiments, a cold electron beam is needed. The electrons are produced by the thermocathode with an initial temperature of about $T_i \approx 1400$K. Due to the acceleration of electrons in the section situated after the cathode the longitudinal temperature of the electron beam can be reduced to $T_\parallel \approx 1.2$K. To reduce the transverse temperature of the electrons the electron beam is adiabatically expanded in the straight section after the acceleration and before the toroids.

For this purpose the electrons are produced under an intense longitudinal magnetic field and then transferred to a region with low magnetic field. Thus, a typical beam diameter of 50mm is obtained. The transverse electron temperature after adiabatic expansion is given by

$$T_\perp = \frac{B}{B_i} T_{\perp,i} \ , \tag{4.5}$$

where B_i and B denote the magnetic fields prior to and after the expansion. The ratio $\alpha = \frac{B}{B_i}$ is called the *expansion factor*. It can be adjusted between 1–30 by varying B. The lowest possible transverse temperature that can be attained therefore is $T_\perp \approx 50K$.

4.2 DR fragment imaging

4.2.1 The imaging detector

To extract information on the kinetic energy release of the H_3^+ ions in reaction with electrons at zero relative energy, we measured the distance of the dissociating neutral fragments after a free flight path of several meters (see Fig. 4.3). The molecular ion dissociates in the cooler due to one of the reactions illustrated in Eq. 4.1. The energy comprised in the molecule will then be transferred to the dissociation fragments, either in internal excitation (molecular fragments) or kinetic energy. Thus, the fragments will expand and they will leave the ring at the next dipole magnet, since they are not influenced by the magnetic field. Therefore a fragment imaging [66] detector was installed after the dipole magnet succeeding the electron cooler as illustrated in Fig. 4.3 and in Fig. 4.4. The main part of the detector is a microchannel plate (MCP) with a diameter of 80mm and a phosphor screen situated just behind it. The image of the phosphor screen is monitored by a photomultiplier (PMT) and is digitized using a 1kHz charge-coupled-device (CCD) camera. The CCD chip offers a resolution of 260×260 pixels and is coupled to a frame grabber device. Due to restrictions in space and due to the nature of the CCD camera, the image of the phosphor screen was transferred to the camera via a mirror and the image was enhanced by means of an image intensifier.
A particle hitting the MCP produces a light spot on the phosphor screen. The light spot is detected by the PMT. The photomultplier triggers the switching off of the phosphor screen and the readout of the camera frame. After the frame has been recorded the phosphor screen is then turned on again. The maximum difference in arrival times of particles belonging to one DR event is several ns, while the response time of the phosphor screen is about 5μs. Hence, this trigger mode operation suppresses random coincidences

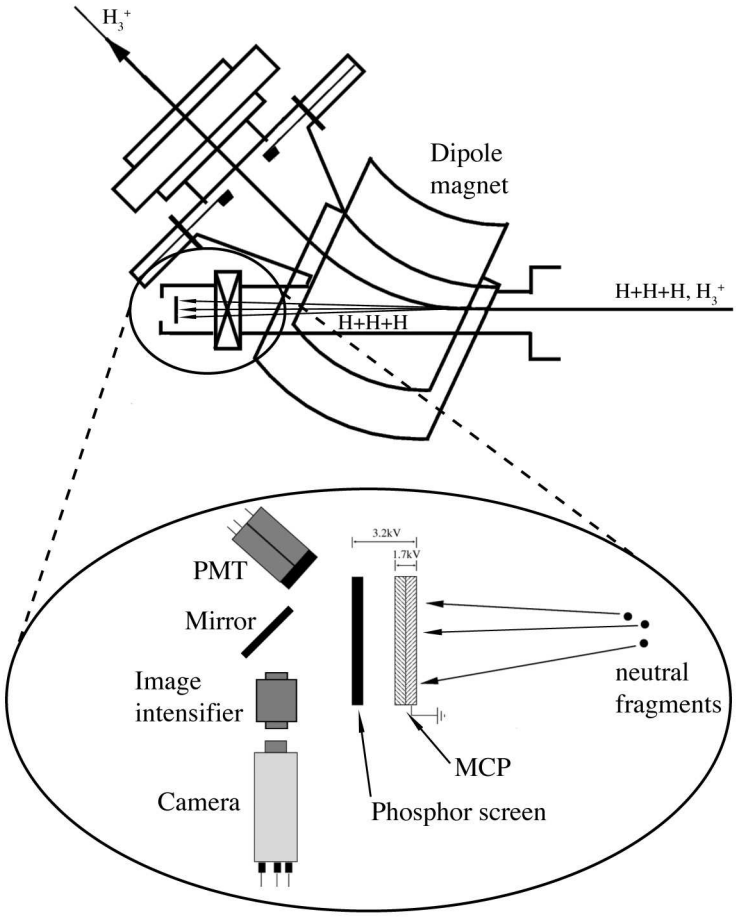

Figure 4.4: *Schematic drawing of the dipole chamber with installed fragment imaging detector.*

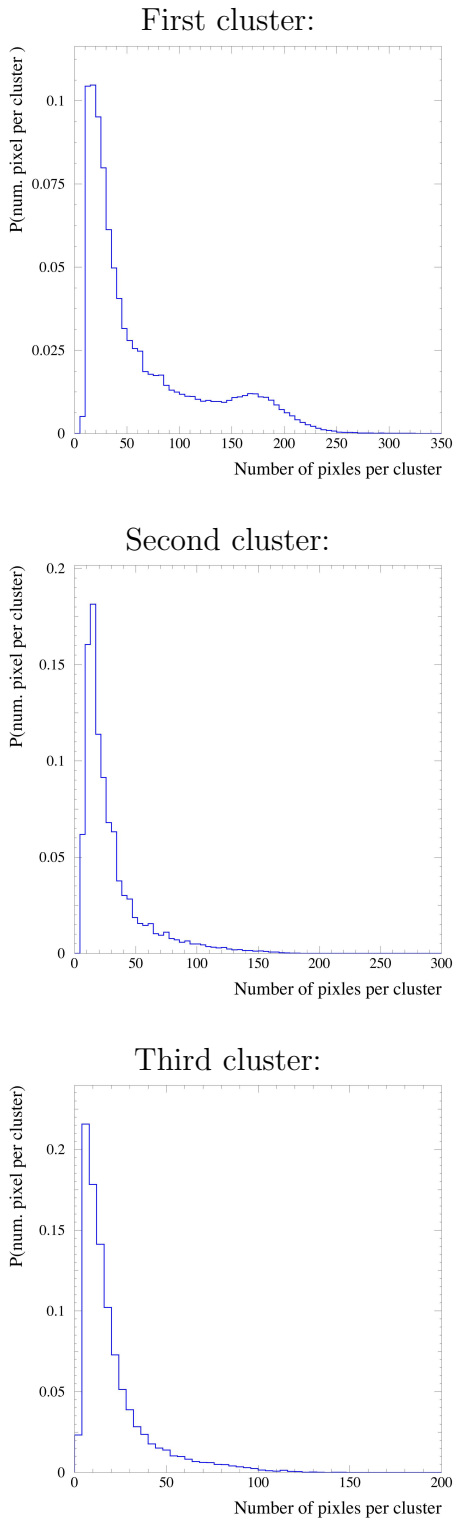

Figure 4.5: *Distribution of the number of camera pixels recorded per cluster detected by the data acquisition, for the first particle (left), the second detected particle (middle) and the third MCP hit (right).*

between hits due to unrelated fragments if the rate of incoming neutral fragments is kept low, usually below 1kHz.
On analysis, the positions of the light spots were determined, using a peak finding procedure. One particle event, i.e. light spot, usually covers several pixels on the CCD. A distribution of the amounts of pixels included in these clusters is shown in Fig 4.5. The number attached to the clusters is determined by their brightness, i.e. the brightest cluster gets assigned the number 1, the second brightest the number 2 and so on. The peak finding routine determines the center of each cluster by weighting each pixel inside the cluster with its amplitude. Hence, the center of the cluster is calculated with the following formula:

$$x_c = \frac{\sum_i x_i \mathrm{A}_i}{\sum_i \mathrm{A}_i} \ , \tag{4.6}$$

where x_i is the x position of the pixel and A_i denotes its associated amplitude. The same holds true for the y coordinate of the cluster center. For the cluster center of each cluster the relative projected distance between any two fragments on the plane of the detector can be deduced. To take into account the dimension of a cluster, two cluster must have a minimum distance of $\approx$ 50Pixels to be considered as two seperate clusters. All events where this condition is not fulfilled are discarded in the data analysis. Naturally, the cluster position is at first only known in pixels. Therefore, the CCD has to be calibrated in order to obtain the pixel-to-millimeter calibration factor. This pixel-to-millimeter calibration was at first done by visual judgement but turned out to be unreliable. Thus a numerical approach was sought. With this method the calibration factors were determined for both beam times in January 2003 and April 2003. The obtained results were $32.79 \pm 0.12 \frac{\mathrm{Pixel}}{\mathrm{mm}}$ for January and $34.96 \pm 0.28 \frac{\mathrm{Pixel}}{\mathrm{mm}}$ for the April beam time, respectively. A detailed description of the newly developed procedure can be found in Appendix A.

4.2.2 Multiplicity distribution

In Fig. 4.6 a characteristic distribution of number of clusters per frame is displayed. Taking into account the branching ratio of the DR reaction (Eq. 4.1) of three-body to two-body, being about 3:1 at zero relative energy, it is not evident why the amount of single events observed is so significant. Thus, one needs to consider that there are other reactions contributing to one particle events. To verify our event distribution shown in Fig. 4.6, we conducted a calculation of the probabilities P(N) for an event with N clusters to occur. As additional background processes we took into account the dissociative excitation (DE)

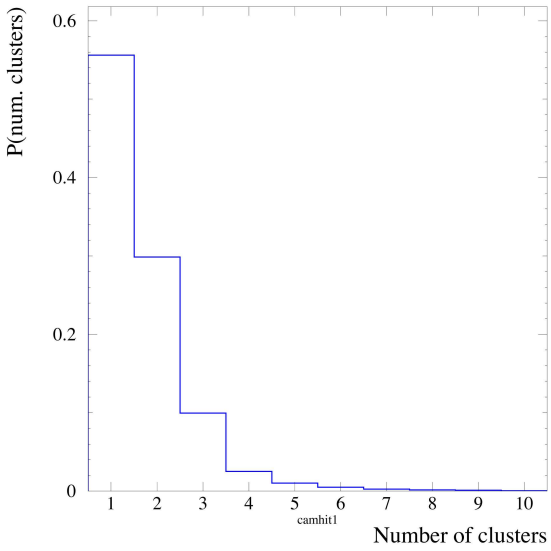

Figure 4.6: *Typical distribution of number of clusters per frame.*

and residual gas induced processes, where a collision with a residual gas molecule X leads to the breakup of H_3^+ (REST).

$$REST: \quad H_3^+ + X \longrightarrow \begin{cases} H + H_2^+ + X \\ H^+ + H_2 + X \end{cases} \tag{4.7}$$

$$DE: \quad H_3^+ + e^- \longrightarrow \begin{cases} H + H + H^+ + e^- \\ H_2 + H^+ + e^- \\ H_2^+ + H + e^- \end{cases} \tag{4.8}$$

The charged fragments produced in these reactions will get lost inside the dipole magnet, but the neutral fragments will leave the ring and will be recorded on the imaging detector. Thus, the residual gas processes will yield only single events and the DE will yield single and double events. If we assume that 40% of the events result from background and the remaining DR events undergo the above mentioned branching ratio. We can then obtain an estimate of the rate at the detector during the measurement. Furthermore, in the calculations we assumed a detector efficiency of 60% and a switching time of the phosphor screen of 5μs, resulting in a value for the probabilities P(N). Only the probabilities for N ranging from 1–4 were calculated. For a rate of neutral particles of 1kHz we arrived at P(1) $\approx$ 60%, P(2) $\approx$ 31%, P(3) $\approx$ 10% and P(4) $\approx$ 0.1%. The single, double and triple events already show a good agreement, but the probability for four clusters still

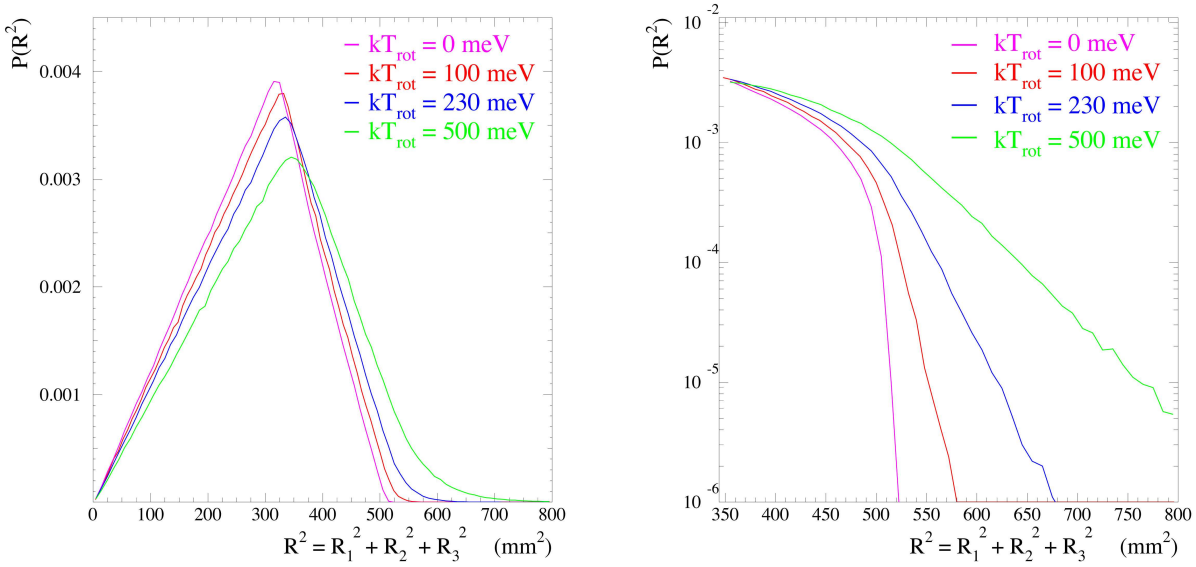

Figure 4.7: *Monte Carlo simulations of the R^2 distribution for H_3^+ , with different rotational excitation simulated with 10^6 events each. On the* **left** *side the complete distribution plotted over all R^2 values is shown, while on the* **right** *side only the regime with $R^2 > 350\text{mm}^2$ is plotted with a logarithmic scaling on the y-axis to illustrate the differences between the various rotational temperatures.*

differs from the distribution in Fig. 4.6. For a higher rate of neutral particles of 20kHz we obtained P(1) ≈ 58%, P(2) ≈ 33%, P(3) ≈ 13% and P(4) ≈ 2%. This shows an overall good agreement with the measured distribution even for the four cluster events. The results suggest that the average neutral rate on the detector for this measurement was around 20kHz.

4.2.3 Monte Carlo simulations

The KER is related to the sum of the squared velocities of the fragments in the center of mass frame of the molecule, and therefore to their squared distances at the detector position. However, as the detector only records 2-dimensional transversal distances of the fragments, and moreover, the position of each recombination event inside the interaction event of 1.5m is unknown, even a fixed KER leads to a broad distribution of the sum of squared transversal distances $R^2 = R_1^2 + R_2^2 + R_3^2$. Nevertheless, to gain a qualitative estimate of the rotatinal temperature of the H_3^+ ions produced in the hollow cathode source a Monte-Carlo simulation can be performed.

The simulation applied to simulate the R^2 distribution of rotationally excited H_3^+ assumes a Boltzmann distribution for the rotational levels and their probabilities for a given tem-

perature. Furthermore, the orientation of dissociation planes of the molecules is assumed to be isotropic with random DR event position in the cooler. Moreover, no correlation in the fragmentation geometry is assumed. For one million simulated particles containing different rotational temperatures, this leads to R^2 distributions as illustrated in Fig. 4.7. Higher rotational excitation contained in the H_3^+ ions leads to an overall broadening of the spectrum and the distribution peaks at higher R^2 values. The rising and falling slopes of the distribution are steeper for lower rotational temperatures. The differences in the falling slopes is illustrated in the right hand picture. There the distribution is plotted for $R^2 > 350\text{mm}^2$ with a logarithmic scaling on the y-axis. In this tail section of the distribution, the different rotational excitation of the ions can be clearly distinguished. The simulated R^2 distribution for $k\text{T}_{rot} = 0\text{meV}$ has a clear cut-off at around $R^2 = 520\text{mm}^2$. The slope of the other curves differ significantly and are less steep. The simulations containing higher rotational energies are always located above the curves simulated with less rotational excitation. Thus, by comparing the tail of the simulated distributions to the measured kinetic energy release spectra one can obtain a qualitative estimate for the rotational temperature of the H_3^+ ions.
In the simulation some effects are not considered. First, it was observed [67] that the H_3^+ molecules show a small preference to dissociate into a linear geometry in the three body channel. This will result in a change in the R^2 distribution due to the fact that only a 2-dimensional projection of the neutral fragments is recorded by the imaging detector. Because of this part of the kinetic energy released upon dissociation can be hidden. An additional effect which is not taken into account in the simulations results from the toroid sections, where the ion and electron beam are merged. Inside the cooler the ion velocity $\mathbf{v}_{ion}$ and electron velocity $\mathbf{v}_e$ are parallel and their absolute values are very close to each other. Thus, the relative velocity is $\mathbf{v}_{rel} = \mathbf{v}_{ion} - \mathbf{v}_e \approx 0$ resulting in the relative energy $\text{E}_{rel} \propto \mathbf{v}_{rel}^2 \approx 0$. But in the merging sections the velocity vectors are not parallel but enclose an angel θ. Therefore, the absolute value of the relative velocity is $|\mathbf{v}_{rel}| = \mathbf{v}_{ion}^2 + \mathbf{v}_e^2 + 2|\mathbf{v}_{ion}||\mathbf{v}_e|\cos\theta > 0$. Hence, the relative energy is no longer zero resulting in a higher kinetic energy release leading to a shift to higher R^2 values for some events.

4.3 Results

4.3.1 Data analysis

To determine the internal rotational temperature of the H_3^+ ions produced in the hollow cathode source, two beam times at the TSR in Heidelberg where undertaken in January

and April 2003. In both beam times the three body channel of the dissociative recombination of H_3^+ was utilized as the probing reaction. As a direct comparison the rotational temperature of H_3^+ ions produced in the CHORDIS source was obtained during each beam time. The applied beam energy differed between the two beam times. In January the full HSI (see Sec. 4.1.1) energy was used, totaling to 5.1MeV, while in April only 1.5MeV was applied. The differences in beam energy leads to a different R^2 distribution. With the high beam energy the expansion cone of the neutral dissociation fragments is smaller, thus the spectrum is shifted to smaller R^2 values. Since the CCD is limited in resolution, a large expansion cone, i.e. small beam energy, should be favored. The distributions taken at different beam energies cannot be compared directly, but by multiplying the R^2 values with the ratio of the beam energies one can correlate the two spectra.

Analysis focused on the three body events, i.e three clusters in one frame. In order to assure that most analyzed events result from only one DR event, an elliptical center of mass cut was applied to the data as illustrated in Fig. 4.8 and Fig. 4.9. The beam is cooled by the electron cooler and the beam diameter is reduced to $\approx$ 1mm (see Sec. 4.1.3). Thus, the center of mass of the neutral fragments on the detector resulting from one DR event inside the cooler region should also be localized close to the center of mass of the beam. This only applies if one allows for sufficient cooling time, hence 2s of pre cooling was always taken into account. To determine the center of mass of the beam on the detector, all recorded three body events are projected onto the x-axis and onto the y-axis, respectively. These obtained beam profiles in x- and y-direction were fitted with a Gaussian distribution and the center of the beam on the detector was determined. Every three-cluster event was then compared to the beam center and discarded if the distance of the center of mass of that particular event was larger than 1.5σ in x- and y-direction, respectively. The σ of a Gaussian distribution is defined as the distance between the inflection points of the curve and its mean value. σ is connected to the full width at half maximum (FWHM) of the distribution with $\sigma = \frac{(\mathrm{FWHM})}{2.35}$. In this way it is ensured that most events detected really result from one DR event because three-body events resulting from other sources, for instance two different events in one camera frame, do not have the appropriate center of mass. The factor 1.5 was taken because it turned out to produce sufficiently good results while still having high enough statistics. However, as one can see in Fig. 4.8 and in Fig. 4.9 there is still a significant background contribution passing the center of mass cut, approximated by the pink dotted line.

It is important to point out that the R^2 distribution of the background will differ from that of the real three-body events. In order to understand the influence that the background events passing through the c.m. cut have on the data, the events outside the c.m. cut

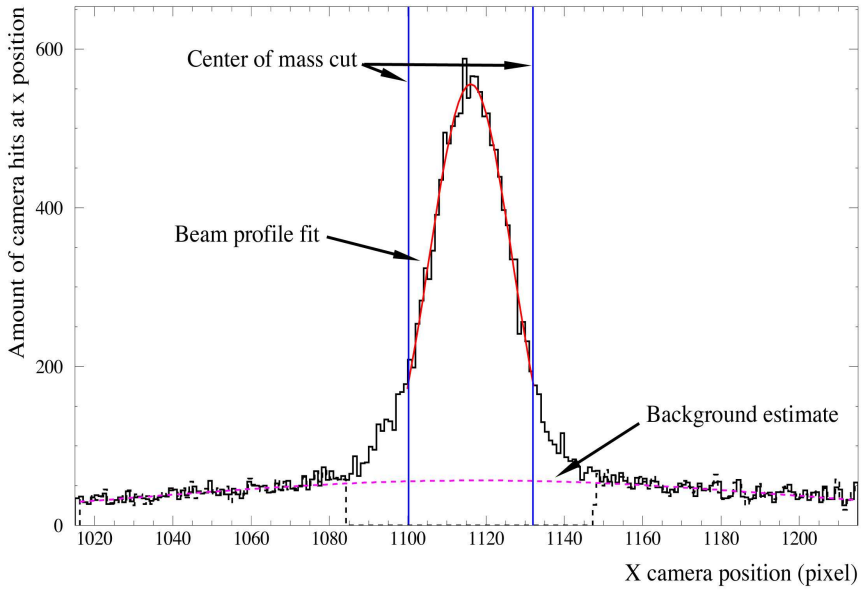

Figure 4.8: *A typical beam profile in x-direction. Shown is the performed center of mass cut (blue lines), the fit for the beam profile (red line) and the background estimate (pink line).*

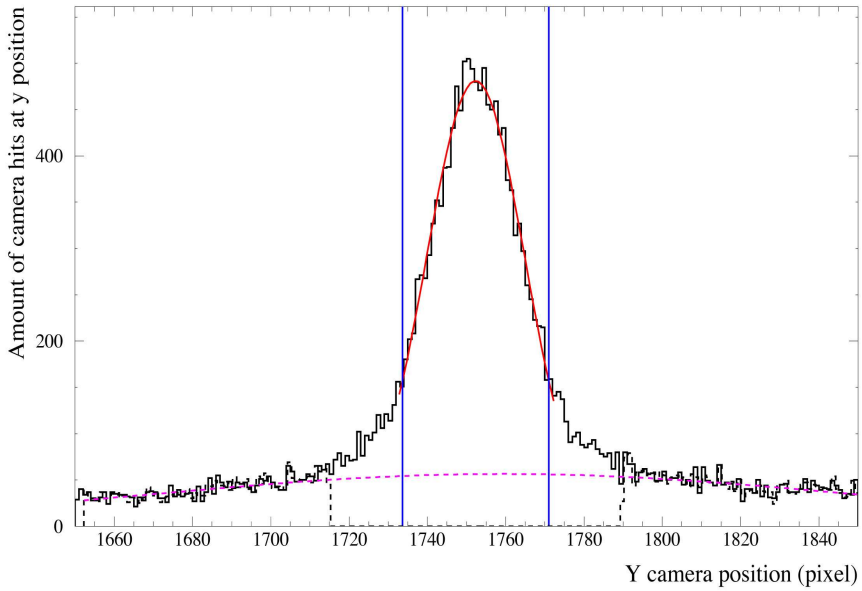

Figure 4.9: *Same as Fig. 4.8 shown for the y-direction.*

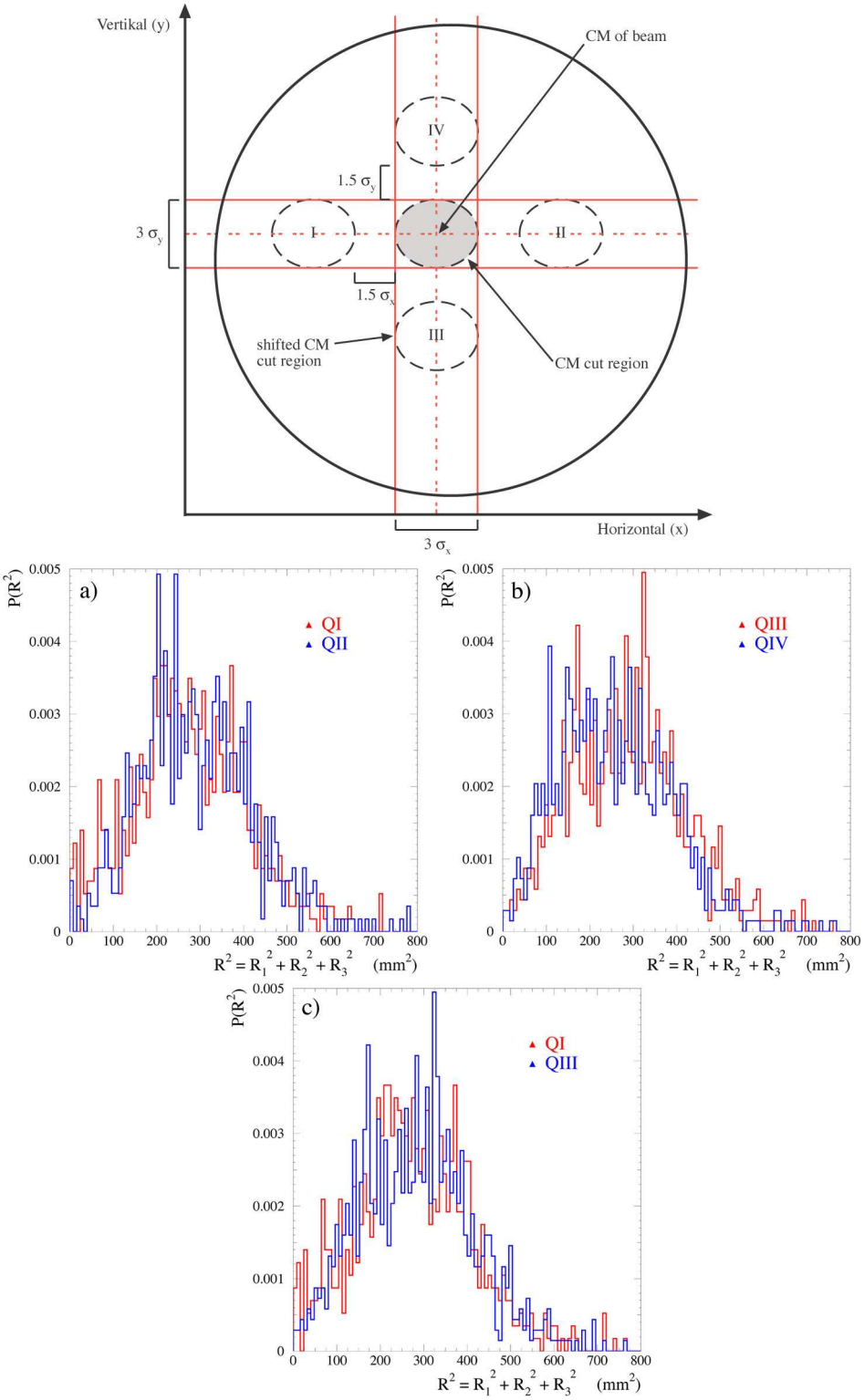

Figure 4.10: *A schematic drawing of the detector with c.m. regions is displayed (dimensions are exaggerated!). The inlay figures show the distributions obtained from the events included in the shifted c.m. regions,* **a)** *c.m. shift in x-direction (QI and QII);* **b)** *c.m. shift in y-direction (QIII and QIV);* **c** *a comparison between the two different shifts (QI vs. QIII).*

were also analyzed. To get a reliable background estimate from events outside the c.m. cut region, one needs to apply the same criteria that the real background events undergo, i.e. they also need to pass a 1.5σ center of mass cut. Therefore the c.m. cut region was shifted away from the beam center as illustrated in Fig. 4.10. The data was taken from one exemplary setting with good statistics (namely the HOCIS-1 run). The shift had to meet the following conditions, one needs to minimize the influence of genuine three particle events by shifting far away from the beam center, while still obtaining a sufficient number of event counts. Thus an overall shift of 4.5σ was applied. In order to rule out a dependence of the background on the shift direction, the shift was executed in all four directions. The background distributions obtained from these shifts are on display in the lower part of Fig. 4.10. Despite the rather poor statistic, the background spectra were found to agree independently of the shift direction, i.e. they all peak at approximately the same position and the slopes on either side of the distributions were found to be the same. Hence, for the analysis, the background distributions from all four quadrants were added up.

Naturally, the background influence only accounts for a small amount of events actually passing through the c.m. cut. This significance was calculated by comparing the total events contained in the center of mass cut, indicated by the area under the red curve in Fig. 4.8, to the amount of background events (pink curve) inside the cut region. The average ratio obtained from these estimates was 17 ± 1.3 %. The background characteristic obtained from the R^2 distribution outside the center of mass cut is then weighted with this ratio, illustrated in Fig. 4.11 by the blue curve. The background is then removed from the original data (red curve) resulting in the green curve, which was again normalized. Comparing the green and the red curve, one can state that the background contamination alters the overall spectrum by reducing the broadening. In the tail region, due to the higher portion of large R^2 values present in the background, almost all the events above $R^2 > 530\text{mm}^2$ result from background. Also the shape of the background corrected curve changes slightly and is being shifted a little inwards in the region of $R^2 > 450\text{mm}^2$, now running below the original data.

4.3.2 January beam time

The results of the January beam time are summarized in Fig. 4.12 and Fig. 4.13. Due to other experiments, the DR imaging part of the beam time only covered about 3 days of data taking. Thus, the source conditions could only be investigated for a short period of time. All runs were done with the type A wiring with positive and negative volt-

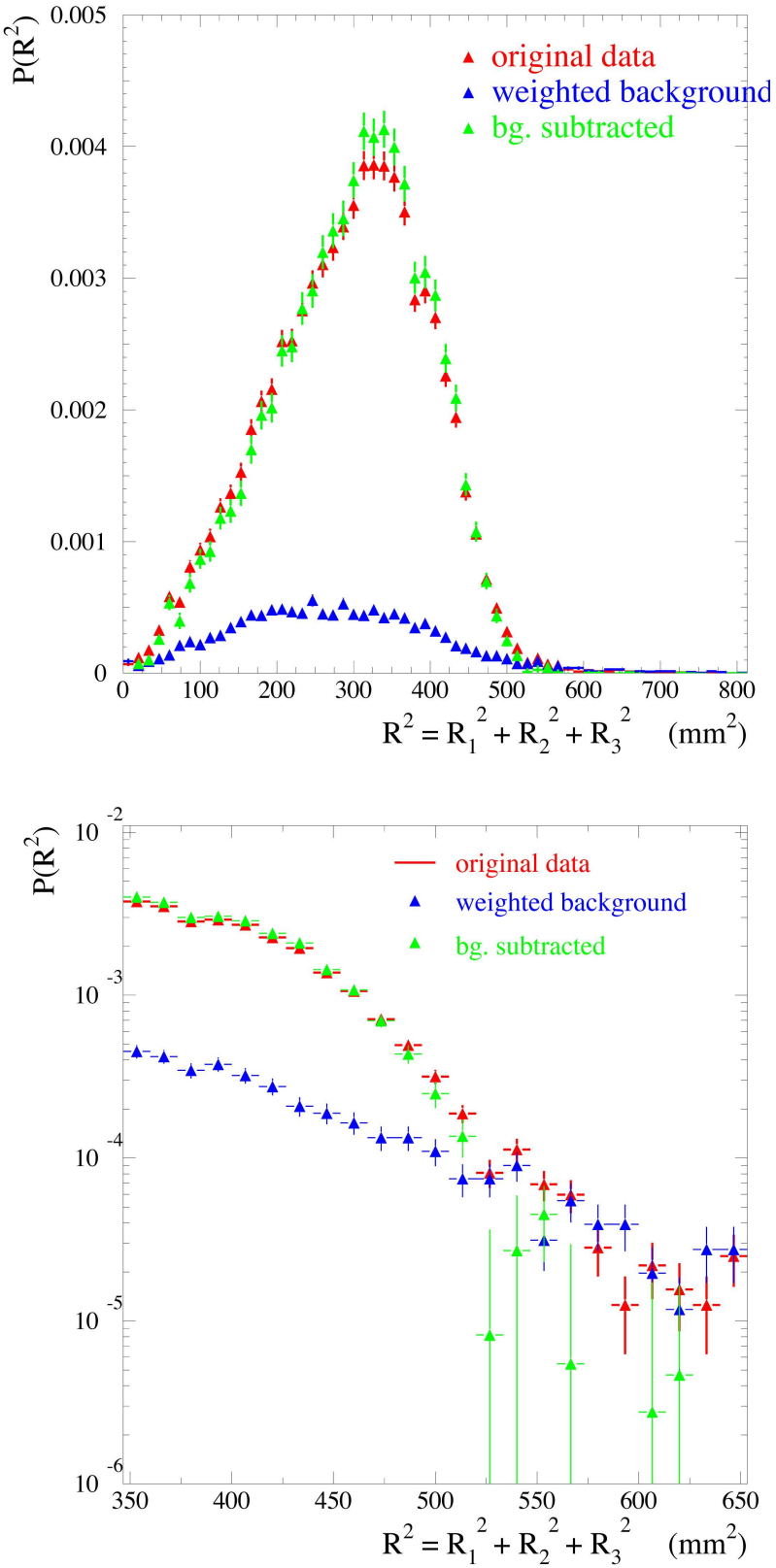

Figure 4.11: *Normalized R^2 distribution of the events outside the center of mass cut weighted with their ratio of contribution to the c.m. cut region (blue). Original data (red) and with removed background and renormalized (green).*

ages applied to the bias electrode. The settings were always directly compared to the CHORDIS results obtained at the same beam energy. At all measurements we stored the beam for 3s to allow for sufficient phase space cooling and the vibrational excitation in the molecules to cool down to the ground state. Data was then taken for 12s for the low energy measurements, and for 15s for the high energy, before the next injection into the storage ring took place. This way vibrational excitation influencing our measurements can be neglected and the eventual influence that the electron cooler has on vibrational excitation of the stored ion beam is for every source condition the same.

The two figures (Fig. 4.12 and 4.13) presented are exemplary results obtained for two different source conditions. Fig. 4.12 displays a run taken with a fairly high negative bias setting of $U_{BPS} = -87V$, while the other source settings were the following $U_{APS} = 1.9$kV, $I_{APS} = 46$mA, p = 3torr. One can see that both R^2 distributions agree quite well, only in the tail figure on the right hand side the hollow cathode source data is running a little below the data from the CHORDIS. Note that no background correction was done for these two runs due to the bad statistic and since two data sets are compared, that are both contaminated by background in a similar fashion, that should not pose a problem. In Fig. 4.13 a measurement with a reversed polarity ($U_{BPS} = +39V$) of the bias electrode is shown, with the other source settings being: $U_{APS} = 2.2$kV, $I_{APS} = 58.2$mA, p = 3.2torr. If one compares the two presented curves (both are background corrected) one can observe, that in the complete R^2 spectrum the maximum of the hollow cathode distribution is shifted to lower values and peaks slightly higher. At the same time, the falling slope runs below the reference data, which becomes even more apparent in the tail plotted in the right hand picture. Important to note here is the difference, that results form the fact that this last spectrum were taken at an increased beam energy of about 5.1MeV, which narrows the expansion cone, as mentioned earlier, and therefore the R^2 distribution is situated at lower values.

In comparison to the CHORDIS source we find that a bias voltage of negative polarity yields almost no difference to the CHORDIS data. We conclude, that at a situation where the ions are extracted from the production region (see also Sec. 3.2) the H_3^+ ions produced do not have a lower rotational excitation than ions produced in the CHORDIS. The small differences visible in the logarithmic plot of the high R^2 spectrum can be explained by the fact, that we are looking at two different ion sources, which both differ in their way of producing ions to a large extent. So naturally, the rotational excitation will show small differences. When we then move to a setting with a low positive potential on the bias electrode the obtained spectrum changes, while the other source settings remain more or less constant. It is visible in the tail of the distribution, that the hollow cathode data

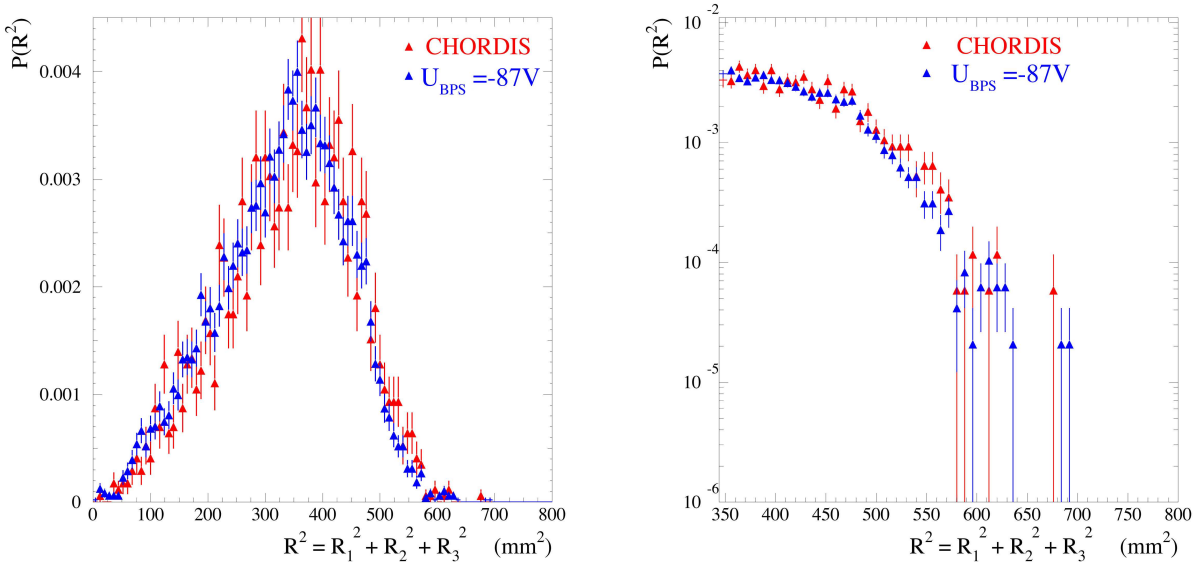

Figure 4.12: *Comparison of CHORDIS to hollow cathode source for wiring type* **A** *(January 2003) with a negative voltage applied to the bias electrode. Note no background correction was done due to the bad statistic. Source settings were:* $U_{APS} = 1.9\text{kV}$, $I_P = 46\text{mA}$, $U_{BPS} = -87\text{V}$, $p = 3\text{torr}$.

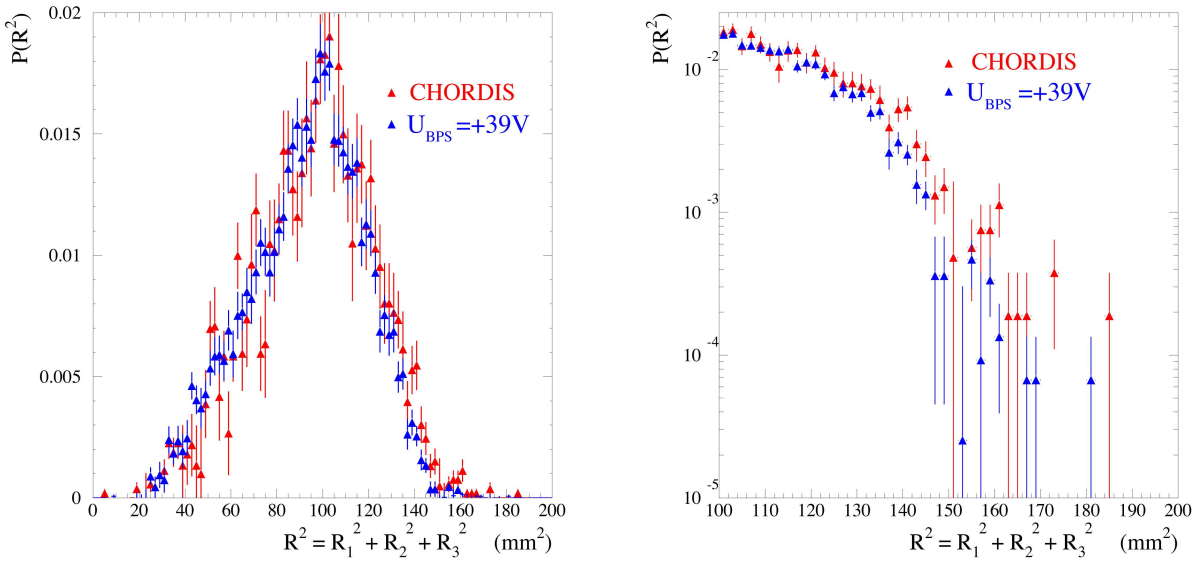

Figure 4.13: *Comparison of CHORDIS to hollow cathode source for wiring type* **A** *(January 2003) with a positive voltage applied to the bias electrode. Note due to higher energy (5.1MeV) the* R^2 *spectrum is situated at lower values. Source settings were:* $U_{APS} = 2.22\text{kV}$, $I_P = 58.2\text{mA}$, $U_{BPS} = +39\text{V}$, $p = 3.2\text{torr}$.

is below the reference data, i.e. the H_3^+ ions are less rotationally excited. However, this decrease in rotational excitation of the ions could only be verified for one particular source setting with only one bias setting. Hence, it could not be ruled out that other factors, for instance the pressure, also play a significant role. So another beam time was scheduled in April 2003 to further investigate the behavior of the ion source.

4.3.3 April beam time

In the beam time conducted in April 2003, several changes had been made to the ion source. This time the type B wiring was applied (see Sec. 3.5) and almost a whole week of DR imaging was used for thorough source testing. Only humble alterations to the actual measurement procedure were done, compared to the previous beam time. The beam was accelerated only to full RFQ energy, being about 1.4MeV, so no other resonators were used. The time intervals of data taking were shortened to a 9s duty cycle, allowing the beam to circulate in the ring for 2s to provide sufficient phase space cooling and time for the vibrational states to cool down to the ground state, before starting the actual measurement for 7s. Electron cooling was applied during the whole measurement cycle. Unfortunately, we experienced difficulties with our pressure measurement, thus we had to rely on the next available penning gauge IS (see Fig. 3.13) which is situated a little further downstream from the ion source. Estimates for the outside H_2 pressure p were then derived by comparing these readings to formerly obtained sets of outside pressure and IS pressure values. Hence, the given values for the outside pressure are only estimates and will always be accompanied by the respective readings on penning IS.

The primary objective was at first to reproduce a similar result as observed in the last beam time with the new way of wiring. The initial run conducted is displayed in Fig. 4.14. Again the hollow cathode data is compared to the CHORDIS data obtained earlier in the same beam time. In the left figure one can see, that the blue curve definitely peaks higher than the red curve and at a different R^2 value. Furthermore, this is supported by the fact that the raising slope is running above the reference data for most of the values, while the falling slope crosses the CHORDIS spectrum at around $R^2 \approx 400\text{mm}^2$ and is then situated clearly below. This becomes even more apparent if one looks at the tail of the spectrum, plotted on a logarithmic scale on the right hand side. Now all data points, lying at higher values than the crossing of the two curves, are running below the reference data.

The next step was to test the dependence of the 'coldness' of the H_3^+ ions on several different source conditions. Therefore, it was decided to take the initial run as the new

benchmark condition, to which all succeeding runs will be compared to. All source settings were numbered sequentially in the chronological order of data taking and will be referred to by their associated number, e.g. making the new reference run HOCIS-1 (**HO**llow **C**athode **I**on **S**ource). A tabular summary of the different settings for all runs can be found in Tab. 4.1. While one parameter was varied we tried to maintain all other settings at their original values. However, since all of the parameters are connected to one another this was not always possible. Nevertheless, source conditions were always matched, so that they reflect the previous settings as good as possible. Furthermore, since the main part of the information can be deduced by looking at the tail region of the R^2 distribution only those will be displayed unless otherwise necessary.

In runs 6 and 7 (Fig. 4.15 left figure) various parameters were changed, as can be seen in Tab. 4.1. Both distributions agree with that of HOCIS-1 indicating that no change in rotational excitation of the ions could be found. In the right hand figure the discharge conditions were changed by increasing the amount of current running through the plasma. The run number 10, which has similar discharge conditions than the reference, although the bias voltage is higher, doesn't show any significant difference. At the same time the HOCIS-8 run, which has undergone a decrease in anode current, while keeping pressure and bias voltage constant, shows an increase in rotational excitation. The blue curve comes in lower than HOCIS-1 at the beginning, then crosses the curve and for R^2 values above 400mm^2 most of the data points are situated higher than the direct comparison.

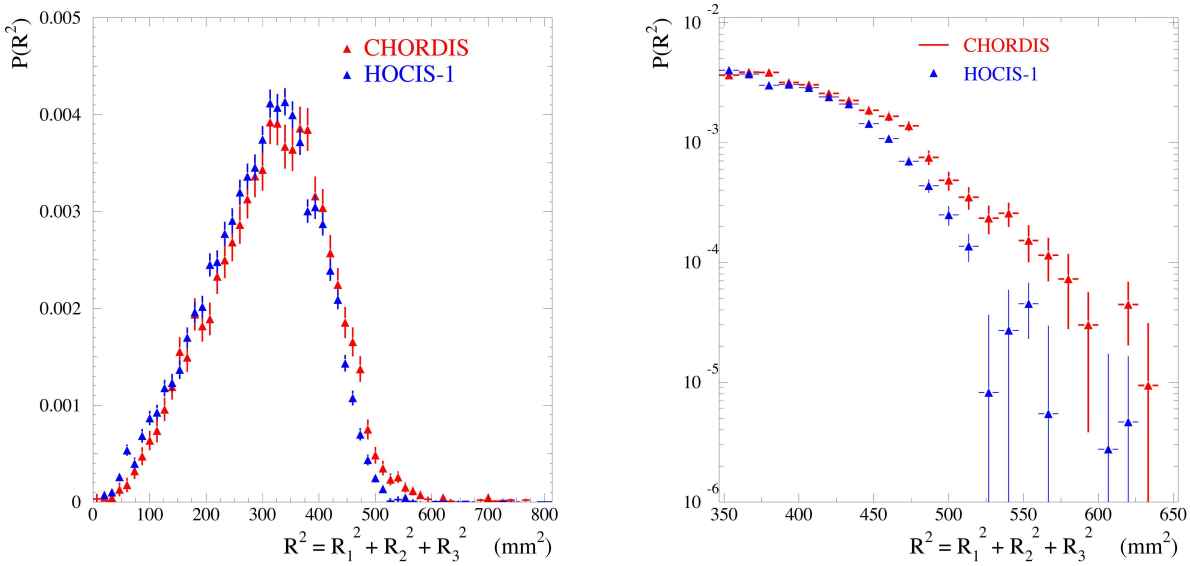

Figure 4.14: *Comparison of CHORDIS to hollow cathode source for wiring type* **B** *(April 2003). Source settings were:* $U_{APS} = 1.43\text{kV}$, $I_{APS} = 45.8\text{mA}$, $U_{BPS} = +308\text{V}$, $p_{IS} = 6 \cdot 10^{-4}\text{mbar}$.

Setting	U_{APS}(V)	I_P(mA)	U_{BPS}(V)	I_{BPS}(mA)	p_{IS}(mbar)	p(mbar)
HOCIS-1	1430	45.8	309	n/a	$6 \cdot 10^{-4}$	78
HOCIS-2	1470	45.8	75	n/a	$6 \cdot 10^{-4}$	78
HOCIS-3	1640	47.6	44	n/a	$6 \cdot 10^{-4}$	78
HOCIS-4	1410	45.8	557	n/a	$6 \cdot 10^{-4}$	78
HOCIS-5	1250	45.7	800	n/a	$6 \cdot 10^{-4}$	78
HOCIS-6	1560	57.6	772	n/a	$2 \cdot 10^{-4}$	26
HOCIS-7	1130	75.7	222	n/a	$1 \cdot 10^{-4}$	13
HOCIS-8	860	54.7	586	n/a	$4 \cdot 10^{-5}$	5
HOCIS-9	930	54.7	284	17.9	$4 \cdot 10^{-5}$	5
HOCIS-10	1050	42.6	593	n/a	$5 \cdot 10^{-5}$	6
HOCIS-11	1240	53.7	270	10	$4 \cdot 10^{-5}$	6
HOCIS-12	1260	55.3	260	8.2	$4 \cdot 10^{-5}$	5
HOCIS-13	1270	55.2	244	1	$4 \cdot 10^{-5}$	5
HOCIS-14	1260	55.3	245	≈ 5	$5 \cdot 10^{-5}$	6
HOCIS-15	1240	55.3	244	5	$5 \cdot 10^{-5}$	6
HOCIS-16	1180	55.1	235	5	$7 \cdot 10^{-5}$	8.5

Table 4.1: *Table of different source settings and their associated values.*

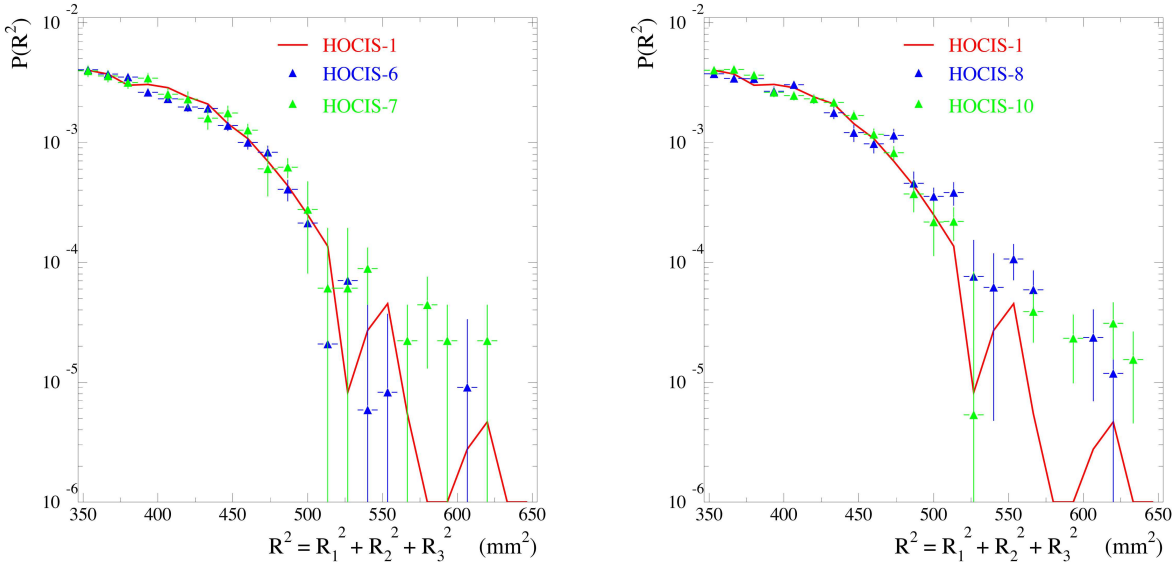

Figure 4.15: *HOCIS-1 compared to runs 6, 7, 8 and 10.*

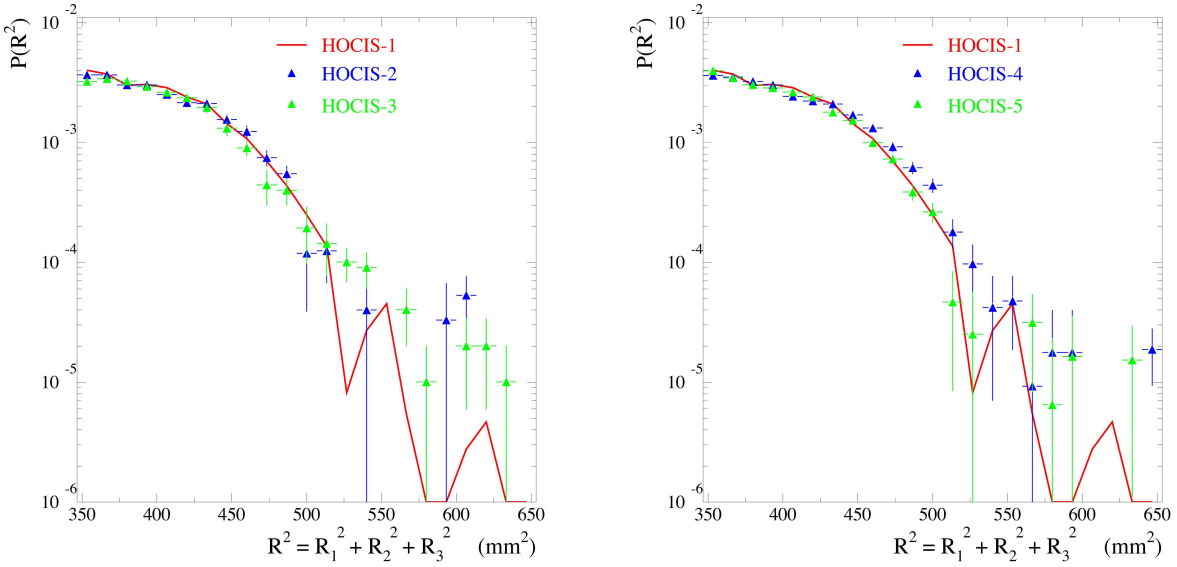

Figure 4.16: *HOCIS-1 run compared to runs 2, 3, 4 and 5 with various bias voltage settings. All other settings remain unchanged.*

The behavior with changed bias voltage was observed in runs 1, 2, 3, 4 and 5 (Fig. 4.16). A wide range of bias potentials was covered with no attention payed to the bias current. On the left side bias settings lower than in the reference are shown. Run number 2 with $U_{BPS} = +75V$ agrees quite well with the first run, while an even lower setting $U_{BPS} = +44V$ yields no significant change to the reference data. The picture changes when the bias voltage is increased above the reference value of $U_{BPS} = +308V$. With a setting of 557V the picture degrades again and the H_3^+ ions are now more rotationally excited while at 800V the data taken agrees quite well again with the run number 1 data. However, the run number 5 showed the highest background contamination of 35% ± 4%, i.e. very high above average of 17% ± 1.3%. Thus, care should be taken with the interpretation.

To further determine the influence played by the bias electrode on the burning plasma and eventually also on the excitation of the H_3^+ ions, we carried out a set of measurements regarding the bias current. We know from the wiring (see Fig. 3.5 and Fig. 3.6), that the current delivered by the bias power supply should be about 5mA at a voltage setting of around 240V. A series of measurements with bias currents around this value were conducted. On the left side in Fig. 4.17 the runs with a higher bias current are displayed. With $I_{BPS} = 8.2$mA we find a good agreement with the reference. The same holds true for a bias setting of 17.9mA. For the $I_{BPS} = 10$mA it can be stated, that within the error bars, it is also found to agree quite well with the data taken from HOCIS-1. The

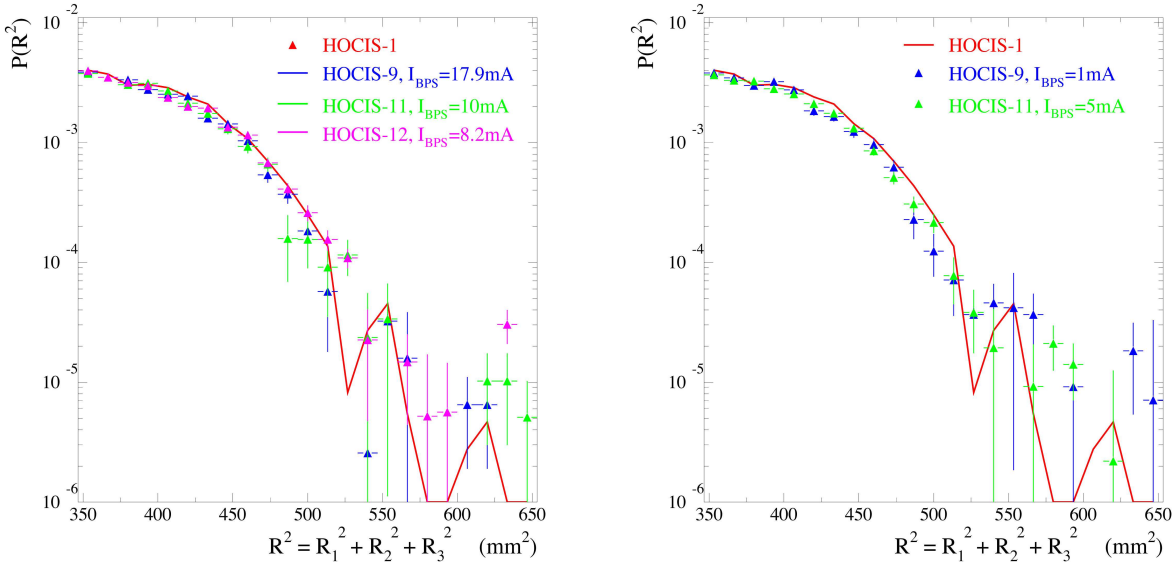

Figure 4.17: *HOCIS-1 run compared to runs 9, 11, 12, 13 and 15 with various bias voltage settings. All other settings remain unchanged.*

lower currents are shown in the right hand picture. Both distributions appear to be less rotationally excited than the reference data. Most data points are situated below the run number 1 distribution. Another attempt for a bias current of 5mA was made in run 14. But it was discovered later, that the current disagreed with this value over a longer period of time. Since we don't store real-time information in our data but only time data, relative to the previous injection, we have no means of filtering out this data, and thus the run has to be discarded.

Concerning the pressure dependence, HOCIS-15 and HOCIS-16 are compared in Fig. 4.18. HOCIS-16 had a pressure increase of 40%, while keeping all other conditions at the same values. Comparing the two curves suggests, that an increase in pressure has at the same time an increasing effect on the rotational excitation of the H_3^+ ions produced. The R^2 spectrum of the run number 16 is clearly above almost all data points of HOCIS-15 and is in much better agreement with the data of HOCIS-1.

To better illustrate the differences between the two HOCIS settings which were found to contain the most and the least rotational excitation, HOCIS-4 and HOCIS-15 have been compiled into Fig. 4.19. As one can see the differences in rotational excitation resulting from changed source conditions are clearly distinguishable.

Summarizing, one can draw the following conclusions from the above elaborated results. Our data suggests that there are several parameters affecting the rotational excitation of the H_3^+ ions obtained from the hollow cathode source. As was expected, the biggest

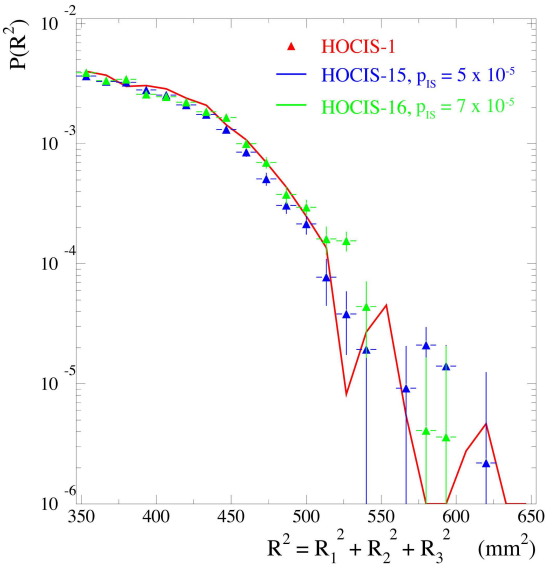

Figure 4.18: *Pressure dependence shown by comparing HOCIS-15 to HOCIS-16.*

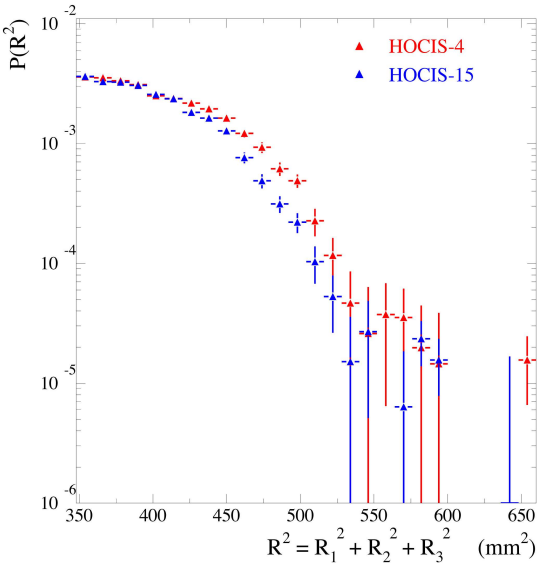

Figure 4.19: *Comparison of HOCIS-4 to HOCIS-15.*

influence is imposed by the voltage settings on the bias electrode. In a regime below ≈ 350V we find the ions to be less rotationally excited than in bias settings above these values. Another effect caused by the bias electrode is the interaction of the electrode with the plasma, which manifests itself in a higher, respectively lower, current delivered by the power supply driving the bias electrode, than the nominal value given by the resistance of the wiring. If it is taken care of, that the bias current stays close to the nominal value of 5mA, we find the situation to improve and the rotational excitation is further reduced. Important parameters, that were also found to affect the rotational temperature of the ions, were the pressure inside the ion source and the discharge conditions given by the anode power supply. If one takes into account that these parameters affect the overall dimension of the plasma this dependence can probably be explained. Higher Pressure and higher anode voltage or anode current make the plasma expand and extend inside the hollow cathode, which will change the distance the ions have to travel before they exit the source, effectively reducing the amount of collisions they undergo.
So the final question will be whether we can give an approximation of the rotational temperature, when comparing the results to the Monte-Carlo simulations? This was undertaken in Fig. 4.20. Here we show the R^2 distributions for the CHORDIS and the hollow cathode source setting number 15 together with simulations for various energies. If we at first look at the data taken for the CHORDIS source we find it to be in pretty good agreement with a rotational temperature of $k\mathrm{T}_{rot} = 230$meV. Looking at the hollow cathode data we can state, that the distribution is situated above the green curve, of the rotationally cold distribution, and clearly below the pink curve. So we can give an upper limit for the rotational excitation of the ions

$$k\mathrm{T}_{rot} \ll 100\mathrm{meV} \tag{4.9}$$

whereas the 0meV curve approximates it much better than the 100meV making it significantly colder than 100meV. This means that the rotational energy contained in the ions produced is at least a factor of 2 better than H_3^+ ions produced in the CHORDIS source. Yet to be explained is the dip like structure in both measured distributions which is not contained in the simulations. Interestingly, it is much more pronounced in the rotationally higher excited CHORDIS data. However, as was mentioned earlier (see Sec. 4.2.3) the simulations are a rather simple approach to the problem and don't take into account any broadening effects, e.g. toroids.

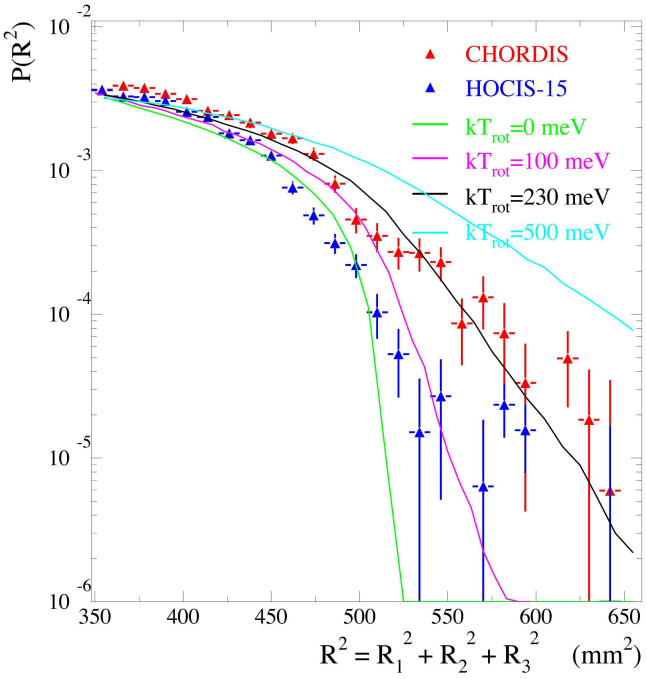

Figure 4.20: *CHORDIS and HOCIS-15 run compared to Monte-Carlo simulations for different rotational excitation of the H_3^+ ions. Both CHORDIS and HOCIS-15 are background corrected.*

5. Summary and outlook

In this diploma thesis the construction and characterization of a hollow cathode ion source has been presented. The aim was the production of rotationally cold H_3^+ ions.
The main parts of the source are an exact copy of an existing source in use by the group of Prof. H. Helm at the Universtät Freiburg. The source consists of a hollow anode and cathode structure with an inner diameter of 1cm. All electrodes are enclosed in a separate volume, leaving only a small opening of 0.4mm. Therefore operation with fairly high inside pressures of 0.2–2.5mbar is possible while keeping the surrounding pressure at 10^{-5}–10^{-4}mbar. The hollow cathode ion source features a liquid nitrogen cooling of both the anode and the cathode. Temperature measurements showed that the outside of the source could be kept close to liquid nitrogen temperature even with high power dissipating discharges.
The plasma characteristics have been determined by means of a current-voltage characteristic. For further characterization of the ion source mass spectra were taken and the ion yields for different source conditions were observed for two different types of electrical wiring. Independent of the wiring, the source was found to deliver a stable maximum current of up to several μA of H_3^+ which was sufficient for all our experiments. The mass spectra showed the production of several different types of ions besides the production of H^+, H_2^+ and H_3^+. Copper ions were found to be present in the discharge resulting from sputtering of cathode material. Additionally, several other ions could be identified caused by restgas present in the source and water. Regarding the ion yields we tested the dependence of the H^+, H_2^+ and H_3^+ current on several source parameters for both wiring types. It turned out that the ratios with which the ions are produced differ strongly on certain source parameters, especially on source inside pressure and bias voltage. And the behavior of the source showed also great differences concerning the two different wiring types.
To investigate the rotational temperature of the ions produced in the hollow cathode ion source, the dissociative recombination of the produced H_3^+ ions with electrons at zero relative energy was studied. As experimental technique heavy ion storage ring particle

imaging was utilized. The rotational temperature of the ions was directly compared to H_3^+ ions produced in a CHORDIS source, which is in regular use at our institute. For the wiring type A, negative bias potentials did not show any significant difference to H_3^+ ions produced in a CHORDIS source, while a positive potential on the bias electrode proved to produce less rotationally excited ions. For the second type of wiring the above result for a positive bias could be verified. Furthermore, we were able to show that the rotational excitation degrades further when special care is taken, that the bias electrode does not influence the plasma.

To get an approximation for the rotational energy contained in the H_3^+ ions produced form the hollow cathode source and the CHORDIS, the results were compared to Monte-Carlo simulations. The H_3^+ ions obtained from the CHORDIS source showed a rotational temperature of $k\mathrm{T}_{rot} \approx 230\mathrm{meV}$. The ions produced in the hollow cathode source turned out to be more than a factor of 2 less rotationally excited and were found to be clearly below the Monte-Carlo simulations for 100meV. Thus we can state that the rotational excitation of the H_3^+ ions produced in the hollow cathode source is $k\mathrm{T}_{rot} \ll 100\mathrm{meV}$.

As indicated in the introduction (see Sec. 1) it was suggested by Kokoouline and coworkers in 2001 [14] that rotational excitation of H_3^+ could explain the vast differences between the values for the rate of the dissociative recombination reaction of H_3^+ with low energy electrons obtained from storage ring measurements and flowing afterglow Langmuir probe measurements. With the less excited H_3^+ ions produced in the hollow cathode source this dependence can now be analyzed. Furthermore, the nature of the cooling of rotational excitation inside the source should be further investigated, since the reason why H_3^+ is rotationally less excited under certain source conditions is not yet fully understood. Due to difficulties with the source in the April beam time the analysis of the results was hampered and did not allow the development of a better understanding of the processes involved in the cooling of the ions. However, recent measurements not included in this diploma thesis showed a much clearer picture and will be published at a later date. Additionally, it might be possible to extent this method of producing rotationally cold molecular ions on to other molecule species.

Appendix

A Detector calibration

The position of the clusters on the phosphor screen is of course at first only available in pixels. In order to obtain the particle distance on the detector in millimeters the CCD has to be calibrated. Therefore a barrier that can be moved in vertical direction is put in front of the imaging detector. The detector is then 'illuminated' by the beam until the structure of the barrier evolves as a 'shadow image'. An example is displayed in Fig. A.1. Several of these runs are taken with the barrier at different positions. The relative position of the obstacle is determined from the outside with a sliding caliper by measuring the length of the motion feedthrough holding the barrier in place. The calibration factor can be deduced

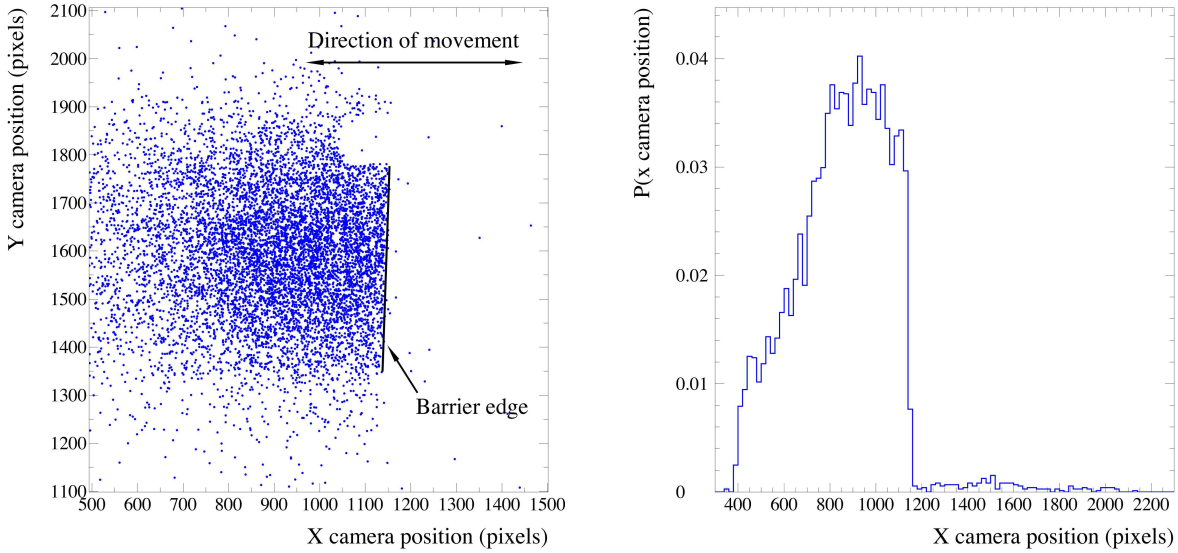

Figure A.1: *The* **left** *figure shows the beam being partly obstructed by the barrier. Note that due to the mounting of the camera the direction are reversed and the nose like structure visible in the upper part of the picture, which is part of the barrier. The* **right** *side shows a projection of the left picture onto the x-axis (here: binning = 200) as utilized in the automatic pixel-to-mm calibration.*

from the recorded position of the barrier on the detector and the measured vertical shifts. A numerical approach to determine the calibration factor has been developed. The picture shown in Fig. A.1 is projected onto the x-axis. An exemplary result of this projection is displayed in Fig. A.2. For enhancement of the picture the x-axis is divided into a certain amount of bins N. The data is then sorted into the different bins on each projection. A straightforward PAW routine was written to detect the barrier edge. Coming from the high x values the routine checks the amount of hits accumulated in each bin and compares it to a given threshold. If the amount of recorded data in a certain number of successive bins is larger than the threshold the barrier edge is said to be found. For the number of successive bins an amount of 15 was found to produce reliable results, while the threshold value was adjusted dynamically according to the number of bins used. Since the accuracy with which the edge position can be detected is dependent on the binning used for the projected picture the procedure was carried out over a wide range of binning resolution, i.e. amount of pixels included in one bin ($\frac{\text{Pixels}}{\text{Bin}}$). The calibration factors obtained for different binning resolutions are shown in Fig A.2. It can be seen that at low binning resolution the obtained values vary to a large extend. The reason for that being the resolution of the camera, which is much higher than the applied binning resolution. This results in a high inaccuracy in the determined barrier edge position. Then a regime is approached, where binning resolution and camera resolution match and where the calibration factors remain constant (denoted by the red line). At values below $2\frac{\text{Pixel}}{\text{Binning}}$ the binning resolution

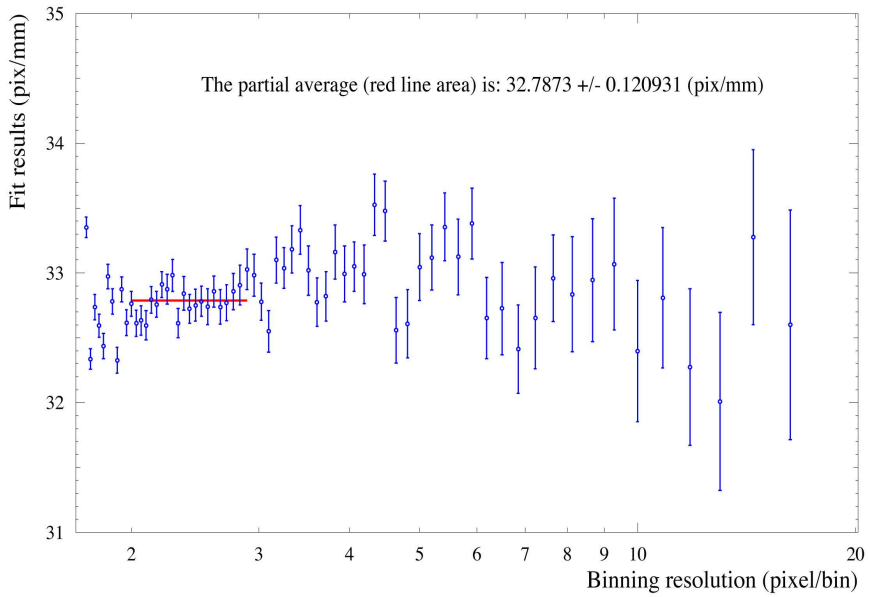

Figure A.2: *Automatic pixel-to-mm calibration.*

is higher than the camera resolution resulting again in a jitter of the obtained values for the calibration factor. The constant regime between a binning resolution of 2–3$\frac{\text{Pixel}}{\text{Binning}}$ was chosen to calculate a partial average for the calibration factor of $32.79 \pm 0.12\frac{\text{Pixel}}{\text{mm}}$ for the beam time in January 2003. Due to changes in the optics the calibration factor undergoes changes between beam times, hence the calibration for the April beam time differed by a few millimeters and was found to be $34.96 \pm 0.28\frac{\text{Pixel}}{\text{mm}}$.

References

[1] G. D. Carney and R. N. Porter, *H_3^+ : ab initio calculations of the vibrational spectrum*, J. Chem. Phys. **81** (1984), 1778–1784.

[2] T. R. Hogness and E. G. Lunn, *The ionization of hydrogen by electron impact as interpreted by positive ray analysis*, Phys. Rev. **26** (1925), 44–54.

[3] T. Oka, *Introductory remarks*, Philosophical Transactions of The Royal Society: Astronomy, physics and chemistry of H_3^+ (T. Oka E. Herbst, S. Miller and J. K. G. Watson, eds.), vol. 358, The Royal Society, 2000, pp. 2363–2369.

[4] D. W. Martin, E. W. McDaniel and M. L. Meeks, *On the possible occurence of H_3^+ in interstellar space*, Astrophys. J. **134** (1961), 1012–1013.

[5] T. R. Geballe and T. Oka, *Detection of H_3^+ in interstellar space*, Nature **340** (1996), 334–335.

[6] B. J. McCall, T. R. Geballe, K. H. Hinkle and T. Oka, *Detection of H_3^+ in diffuse interstellar medium toward Cygnus OB2 No. 12*, Science **279** (1998), 1910–1913.

[7] W. D. Watson, *Interstellar molecule reactions*, Rev. Mod. Phys. **48** (1976), 513–552.

[8] M. T. Leu, M. A. Biondi and R. Johnsen, *Measurements of recombination of electrons with H_3^+ and H_5^+ ions*, Phys. Rev. A **8** (1973), 413–419.

[9] N. G. Adams, D. Smith and E. Alge, *Measurements of dissociative recombination coefficients of H_3^+ , HCO^+, N_2H^+, and CH_5^+ at 95K and 300K using the FALP apparatus*, J. Chem. Phys. **81** (1984), 1778–1784.

[10] M. Larsson, H. Danared, J. R. Mowat, P. Sigray, G. Sundström, L. Broström, A. Filevich, A. Källberg, S. Mannervik, K. G. Rensfelt and S. Datz, *Direct high-energy neutral-channel dissociative recombination of cold H_3^+ in an ion storage ring*, Phys. Rev. Lett. **70** (1993), 430–433.

[11] J. Glosík, R. Plašil, V. Poterya, P. Kudrna and M. Tichý, *The recombination of H_3^+ ions with electrons: dependence on the partial pressure of H_2* , Chem. Phys. Lett. **331** (2000), 209–214.

[12] A. Suzor-Weiner and I. F. Schneider, *Mystery of an interstellar ion*, Nature **412** (2001), 871–872.

[13] I. F. Schneider, A. E. Orel and A. Suzor-Weiner, *Channel mixing effects in the dissociative recombination of H_3^+ with slow energy electrons*, Phys. Rev. Lett. **85** (2000), 3785–3788.

[14] V. Kokoouline, C. H. Green and B. D. Esry, *Mechanism for the destruction of H_3^+ ions by electron impact*, Nature **412** (2001), 891–894.

[15] J. A. Stephens and C. H. Greene, *Quantum-defect description of* H_3 *and the Jahn-Teller effect*, Phys. Rev. Lett. **102** (1995), 1579–1591.

[16] H. Kreckel, S. Krohn, L. Lammich, M. Lange, J. Levin, M. Scheffel, D. Schwalm, J. Tennyson, Z. Vager, R. Wester, A. Wolf and D. Zajfman, *Vibrational and rotational cooling of H_3^+* , Phys. Rev. A **66** (2002), no. 052509.

[17] D. Strasser, L. Lammich, H. Kreckel, S. Krohn, M. Lange, A. Naaman, D. Schwalm, A. Wolf and D. Zajfman, *Breakup dynamics and isotope effect in H_3^+ and D_3^+ dissociative recombination*, Phys. Rev. A **66** (2002), no. 032719.

[18] S. C. Brown, *Itroduction to Electrical Discharges in Gases*, John Wiley & Sons, 1966.

[19] Y. P. Raizer, *Gas Discharge Physics*, Springer-Verlag, 1997.

[20] F. Llewellyn-Jones, *The Glow Discharge*, Methuen & Co LTD, 1966.

[21] D. D. Šijačić and Ute Ebert, *Transition from townsend to glow discharge: subcritical, mixed, or supercritical characteristics*, Physical Review E **66** (2002).

[22] M. C. Penache, *Study of High-Pressure Glow Discharges Generated by Micro-Structured Electrode (MSE) Arrays*, Ph.D. thesis, Johann Wolfgang Goethe - Universität in Frankfurt am Main, 2002.

[23] G. Schäfer and K. H. Schönbach, *Basic mechanism contributing to the hollow cathode effect*, Physics and Applications of Pseudosparks (M. A. Gundersen and G. Schäfer, eds.), Plenum Press, 1990, pp. 55–76.

[24] F. Howorka and M. Pahl, *Experimentelle Bestimmung innerer und äußerer Parameter des negativen Glimmlichtplasmas einer zylindrischen Hohlkathodenentladung in Argon*, Z. Naturforsch. **27** (1972), 1425–1433.

[25] P. F. Little and A. von Engel, *The hollow cathode effect and the theory of glow discharges*, Proc. Roy. Soc. **224** (1954), 209–227.

[26] A. Güntherschulze, *Einige neue charakteristische Abstände bei der Glimmentladung*, Z. Physik **30** (1924), 175–186.

[27] ———, *Glimmentladung an Hohlkathoden*, Z. tech. Physik **11** (1930), 49–54.

[28] D. J. Struges and H. J. Oskam, *A qualitative theory of the medium pressure hollow cathode effect*, Physica **37** (1967), 457–466.

[29] A. Güntherschulze, *Die Stromdichte des normalen Kathodenfalls*, Z. Physik **19** (1923), 313–332.

[30] H. Helm, *Experimenteller Nachweis des Pendel-Effekts in einer zylindrischen Niederdruck-Hohlkathoden-Entladung in Argon*, Z. Naturforsch. **27** (1972), 1812–1820.

[31] T. Musha, *Cathode sputtering in hollow cathode discharges*, Journal of the Physical Society of Japan **17** (1962), 1440–1446.

[32] D. J. Struges and H. J. Oskam, *Studies of the properties of the hollow cathode glow discharge in helium and neon*, J. Applied Physics **35** (1964), 2887–ff.

[33] E. Badareu, I. Popescu and T. Iova, *Beiträge zur Klärung des Mechanismus des Doppelkathodeneffektes*, Ann. Physik **6–7** (1960), 308–326.

[34] J. W. Gewartowski and H. A. Watson, *Principles of electron tubes*, Van Nostrand, 1965.

[35] D. J. Struges and H. J. Oskam, *Hollow cathode glow discharge in hydorgen and the noble gases*, J. Applied Physics **37** (1966), 2405–2412.

[36] H. D. Smyth, *Primary and secondary products of ionization in hydrogen*, Phys. Rev. **25** (1925), 452–468.

[37] T. Oka, *The H_3^+ ion*, Molecular ions: spectroscopy, structure and chemistry (T. A. Miller and V. E. Bondybey, eds.), North-Holland Publishing, 1983, pp. 73–90.

[38] M. Saporoschenko, *Formation of H_3^+ and H_5^+ ions*, J. Chem. Phys. **42** (1965), 2760–2764.

[39] F. Kirchner, *Wasserstoffmoleküle mit vier und fünf Atomen*, Z. Naturforsch. **18** (1963), 879–880.

[40] W. Paul, B. Lücke, S. Schlemmer and D. Gerlich, *On the dynamics of the reaction of postive hydrogen cluster ions (H_5^+ to H_{23}^+) with para and normal hydrogen at 10K*, International Journal of Mass Spectrometry and Ion Processes **149** (1995), 373–387.

[41] W. D. Davis and T. A. Vanderslice, *Ion energies at the cathode of a glow discharge*, Phys. Rev. **131** (1963), 219–228.

[42] U. Müller, U. Majer, R. Reichle and M. Braun, *Spectroskopy of high n Rydberg states of the triatomic deutirium molecule* D_3, J. chem. Phys. **106** (1997), 7958–7967.

[43] R. Reichle, I. Mistrík, U. Müller and H. Helm, *Rotational channel interactions of vibrationally excited np Rydberg states of the triatomic hydrogen molecule*, Phys. Rev. A **60** (1999), 3929–3942.

[44] U. Müller, *private communication.*

[45] F. Pobell, *Matter and methods at low temperatures*, Springer Verlag, 1996.

[46] D. A. Dahl, *SIMION 3D Version 7.0*, 2000.

[47] M. Wutz, H. Adam, W. Walcher and K. Jousten, *Handbuch Vakuumtechnik: Theorie und Praxis*, Vieweg, 2000.

[48] H. Hänsel, W. Neumann, R. Wedell, P. Gehrmann, A. Mertens and R. Stolle, *Physik: Mechanik und Wärmelehre*, Spektrum Akademischer Verlag, 1993.

[49] *MAFIA Version 3.2*, 1994.

[50] T. Šimko, V. Martišovitš, J. Bretagne and G. Gousset, *Computer simulations of H^+ and H_3^+ transport in hydrogen drift tubes*, Phys. Rev. E **56** (1997), 5908–5919.

[51] B. L. Peko and R. L. Champion, *Total cross sections for low energy collisions of H_3^+ with molecular hydrogen and rare gas*, J. Chem. Phys. **107** (1997), 1156–1162.

[52] A. D. White, *New hollow cathode glow discharge*, J. Applied Physics **30** (1959), 711–719.

[53] R. von Hahn, M. Grieser, D. Habs, E. Jaeschke, C.-M. Kleffner, J. Liebermann, S. Papureanu, R. Repnow, D. Schwalm and M. Stampfer, *Development of seven-gap resonators for the Heidelberg high current injector*, Nucl. Instrum. Methods A **328** (1993), 270–274.

[54] M. Grieser, H. Deitinghoff, D. Habs, R. von Hahn, E. Jaeschke, C.-M. Kleffner, V. Kössler, S. Papureanu, R. Repnow, M.-H. Rhee, D. Schwalm and A. Schempp, *Upgrading of the Heidelberg accelerator facility with a new high current injector*, Nucl. Instrum. Methods A **328** (1993), 160–163.

[55] S. Datz, G. Sundström, C. Biedermann, L. Broström, H. Danared, S. Mannervik, J. R. Mowat and M. Larsson, *Branching processes in the dissociative recombination of* H_3^+ , Phys. Rev. Lett. **74** (1995), 896–899.

[56] R. Wester, F. Albrecht, M. Grieser, L. Knoll, R. Repnow, D. Schwalm, A. Wolf, A. Baer, J. Levin, Z. Vager and D. Zajfman, *Coulomb explosion imaging at the heavy ion storage ring TSR*, Nucl. Instrum. Methods A **413** (1998), 379–396.

[57] R. Keller, B. R. Nielsen and B. Torp, *Metal beam production using a high current ion source*, Nucl. Instrum. Methods B **37/38** (1989), 74–77.

[58] M. Madert, R. Cee, M. Grieser, R. von Hahn, S. Papureanu, H. Podlech, R. Repnow, D. Schwalm and C.-M. Kleffner, *The RFQ-accelerator for the Heidelberg high current injector*, Nucl. Instrum. Methods B **139** (1998), 437–440.

[59] D. Habs, W. Baumann, J. Berger, P. Blatt, A. Faulstich, P. Krause, G. Kilgus, R. Neumann, W. Petrich, R. Stockstad, D. Schwalm, E. Szmola, K. welti, A. Wolf, S. Zwickler, E. Jaeschke, D. Krämer, G. Bisoffi, M. Blum, A. Friedrich, C. Geyer, M. Grieser, H. W. Heyng, B. Holzer, R. Ihde, M. Jung, K. Matl, W. Ott, B. Povh, R. Repnow, M. Steck, E. Steffens, D. Dutta, T. Kühl, D. Marx, S. Schröder, M. Gerhard, R. Grieser, G. Huber, R. Klein, M. Krieg, N. Schmidt, R. Schuch, J. F. Babb, L. Spruch, W. Arnold and A. Noda, *First experiments with the Heideleberg test storage ring TSR*, Nucl. Instrum. Methods B **43** (1989), 390–410.

[60] P. Baumann, M. Blum, A. Friedrich, C. Geyer, M. Grieser, B. Holzer, E. Jaeschke, D. Krämer, C. Martin, K. Matl, R. Mayer, W. Ott, B. Povh, R. Repnow, M. Steck, E. Steffens and W. Arnold, *The Heidelberg ion test storage ring TSR*, Nucl. Instrum. Methods A **268** (1988), 531–537.

[61] G. Bisoffi, M. Grieser, E. Jaeschke, D. Krämer and A. Noda, *Radiofrequency stacking experiments at the Heidelberg test storage ring*, Nucl. Instrum. Methods A **287** (1990), 320–323.

[62] S. Krohn, *Inelastic collisions and recombination between electrons and molecular ions*, Ph.D. thesis, Universität Heidelberg, 2002.

[63] M. Steck, G. Bisoffi, M. Blum, A. Friedrich, C. Geyer, M. Grieser, B. Holzer, E. Jaeschke, M. Jung, D. Krämer, K. Matl, W. Ott and R. Repnow, *Electron cooling of heavy ions*, Nucl. Instrum. Methods A **287** (1990), 324–327.

[64] M. Schmitt, *Erzeugung energiescharfer Elektronenstrahlen*, Ph.D. thesis, Universität Heidelberg, 2000.

[65] V. V. Parkhomchuk and A. N. Skrinsky, *Electron cooling: physics and prospective applications*, Rep. Prog. Phys. **54** (1991), 919–947.

[66] D. Zajfman, Z. Amitay, C. Broude, P. Forck, B. Seidel, M. Grieser, D. Habs, D. Schwalm and A. Wolf, *Measurement of branching ratios for the dissociative recombintation of the cold HD^+ using fragmetn imaging*, Phys. Rev. Letters **75** (1995), 814–817.

[67] L. Lammich, H. Kreckel, S. Krohn, M. Lange, D. Schwalm, D. Strasser, A. Wolf and D. Zajfman, *Breakup dynamics in the dissociative recombination of H_3^+ and its isotopomers*, Radiation Phys. Chem. **in press** (2003).

[68] H. Helm, F. Howorka and M. Pahl, *Über den Fallraum einer zylindrischen Hohlkathode*, Z. Naturforsch. **27** (1972), 1417–1425.

[69] S. Schößler, *Ionenerzeugung mit Hochdruck-Mikroentladungen*, Diplomarbeit, Johann Wolfgang Goethe - Universität in Frankfurt am Main, 2002.